

A high-sensitivity resonant sensor realised through the exploitation of nonlinear dynamic behaviour

A thesis submitted to the Faculty of Science,
Agriculture and Engineering for the Degree of
Doctor of Philosophy

by
William H. Waugh
M.Sc.

School of Mechanical and Systems Engineering
Newcastle University

October 2010

Abstract

Measurements of viscosity and density allow for the monitoring of fluid quality and processes involving a fluid environment. There are various fields in which such measurements may be required, including oil exploration and production, environmental monitoring, process control, medicine, and the automotive industry. Existing MEMS viscometers and density meters typically measure vibrational characteristics such as resonant frequency, bandwidth and quality factor.

This thesis reports on the development of a high-sensitivity resonant sensor. In order to significantly improve sensitivity to changes in viscosity and/or density the proposed sensor will exploit nonlinear dynamic behaviour and measure the frequency separation between singular jump points in the frequency response function.

By using a one-mode approximation when excited near resonance, the dynamics of a clamped-clamped slender beam immersed in fluid is that of a standard Duffing oscillator. With harmonic forcing of sufficient magnitude, a bistable region, bounded by amplitude jump points, is seen to occur. The width of this bistable region, δF , is dependent on the damping ratio of the system, which is shown to be a function of the dynamic viscosity and density.

Experiments with clamped-clamped silicon <100> beams in a range of Newtonian gases demonstrate that the measurand δF can uniquely identify a fluid, and may be amplified to magnitudes greatly exceeding bandwidth measurements for the same device. In addition, the sensitivity of the proposed nonlinear sensor to changes in fluid properties at low viscosity can be at least an order of magnitude better than that of conventional devices. Forcing magnitude and control is identified as being critical to the measured width of the bistable region. Beam dimensions can be chosen to optimise measurements for the desired application.

Acknowledgements

Firstly I would like to thank my supervisors Dr Barry Gallacher and Professor Jim Burdess for their continued help and support throughout this Ph. D. Particular thanks go to Dr Gallacher who has been at hand to provide advice, explanations and encouragements on a daily basis. Without this help, this work would have proven far more difficult. I wish to thank Dr John Hedley for his help in the laboratory, and I would extend thanks to all the staff in the mechanical workshops for their assistance. Thank you also to Mr Robert Davidson for his advice regarding Autodesk Inventor, and to Mr Stuart Marsden for his assistance with Matlab. I would like to extend a general thank you to all of my colleagues within the School of Mechanics and Systems Engineering, as I have found everyone to be extremely approachable and helpful. Finally thank you to my family for supporting me throughout this Ph. D.

Contents

Abstract	i
Acknowledgements	ii
Contents	iii
Nomenclature	ix
1 Introduction	1
1.1 Background	1
1.2 Motivation	2
1.3 Aims and objectives	3
1.4 Microresonators	4
1.4.1 Linear microresonators	4
1.4.2 Nonlinear microresonators	5
1.4.3 Sources of nonlinearities	5
1.4.4 Sources of damping	7
1.5 Beam theories	9
1.6 Fluid damping models	9
1.7 Previous work	10
1.7.1 Modelling nonlinear behaviour in MEMS	10
1.7.2 MEMS as linear sensors	10
1.7.3 MEMS as nonlinear sensors	11
1.8 Thesis overview	12
1.9 References	14
2 Beam kinematics	17
2.1 Dominant nonlinearity	17
2.2 Temperature effects	17
2.2.1 Tension	17
2.2.2 Beam dimensions	18
2.3 Beam theory	18

2.3.1 Euler-Bernoulli theory	18
2.3.2 Bending and curvature	19
2.3.3 Second moment of area	21
2.4 Equation of motion	22
2.4.1 Axial strain	22
2.4.2 Kinetic energy	24
2.4.3 Potential energy	24
2.4.4 Hamilton's principle	25
2.5 Intrinsic damping	27
2.5.1 Support loss	28
2.5.2 Thermoelastic damping (TED)	29
2.5.3 Surface damping	29
2.5.4 Equation of motion with intrinsic damping	30
2.6 References	31
3 Fluid damping	32
3.1 Flow regimes	33
3.1.1 Fluid damping in each flow regime	34
3.2 Damping force in a continuum	36
3.2.1 Added mass	36
3.2.2 Skin friction drag	37
3.2.3 Pressure drag	37
3.2.4 Resultant damping force	38
3.3 Viscous regime damping models	39
3.3.1 Circular cylinder model	40
3.3.2 Elliptic cylinder model	42
3.4 Molecular and transition regimes damping model	44
3.4.1 Molecular model	44
3.5 Equation of motion with fluid damping	44
3.6 Summary	44
3.7 References	45

4 Problem formulation and solution modelling	47
4.1 Harmonic displacement	47
4.2 Modal analysis	48
4.2.1 Analysis of fundamental mode	49
4.3 Quantitative analysis	55
4.3.1 Harmonic balance solution	56
4.3.2 Frequency response	57
4.4 Stability	58
4.4.1 Jump points and peak response	58
4.4.2 Stability condition	60
4.5 Numerical predictions	65
4.5.1 Added mass effect	65
4.5.2 Effect of fluid properties	68
4.5.3 Effect of boundary conditions	71
4.5.4 Sensitivity to changes in fluid properties	72
4.5.5 Beam dimensions	74
4.5.6 Beam materials	76
4.5.7 Using ODE solvers in Matlab	77
4.6 Summary	79
4.7 References	80
5 Design and fabrication of devices	81
5.1 Material considerations	81
5.1.1 Crystalline silicon	81
5.1.2 Silicon wafers	82
5.1.3 Silicon On Insulator (SOI) substrates	83
5.2 Design considerations and limitations	83
5.3 Fabrication process	84
5.3.1 Summary of process	84
5.3.2 Photolithography and etching processes	87
5.4 Fabricated devices	88

5.5 References	90
6 Experimental methodology and test equipment	91
6.1 Overview of test equipment	91
6.1.1 Surface profiler	92
6.1.2 Laser vibrometer	94
6.1.3 Signal analyser	96
6.2 Description of test chamber	98
6.2.1 Peltier heating and temperature measurement	99
6.2.2 Piezo-vibrator actuation	100
6.2.3 Pressure transducer	101
6.2.4 Imperfections	102
6.3 Test gases	104
6.4 Testing and data gathering procedures	105
6.4.1 Preliminaries	105
6.4.2 Static measurements	107
6.4.3 Vibratory measurements	108
6.5 References	111
7 Experimental results for fabricated devices	112
7.1 Overview	112
7.1.1 Actuation	112
7.1.2 Typical frequency response data	114
7.1.3 Nonlinear response data	118
7.1.4 Amplitude of vibration	121
7.2 Temperature effects	122
7.2.1 Background stability	122
7.2.2 Boundary conditions	128
7.2.3 Beam dimensions	129
7.3 Beam comparison	130
7.4 Limits	132
7.4.1 Magnitude of readings	132

7.4.2 Achievable resonant modes	133
7.4.3 Pressure regimes	134
7.5 Summary	135
8 Analysis	136
8.1 Approximations	136
8.1.1 Errors and uncertainties	136
8.1.2 Reynolds and Keulegan-Carpenter numbers	136
8.1.3 Beam and fluid properties	136
8.2 Influence of background	138
8.2.1 Shifting and scaling background data for modelling purposes	138
8.2.2 Effect of background profile	143
8.3 Detailed modelling	145
8.3.1 Molecular regime - linear	146
8.3.2 Molecular regime - nonlinear	150
8.3.3 Viscous regime - linear	151
8.3.4 Viscous regime – nonlinear	152
8.4 Sensitivity	154
8.4.1 Identifying gases	154
8.4.2 Model prediction	159
8.5 References	162
9 Conclusions	163
9.1 Contributions	163
9.2 Limitations of the study	164
9.2.1 Experimental issues	164
9.2.2 Modelling issues	166
9.3 Implications of study	167
9.4 Further work	168
9.4.1 Actuation	168
9.4.2 Detection	168
9.4.3 Alternative fluids and materials	168

9.4.4 Develop damping model	169
9.4.5 Analysis of further modes and/or harmonics	170
9.4.6 Alternative applications	170
9.5 References	171

Appendices

A. Fluid properties

B. Silicon properties

Nomenclature

Chapter 1

δF	Frequency separation of jump points
ω_n	Natural frequency
Q	Quality factor

Chapter 2

L	Beam length
η	Initial extension
α_L	Thermal expansion coefficient
ΔL	Change in beam length
ΔT	Change in temperature
θ	Slope angle
s	Arc length
κ	Curvature
x, y, z	Local axes
M	Bending moment
E	Young's modulus
I	Second moment of area
U_B	Bending potential energy
I_z	Second moment of area about z axis
dA	Elemental area
b	Beam width
d	Beam depth
$u(x)$	Displacement in x direction
$v(y)$	Displacement in y direction
$w(z)$	Displacement in z direction
\bar{u}	Longitudinal extension
\bar{v}	Transverse extension
ds	Initial length of centerline element
ds^*	Deformed length of centerline element

$\overline{\varepsilon_{xx}}$	Axial strain on centreline
$\partial\varepsilon$	Reduction in strain
∂x	Elemental length
ε_{xx}	Axial strain
T	Kinetic energy
ρ	Beam density
A	Cross-sectional area
U_0	Strain energy density
U	Strain energy
δ	Variation operator
δW_{nc}	Virtual work
δT	Variation in kinetic energy
δU	Variation in potential energy
N	Constant
Q_{sup}	Support loss quality factor
Q_{TED}	TED quality factor
Q_{surf}	Surface loss quality factor
Q_{int}	Intrinsic damping quality factor
λ_T	Transverse elastic wave wavelength
C_T	Propagation velocity of transverse elastic wave
f	Resonant frequency
ν	Poisson's ratio
β_n	Mode constant
χ_n	Mode shape factor
C_p	Specific heat
κ_T	Thermal conductivity
ω	Angular frequency
E_{ds}	Dissipation value
δ_s	Surface layer thickness
c_I	Intrinsic damping coefficient

Chapter 3

ρ_f	Fluid density
μ	Fluid dynamic viscosity
Kn	Knudsen number
λ	Mean free path of gas molecule
w	Width of gas layer
k_B	Boltzmann constant
T	Absolute temperature
p	Gas pressure
d_g	Diameter of gas molecule
L	Beam length
Re	Reynolds number
Kc	Keulegan-Carpenter number
D	Characteristic length
U_m	Maximum fluid velocity
T_o	Period of oscillation
$U(t)$	Velocity of oscillating body
$F(t)$	Inline force
C_a	Added mass coefficient
V	Volume of body
C_D	Drag coefficient – circular cylinder model
A	Reference area
v	Fluid velocity at given point
δ	Viscous penetration depth
M_A	Added mass per unit length
α	Width to depth coefficient
α_D	Drag force coefficient
F_D	Viscous drag force per unit length
Φ	Multiple of cylinder drag
$C_{damping}$	Damping coefficient – elliptic cylinder model
a	Cross-section shape parameter a
b	Cross-section shape parameter b

d_1	Minor axis of ellipse
d_2	Major axis of ellipse
v_T	Thermal velocity
m_g	Mass of gas molecule
$v(x,t)$	Displacement of beam element with respect to inertial frame
c_f	Fluid damping coefficient

Chapter 4

$\hat{v}(x,t)$	End displacement with respect to inertial frame
$v(x,t)$	Total displacement of element with respect to inertial frame
c	Selected drag coefficient for rectangular beam
h	Displacement amplitude
$T(t)$	Temporal function
$X(x)$	Spatial function
k_r	Constant
ω_0	Undamped natural frequency for fundamental mode
ρ_s	Beam density
δF	Frequency separation of jump points
λ	Nondimensional nonlinear parameter
ζ	Damping ratio
P	Forcing constant
ω_a	Modelled damped resonant frequency
S	Stability parameter

Chapter 6

V_{output}	Output signal voltage
K	Conversion efficiency constant
f_{Bragg}	Bragg frequency shift
v_o	Object velocity
λ_{source}	Source wavelength
$f_{Doppler}$	Doppler shift

\tilde{x}	Displacement amplitude
\tilde{v}	Velocity amplitude
V_R	Velocity range
f	Actuation frequency
F_1	FFT of channel 1 signal
F_2	FFT of channel 2 signal

Chapter 7

\bar{h}	Mean of background displacement
-----------	---------------------------------

Chapter 8

SHIFT	Frequency shift and amplitude scaling parameter
<i>MOL</i>	Molecular damping coefficient
<i>OTHER</i>	Experimentally defined damping coefficient
Q	Quality factor
ζ	Damping ratio
ω_d	Measured damped resonant frequency

Chapter 1

Introduction

1.1. Background

Microelectromechanical systems (MEMS) is the integration of mechanical elements, sensors, actuators, and electronics in devices typically fabricated using integrated circuit batch-processing technologies. MEMS devices typically have characteristic dimensions in the region of $1\mu\text{m}$ to 1mm .

MEMS technology has grown rapidly and has generated diverse developments in a wide range of fields, including automotive, aerospace, biotechnology and bioengineering, medicine and pharmaceuticals, telecommunications and manufacturing. MEMS devices are used for a range of purposes in these fields, with applications including RF signal filtering, resonant mass sensing, inertial sensing, radiation sensing, magnetic field sensing, chemical sensing, cooling and optical scanning.

MEMS devices function as integral components in a number of technologies, and may be used as, for example, actuators, motors, switches or sensors. Some specific examples of MEMS devices include accelerometers for automobile airbags [1], chemical and biological sensors [2,3,4], high-frequency signal filters [5,6] and atomic force microscopes (AFMs) [7].

Silicon is the material used to create most MEMS devices. It possesses various advantages, including desirable mechanical properties and high purity [8]. In addition, silicon processing technologies are well established and enable batch production, reducing the cost of devices.

Silicon micromechanical components are generally fabricated using processes that either selectively etch away parts of a silicon wafer (bulk silicon micromachining), or add structural layers (surface silicon micromachining) to form the devices [8].

MEMS devices can offer numerous advantages over their traditional macroscale counterparts. MEMS consume minimal power, occupy minimal space, are light, have fast response time, offer high precision and reliability, and are integrable with existing integrated circuit technologies. MEMS can be scaled such that effects not easily exploitable at macroscale become of interest: this is of pertinence to this study where devices are designed to exploit nonlinearities.

1.2. Motivation

This work investigates the possible use of nonlinear MEMS microresonators as sensors for measuring fluid viscosity and density. The vast majority of research related to microresonators has to date focused on oscillators utilising a linear frequency response structure. MEMS viscometers and density sensors have typically measured the linear vibrational characteristics of resonant frequency, bandwidth and quality factor [9,10].

The measurement of viscosity and density is of interest as it allows for the identification of fluids, monitoring of fluid quality and monitoring of processes involving a fluid environment. Such measurements are required across a range of fields, from oil exploration and production, to environmental monitoring, process control, for medical applications and within the automotive industry [10,11,12,13,14].

Suitably designed nonlinear microresonators are believed to be capable of performing in a superior fashion to their linear counterparts [15]. The sensor discussed in this thesis exploits the nonlinear dynamic behaviour of a rectangular beam microresonator in a novel way by measuring the frequency separation δF between singular points in the frequency response function. In doing so, a significant improvement in sensitivity to changes in viscosity and/or density is demonstrated.

An increased sensitivity viscometer and/or density meter would prove valuable for applications currently requiring greater accuracy in measurements. Examples include measurements for clean fuels such as dimethyl ether [16], and medical applications such as monitoring of synovial fluid viscosity [14].

It is important to restate that while the system described here is believed to be novel, the use of linear or nonlinear MEMS devices as fluid sensors is not. Section 1.7 outlines previous pertinent research.

1.3. Aims and objectives

This work focuses predominantly on the geometric nonlinearities which occur due to midplane stretching of clamped-clamped beam resonators of rectangular cross-section. The frequency response of such devices shows the existence of jump phenomenon [17,18]. The jump points are singularities which can be measured to a high degree of accuracy. By utilising the existence of these jump points, and measuring the frequency difference between them, it may be possible to design novel MEMS sensors capable of measuring fluid properties with increased sensitivity.

The overall aim of the research presented is to investigate the nonlinear response of resonator beams immersed in a range of gases. Experimental data will be presented and analysed, to establish whether nonlinear measurands may be used to identify gases directly. Further, the nonlinear results will be compared with linear measurements to compare the sensitivity of each approach to changes in gas properties.

The specific objectives of the research are summarised as follows:

- Establish a representative equation of motion for a harmonically displaced clamped-clamped rectangular beam immersed in a viscous fluid.
- Derive the frequency response of the beam by means of modal analysis, using a single-mode approximation.
- Examine the stability of the steady-state solution for the equation of motion.
- Obtain numerical predictions of beam behaviour in a range of fluids.
- Design and fabricate suitable resonator beams for experimental purposes.
- Design suitable experiments and select or commission experimental equipment.

- Conduct appropriate experiments in order to gather necessary data and validate model predictions.
- Present experimental results appropriately in order to demonstrate potential uses of devices as fluid sensors.
- Analyse experimental data to evaluate and develop further the system model.
- Use experimental data and model to comment on observed and predicted advantages of the nonlinear approach.

1.4. Microresonators

1.4.1. Linear microresonators

Harmonically-forced, linear resonators are the most common of modern microresonators. Such resonators have a Lorentzian frequency response which is dependent on the resonator's natural frequency ω_n , quality factor Q and excitation amplitude [15]. A high quality factor indicates that a pronounced resonance will be clearly distinguishable from non-resonant vibrations.

A variety of density and viscosity sensors have been developed based on the exploitation of resonance. Examples of devices operating in the linear regime include vibrating wire viscometers [19], oscillating plates [13] and quartz-crystal microbalances [20]. The frequency response of a resonator in a surrounding fluid depends strongly on the properties of the fluid. The resonance frequency and damping (and hence quality factor Q) are influenced by the viscosity and density, and hence can be used to sense these properties. [10,21,22].

However, there remain challenges in terms of sensor accuracy, flexibility, and use outside of the laboratory environment [10,13]. The behaviour of a finite rectangular beam resonator immersed in a viscous fluid needs careful consideration, as there is no analytical solution to this problem [23]. An analytic solution for the idealised geometry of a thin blade of zero thickness and infinite length has however been presented [24].

1.4.2. Nonlinear microresonators

MEMS devices frequently feature inherent nonlinearities. However, the exploitation of nonlinear frequency response structures has been limited compared to the linear case. Early investigations into the use of nonlinear microresonators focused on forced harmonic oscillators with nonlinearities occurring due to large elastic deformations [15]. Subsequent work showed electrically actuated nonlinear resonators being considered by various authors [25,26]. In recent years there has been increased attention to nonlinear microresonators, with studies considering such matters as the storage of vibrational energy [27], nonlinear response to piezoelectric actuation [28], effect of superharmonic excitation [29], and mass detection [30]. This increased attention has been attributed to the potential for increased tunability of devices and superior performance [15]. A review of nonlinear micro- and nanoresonators has been presented by Rhoads, Shaw and Turner [31].

1.4.3. Sources of nonlinearities

Nonlinearities can arise in many different ways and take different forms. Any component of the equations of motion may be affected by nonlinearities, such as the inertial terms, terms describing restoring forces, dissipative terms, excitation terms, and boundary conditions [32,33,34]. An overview of nonlinearities common to MEMS devices is presented below.

Geometrical nonlinearities

Geometric nonlinearities arise from nonlinear strain-displacement relationships. Sources of geometric nonlinearities include large deflections of an element, large curvatures and large rotations. In this context, deformations are considered small where the standard small angle approximation of $\sin \theta \approx \theta$ is valid (see section 2.3.2 for a related discussion of curvature.) Examples of geometrical nonlinearities include the midplane stretching of a clamped-clamped beam subject to large transverse deflections, or the nonlinearity of the sine term in the pendulum equation at large rotations.

Material nonlinearities

All real materials exhibit a certain amount of nonlinearity in the relationship between stress and strain, due to nonlinearities in atomic interactions. There is therefore a nonlinear relationship between force and deformation when strain variations are large [32].

Nonlinear body forces

Body forces acting on a structure can vary nonlinearly. For example, the magnetic potential for a beam in a magnetic field is approximated by an expression including terms higher than quadratic, causing nonlinearities to appear in the equation of motion [32]. Fluid behaviour is governed by nonlinear equations, so consideration of fluid and aerodynamic forces on a body must recognise nonlinearity in these forces.

Physical configuration nonlinearities

The specific configuration of components in a system can introduce nonlinearities. This is true even when the individual components are linear, or operated within a linear regime [32].

Consider again a clamped-clamped beam. The nonlinearity which arises due to midplane stretching is of a geometrical origin. However, if one of the clamped ends of the beam were free to move in a longitudinal direction, the nonlinearity would disappear. Thus the physical configuration determines whether the nonlinearity manifests itself or not.

Inertia nonlinearities

Inertia nonlinearities arise from nonlinear terms containing velocities and/or accelerations in the equations of motion. They may be a result of, for instance, concentrated or distributed masses. It is the kinetic energy of the system which is the source of these nonlinearities. Examples include centripetal acceleration terms [33, 35].

Other nonlinearities may arise from, for instance, the boundary conditions, the presence of friction, or from impacts to a system.

1.4.4. Sources of damping

Energy loss from MEMS devices occurs due to both internal and external mechanisms. Dissipative forces act to change the behaviour of the device. These forces are referred to as the damping forces on the system.

For oscillatory MEMS devices, movement involves the dissipation of energy, which is drawn from the vibrational energy of the device. Energy losses are quantified by means of the quality factor, which is the ratio of the energy stored to the energy lost during one cycle of vibration. A damping coefficient may be expressed in terms of the quality factor. There follows an overview of the typical sources of damping affecting MEMS devices.

Material damping

Material damping is the dissipation of energy from solid bodies due to lattice defects or the internal structure of the body. During mechanical vibrations, deformations occur in the body which are accompanied by thermodynamically irreversible processes [36]. Molecular interaction in the material is the source of this damping.

Fluid damping

Fluid interaction with an oscillating body causes dissipative processes. These are covered in detail in chapter 3, but a brief description of the damping processes is provided here.

- Acoustic radiation: loss occurs when oscillations create sound waves in the fluid.
- Skin friction drag: fluid viscosity acts against the oscillatory motion.
- Added mass: the inertia of the fluid surrounding the body adds to the bodies effective mass.
- Pressure drag: separation of the flow around an oscillating body causes a pressure gradient which acts against the oscillatory motion.

- Molecular damping: collisions between individual fluid molecules and the oscillating body cause a transfer of momentum, which acts against the oscillatory motion.
- Squeeze- and slide-film damping: thin fluid films between a moving surface and a fixed structure generate a resistance to motion.

Support or anchor loss

This type of loss can occur as a result of the device structure. Vibrating MEMS can create elastic waves which are then propagated through the device supports or anchors. See section 2.5.1. for further discussion.

Thermoelastic damping (TED)

An oscillating body will create alternating regions of compression and extension. Compressed regions become hotter, extended regions cooler, resulting in temperature gradients across the body and hence heat flow [36]. Any resulting irreversible heat flow then causes energy to be dissipated. This is discussed further in section 2.5.2.

Surface damping

Surface damping has been identified as an important loss mechanism in MEMS devices. A loss in quality factor has been experimentally observed when device dimensions are reduced, increasing the surface-to-volume ratio. However, no precise mechanism has yet been determined. It is suggested that surface imperfections, adsorbents or oxidation are responsible. For a further discussion of surface damping see section 2.5.3.

Other damping mechanisms which may affect MEMS device, but are not considered in this work, include volume losses, phonon-mediated damping, and coupling losses due to the coupling of different kinds of vibration [36].

1.5. Beam theories.

The two most popular beam theories in use today for modelling MEMS beam resonators are the Euler-Bernoulli beam theory and the Timoshenko beam theory.

The simplest of these models is given by Euler-Bernoulli theory, and is discussed in detail in section 2.3.1. In brief, this theory assumes that plane cross-sections, which are normal to the neutral axis before deformation, remain plane and normal to the neutral axis on deformation. This then assumes that warping, shear deformation effects and transverse normal strains are negligible. These assumptions are assumed valid for slender beams [35].

Where the beam is not slender, or there are high-frequency modes excited, or the beam is made of a composite material, Euler-Bernoulli theory is insufficient and the Timoshenko theory must be used. In these cases, the transverse shear is not negligible and must be accounted for. With transverse shear, rotation of a cross-section occurs due to both bending and transverse shear deformation. Timoshenko [37] derived correction terms for the effects of shear and of rotary inertia.

In this work, the experimental beam dimensions are such that Euler-Bernoulli theory is deemed appropriate. The model is taken and adapted to include the effect of nonlinearities introduced by midplane stretching.

1.6. Fluid damping models

As a body oscillates in a fluid, the vibrating structure interacts with the fluid and energy is dissipated. Fluid damping models can be employed to account for this energy dissipation. Knowledge of the damping is essential if the dynamic behaviour of a structure in a fluid is to be fully understood.

The damping mechanism on which fluid damping models are based depends largely on the pressure regime of the fluid. The pressure determines whether a fluid may be considered a continuum, or as a collection of non-interacting molecules. In the former case, fluid damping results from the viscous shearing of the fluid at the surface of the structure and from flow separation. In the latter, dissipation occurs due to momentum exchange between the oscillating structure and the surrounding molecules.

Fluid behaviour is governed by nonlinear equations. The behaviour of a fluid surrounding an oscillating body is affected by the shape of the body. These two factors mean that any fluid damping models developed for use with finite rectangular beams will necessarily be approximate.

In this work, only Newtonian fluids are considered. The subject of fluid damping is covered in detail in chapter 3, where fluid damping models for use with a rectangular beam are presented.

1.7. Previous work

This section provides an overview of previous work relevant to the current study.

1.7.1. Modelling nonlinear behaviour in MEMS

There has been a vast amount of work conducted on the understanding of and solution to nonlinear equations. This section is then limited to a discussion of work directly related to MEMS devices or beams.

Various authors have studied the nonlinear vibrations of MEMS resonators. Mestrom et al. [38] considered the nonlinear dynamics of a clamped-clamped beam resonator, as did Rhoads, Shaw and Turner [39], Veijola and Mattila [40], and Tadayan et al. [41]. Emam [33] investigated nonlinear dynamics in buckled beams. Malatkar [35] studied nonlinear vibrations in cantilever beams and plates subject to transverse excitations. Braghin et al [18] consider nonlinearities affecting a MEMS translation gyroscope. A nonlinear modal analysis approach was used by Xie, Lee and Lim [42] to obtain nonlinear normal modes for a clamped-clamped beam. A review of previous work regarding nonlinear beam vibration is presented by Marur [43].

1.7.2. MEMS as linear sensors

One of the more common uses for MEMS devices as sensors is for the purpose of mass sensing. Rhoads [15] presents a thorough account of resonant mass sensing in MEMS. Resonant mass sensors are widely used in chemical and biological sensing applications. The sensitivity of such devices is such that Yang et al [44] have

reported the detection of zeptogram-scale mass particles with nanoscale beam resonators.

Linear MEMS devices have been employed as viscosity sensors. For instance, Ronaldson, Goodwin and Wakeham [13] devised an oscillating-plate viscometer, whereas Agoston, Keplinger and Jakoby [21] use a cantilever to measure viscosity of complex organic liquids.

Various other MEMS based sensors are encountered within the literature.

Examples include

- Gas sensors: Zribi et al [12] describe a resonant MEMS sensor for the detection of carbon dioxide and humidity.
- Chemical sensors: Goeders, Colton and Bottomley [45] describe the sensing of chemical interactions with a microcantilever.
- Atomic force microscopes: Sader [23] describes the application of cantilevers in viscous fluids towards the atomic force microscope.

All of the above sensors are linear in nature. The next section considers nonlinear sensors.

1.7.3. MEMS as nonlinear sensors

The exploitation of nonlinearity in MEMS sensors is relatively limited to date. The subject of nonlinear resonant mass sensing, as discussed in detail by Rhoads [15], is however of increasing interest. Indications are that mass sensors based on nonlinear frequency response structures may be capable of higher sensitivities than their linear counterparts. The principle is that a given device is driven close to a known bifurcation point. Should a small amount of mass attach itself or interact with the resonator, then there is a sharp change in the behaviour of the resonator. An example of such a device is given by Buks and Yurke [30].

Greywall [46] proposed a scheme for measuring magnetic field strength using a nonlinear mechanical resonator. Measurements of the nonlinear beam resonance peak provide information regarding the surrounding magnetic field.

For the measurement of fluid viscosity, Sullivan et al [47] discuss a nonlinear vibrating wire viscometer. In this case, nonlinearities appear in the drag of the fluid and the transient response of the wire is measured.

1.8. Thesis overview

The thesis consists of nine chapters.

Chapter 1 introduces the background and motivation of the work. The aims and objectives are stated. A brief discussion of microresonators, damping, nonlinearities and system modeling is presented. The chapter concludes with a review of related previous work.

In Chapter 2, the equation of motion for a transversely oscillating clamped-clamped beam in vacuum is derived using the Hamilton principle. Nonlinearities and intrinsic damping affecting the beam are discussed and evaluated.

In Chapter 3, the effect of immersing and vibrating a rectangular beam resonator in a viscous fluid is considered. Fluid forces and energy dissipation are discussed, and models for the fluid damping on the beam, oscillating in fluids at various pressures, identified.

In Chapter 4, the system equation of motion is developed, accounting for the presence of the surrounding fluid and the chosen actuation method. The system is analysed by means of modal analysis and approximation methods. Numerical predictions are then made from this analysis, informing subsequent design and experimental work.

Chapter 5 describes the design and fabrication of silicon beam resonators for use in experiment.

Chapter 6 presents the experimental equipment, setup and procedures. Problems encountered while performing experiments are described.

In Chapter 7, the experimental results are presented for the fabricated devices. Comment is made on data reliability, measurement repeatability, and experimental limiting factors.

Experimental data is analysed further in Chapter 8 to develop a damping model based on an elliptic cylinder approximation. Predictions are made from the resulting

model regarding the sensitivity of nonlinear measurements to changes in fluid properties.

Finally, in Chapter 9, conclusions are presented with a summary of the contributions, discussion of study limitations and implications, and suggestions for future work.

1.9. References

1. Kim, K.H. et al. 'A skew-symmetric cantilever accelerometer for automotive airbag applications', *Sensors and Actuators A: Physical*, **50** (1-2), 1995, pp. 121-126.
2. Lang, H.P. et al. 'A chemical sensor based on a micromechanical cantilever array for the identification of gases and vapors', *Applied Physics A: Material Science & Processing*, **66** (1), 1998, pp. S61-S64.
3. Lavrik, N.V., Sepaniak, M.J., Datskos, P.G. 'Cantilever transducers as a platform for chemical and biological sensors', *Review of Scientific Instruments*, **75** (7), 2004, pp. 2229-2253.
4. Raiteri, R. et al. 'Micromechanical cantilever-based biosensors', *Sensors and Actuators B: Chemical*, **79** (2-3), 2001, pp. 115-126.
5. Greywall, D.S., 'Micromechanical RF filters excited by the Lorentz force', *Journal of Micromechanics and Microengineering*, **9** (1), 1999, pp. 78-84.
6. Wang, K., Nguyen, C. T.-C. 'High-order micromechanical electronic filters', *Proceedings of the 1997 IEEE International Micro Electro Mechanical Workshop*, Nagoya, Japan, 1997, pp. 25-30.
7. Lee, S.I. et al. 'Nonlinear dynamics of microcantilevers in tapping mode atomic force microscopy: A comparison between theory and experiment', *Physics Review B*, **66** (11), 2002.
8. Beeby, S. *MEMS mechanical sensors*. London: Artech House, 2004.
9. Atkinson, C., Manrique de Lara, M. 'The frequency response of a rectangular cantilever plate vibrating in a viscous fluid', *Journal of Sound and Vibration*, **300** (1-2), 2007, pp. 352-367.
10. Harrison, C. et al. 'A MEMS sensor for the measurement of density-viscosity for oilfield applications', *Proceedings of SPIE, 21-26th January*. Photonics West 2006: MOEMS, MEMS, Micro and Nanofabrication, San Jose, USA, 2006.
11. Shih, W.Y. et al. 'Simultaneous liquid viscosity and density determination with piezoelectric unimorph cantilevers', *Journal of Applied Physics*, **89**(2), 2001.
12. Zribi, A. et al, 'Micromachined resonant multiple gas sensor', *Sensors and Actuators*, **A(122)**, 2005, pp.31-38.
13. Ronaldson, K.A. et al. 'Transversely oscillating MEMS viscometer: The "Spider"', *International Journal of Thermophysics*, **27**(6), 2006, pp.1677-1695.
14. Conrad, B.P. et al. 'Can synovial fluid viscosity be used as a physical marker for osteoarthritis sensitivity?', Summer Bioengineering Conference 2003, Key Biscayne, Florida, USA, 2003.
15. Rhoads, J.H. *Exploring and exploiting resonance in coupled and/or nonlinear microelectromechanical oscillators*. PhD Thesis. Michigan State University, USA, 2007.
16. Sivebaek, I.M., Jakobsen, J. 'The viscosity of dimethyl ether', *Tribology International*, **40**, 2007, pp. 652-658.
17. Rao, S.S. *Mechanical vibrations*. 4th ed. Pearson Prentice Hal, 2004.
18. Braghin F. et al. 'Nonlinear dynamics of vibrating MEMS', *Sensors and Actuators*, **A (134)**, 2007, pp. 98-108.
19. Harrison, C. et al. 'Operation of a Vibrating Wire Viscometer at Viscosities Greater than 0.2 Pa.s: Results for a Certified Reference Fluid with Nominal Viscosity at $T= 273$ K and $p= 0.1$ MPa of 0.652 Pa.s while Stagnant and a Fluid

- of Nominal Viscosity of 0.037 Pa.s while Flowing’, *Journal of Chemical and Engineering Data*, **52** (3), 2007, pp. 774-782.
20. Lin, Z.X. et al. ‘Operation of an ultrasensitive 30-MHz quartz-crystal microbalance in liquids’, *Analytical Chemistry*, **65** (11), 1993, pp.1546-1551.
 21. Agoston, A., Keplinger, F., Jakoby, B. ‘Evaluation of a vibrating micromachined cantilever sensor for measuring the viscosity of complex organic liquids’, *Sensors and Actuators, A* (123-124), 2005, pp. 82-86.
 22. Loisel, K.T., Grimes, C.A. ‘Viscosity measurements of viscous liquids using magnetoelastic thick-film sensors’, *Review of Scientific Instruments*, **71**(3), 2000, pp.1441-1446.
 23. Sader, J.E. ‘Frequency response of cantilever beams immersed in viscous fluids with application to the atomic force microscope’, *Journal of Applied Physics*, **84** (1), 1998, pp. 64-76.
 24. Van Eysden, C.A, Sader, J.E. ‘Small amplitude oscillations of a flexible thin blade in a viscous fluid: Exact analytical solution.’, *Physics of fluids*, **18**, 2006, 123102-1 – 11.
 25. Younis, M.I., Nayfeh, A.H. ‘A study of the nonlinear response of a resonant microbeam to an electric actuation’, *Nonlinear Dynamics*, **31** (1), 2003, pp. 91-117.
 26. Abdel-Rahman, E.M., Nayfeh, A.H. ‘Secondary resonances of electrically actuated resonant microsensors’, *Journal of Micromechanics and Microengineering*, **13** (3), 2003, pp. 491-501.
 27. Kaajakari, V. et al. ‘Nonlinear limits for single crystal silicon microresonators’, *Journal of Microelectromechanical Systems*, **13** (5), 2004, pp. 715-724.
 28. Li, H. et al. ‘Nonlinear free and forced oscillations of piezoelectric microresonators’, *Journal of Micromechanics and Microengineering*, **16** (2), 2006, pp. 356-367.
 29. De, S.K., Aluru, N.R. ‘Complex oscillations and chaos in electrostatic microelectromechanical systems under superharmonic excitations’, *Physical Review Letters*, **94**, 2005, 204101.
 30. Buks, E; Yurke, B. ‘Mass detection with a nonlinear nanomechanical resonator’, *Physical Review E*, **74** (4), 2006, 046619.
 31. Rhoads, J.F., Shaw, S.W., Turner, K, L. ‘Nonlinear dynamics and its applications in micro- and nanoresonators’, *Journal of Dynamic Systems, Measurement and Control – Transactions of the ASME*, **132** (3), 2010, 034001..
 32. Thomsen, J.J. *Vibrations and Stability: Advanced theory, analysis and tools*. 2nd ed. Springer, 2003.
 33. Emam, S. A. *A Theoretical and Experimental study of Nonlinear Dynamics of Buckled Beams*. PhD Thesis. Virginia Polytechnic Institute and State University, USA, 2002.
 34. Fidlin, A. *Nonlinear oscillations in mechanical engineering*. Berlin: Springer, 2006.
 35. Malatkar, P. *Nonlinear vibrations of cantilever beams and plates*. PhD Thesis. Virginia Polytechnic Institute and State University, USA, 2003.
 36. Braginsky, V.B, Mitrofanov, V.P., Panov, V.I. *Systems with small dissipation*. Chicago: University of Chicago Press, 1985.
 37. Timoshenko, S. *Vibration problems in engineering*. Princeton: Van Nostrand Co., 1955.

38. Mestrom, R.M.C. et al. 'Simulations and experiments of hardening and softening resonances in a clamped-clamped beam MEMS resonator', *Sensors and Actuators A: Physical*, **162**, 2010, pp. 225-234.
39. Rhoads, J.F., Shaw, S.W., Turner, K, L. 'The nonlinear response of resonant microbeam systems with purely-parametric electrostatic actuation', *Journal of Micromechanics and Microengineering*, **16**, 2006, pp. 890-899.
40. Veijola, T., Mattila, T. 'Modeling of nonlinear micromechanical resonators and their simulation with the harmonic-balance method', *International Journal of RF and Microwave Computer-Aided Engineering*, **11**, 2001, pp. 310–321.
41. Tadayan, M.A. et al. 'Nonlinear dynamics of microresonators', *Journal of Physics: Conference series*, **34**, 2006, pp 961-966.
42. Xie, W.C., Lee, H.P., Lim S.P. 'Normal modes of a non-linear clamped-clamped beam', *Journal of Sound and Vibration*, **250** (2), 2002, pp.339-349.
43. Marur, S.R. 'Advances in nonlinear vibration analysis of structures. Part I. Beams', *Sadhana*, **26** (3), 2001, pp. 243-249.
44. Yang, Y.T. et al. 'Zeptogram-sclae nanomechanical mass sensing', *Nano Letters*, **6** (4), 2006, pp. 583-586.
45. Goeders, K.M., Colton, J.S., Bottomley, L.A. 'Microcantilevers: Sensing chemical interactions via mechanical motion', *Chemical Reviews*, **108** (2), 2008, pp. 522-542.
46. Greywall, D.S. 'Sensitive magnetometer incorporating a high-Q nonlinear mechanical resonator', *Measurement Science and Technology*, **16**, 2005, pp. 2473-2482.
47. Sullivan, M. et al. 'On the nonlinear interpretation of a vibrating wire viscometer operated at large amplitude', *Fluid phase equilibria*, **276** (2), 2009, pp. 99-107.

Chapter 2

Beam kinematics

In this chapter, the equation of motion for a transversely oscillating clamped-clamped beam in vacuum is derived. A variational approach is taken employing the Hamilton principle. Nonlinearities, temperature effects and simplifying assumptions are discussed and evaluated prior to and/or during the derivation. Finally, intrinsic damping mechanisms are described and evaluated.

2.1. Dominant nonlinearity

The various nonlinearities which may occur in MEMS devices have been outlined in section 1.4.3. For a transversely oscillating clamped-clamped beam, providing strains remain small and the beam material is Hookean, then the primary nonlinearities to consider are geometric. The differential equations of motion for an extensional beam will include nonlinear contributions to the curvature and inertia, with another nonlinearity due to midplane stretching. Crespo da Silva [1] showed that the midplane stretching is the dominant nonlinearity, allowing for the linearisation of curvature and inertial terms with no significant effect on analysis of the system.

2.2. Temperature effects

2.2.1. Tension

A clamped-clamped beam may be subject to an initial tension. Depending upon the boundary conditions, this tension can increase or decrease with a change in temperature. To account for this tension, suppose that a clamped-clamped beam of length L has its supports a distance $(1 + \eta)L$ apart, where η is a small initial stretch of the beam and $|\eta| \ll 1$. For $\eta > 0$ the beam is pre-tensioned, whereas for $\eta < 0$ the beam is pre-compressed.

2.2.2. Beam dimensions

An increase in temperature will lead to an increase in beam dimensions. In turn, this may have some effect on beam behaviour. The degree to which beam expansion (or contraction for temperature decrease) affects beam behaviour depends upon the size of the temperature change and the beam material properties.

Consider for example a silicon beam. At a temperature of 300K, silicon has a linear thermal expansion coefficient α_L of 2.616×10^{-6} [2]. Although this coefficient is temperature dependent, it can be reasonably approximated to show that temperature fluctuations of even ± 50 K about the 300K point make only a negligible difference to beam dimensions.

To illustrate, suppose the silicon beam has length $L = 1500 \mu\text{m}$ at 20°C , then is heated to 40°C . The change in beam length is calculated using $\frac{\Delta L}{L} = \alpha_L \Delta T$, where ΔL is the change in length and ΔT the change in temperature. Inserting the numerical values gives a predicted increase in length of 0.0052%. For the purpose of this work then, the effect of temperature on beam dimensions may be disregarded. This assumption is confirmed in section 8.1.3.

2.3. Beam theory

In order to approximate the behaviour of a clamped-clamped beam, Euler-Bernoulli beam theory is employed. This theory makes certain general assumptions which are found to be approximately true for most beams. It applies particularly to slender beams, whose length is far greater than width or depth.

2.3.1. Euler-Bernoulli theory

The analysis of a thin beam undergoing small flexural vibrations can be simplified by using Euler-Bernoulli theory, in which shear effects, longitudinal inertia and rotary inertia are ignored [3]. Providing certain conditions are met, the theory allows for the neglect of warping and shear deformation. In turn, a differential beam element may be considered a body whose motion is completely described by three translational and three rotational displacements. Knowledge of the deformation of the

beam centerline allows for the determination of the deformation of any point on the beam [4]. The conditions are as follows [5,6].

1. The beam is long and slender i.e. beam length is far greater than beam width and depth. As a consequence, tensile/compressive stresses perpendicular to the beam are much smaller than tensile/compressive stresses parallel to the beam.
2. The beam is initially straight with a uniform cross section along the beam length.
3. The beam has an axis of symmetry in the plane of bending.
4. The beam is subject to pure bending i.e. the shear force is zero and there are no torsional or axial loads.
5. The beam material is isotropic and homogeneous.
6. The material obeys Hooke's law, i.e. it is linearly elastic and there is no plastic deformation.
7. Plane sections of the beam remain plane during bending.
8. Deformations remain small, such that the radius of curvature of the bent beam is large compared to the beams depth.

Although real structures never exactly meet these conditions, they are often approximately true enough to allow the theory to make useful predictions. Euler-Bernoulli theory does not hold for thick and short beams, where it is necessary to use the Timoshenko model instead [7].

2.3.2. Bending and curvature

Consider the centreline of a uniform beam, curved due to in-plane loading. Let θ be the slope angle of the tangent to the curve at any point, and s be the arc length of the curve measured from an arbitrary starting point (see figure 2.1). The curvature of

a planar curve is then defined as $\kappa = \frac{d\theta}{ds}$.

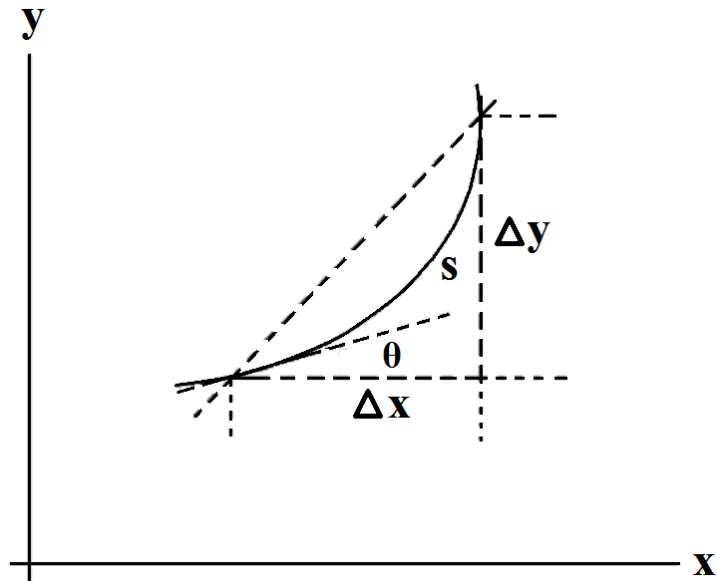


Figure 2.1: Curvature

Consider a differential element of the curve as illustrated in figure 2.2, where x and y are local axes.

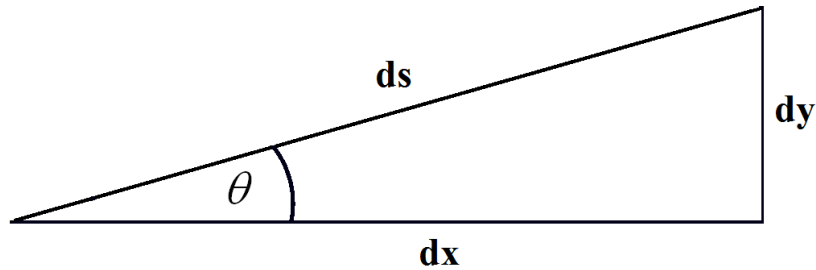


Figure 2.2: Differential element of curve

By inspection $\tan \theta = \frac{dy}{dx}$, which yields $\frac{d\theta}{dx} = \frac{\frac{d^2 y}{dx^2}}{\left(\frac{ds}{dx}\right)^2}$.

Also, $ds = (dx^2 + dy^2)^{1/2} = \left[1 + \left(\frac{dy}{dx}\right)^2\right]^{1/2} dx$.

Therefore $\kappa = \frac{d\theta}{ds} = \frac{d\theta}{dx} \frac{dx}{ds} = \frac{\frac{d^2 y}{dx^2}}{\left[1 + \left(\frac{dy}{dx}\right)^2\right]^{3/2}}$.

For small rotations, $\left(\frac{dy}{dx}\right)^2 \ll 1$. In this case, the curvature can be linearly approximated as $\kappa = \frac{d^2y}{dx^2}$. For larger, finite rotations, the true nonlinear curvature term should be adopted.

Euler-Bernoulli theory assumes that the following relationship exists between bending moment and beam curvature: $\kappa = \frac{M}{EI}$, where M , E and I denote the bending moment, Young's modulus of the beam material and second moment of area respectively. The bending potential energy in a beam of length L is given by $U_B = \int_0^L \frac{1}{2} EI \kappa^2 dx$.

2.3.3. Second moment of area

The resistance to bending of a body is proportional to the second moment of area. For the beam cross section illustrated in figure 2.3, the second moment of area about the z axis is given by $I_z = \int_A y^2 dA$, where dA is an elemental area and y is the perpendicular distance to the element dA from the axis z . On computing, $I_z = \int \int_A y^2 dydz = \frac{bd^3}{12}$, where b is the beam width and d the beam depth.

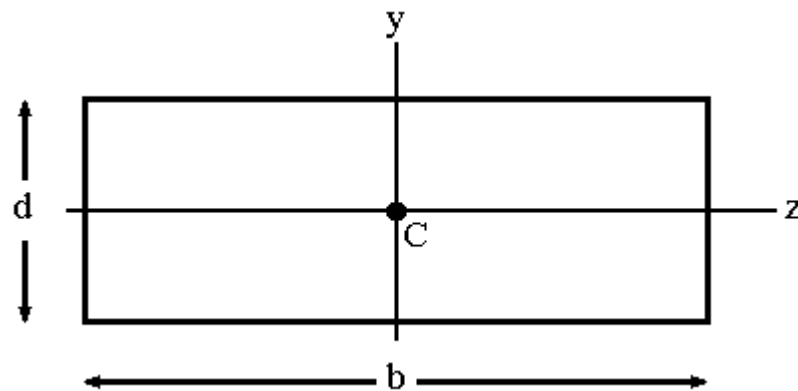


Figure 2.3: Second moment of area about z-axis

2.4. Equation of motion

Consider a uniform clamped-clamped beam of length L , width b and depth d as shown in figure 2.4. The displacements in each direction correspond to $u(x)$, $v(y)$, $w(z)$.

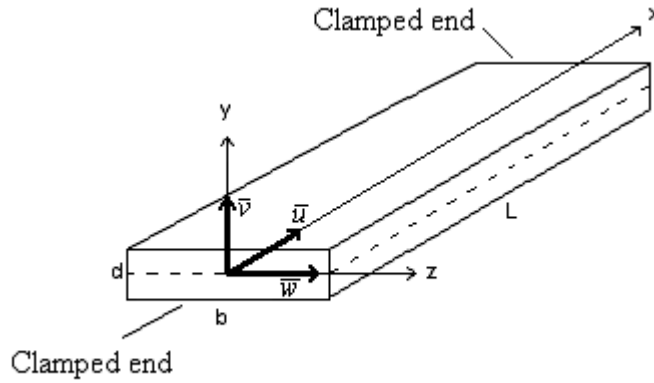


Figure 2.4: Transverse vibration of slender clamped-clamped beam

For transverse displacement in the y -direction to be possible, the beam has to stretch axially as well as bend. Stretching of the beam's midplane can therefore be expected to contribute to the transverse stiffness of the beam [8].

Now consider the centre line of the beam, running parallel to the x axis. Let \bar{u} and \bar{v} represent displacement on the centre line of the beam, where \bar{u} is longitudinal extension and \bar{v} transverse extension. In addition to the slender beam assumptions outlined in the previous section, it is also assumed that extensions are small with $\bar{v} \gg \bar{u}$, such that $\bar{u} = O(\bar{v}^2)$ [8,9].

2.4.1. Axial strain

During transverse vibrations a beam element will be deformed and deflected. Suppose the length of the centre line in the element then changes from ds to ds^* (see figure 2.5). The axial strain on the centre line, $\bar{\varepsilon}_{xx}$, is then calculated as

$$\bar{\varepsilon}_{xx} = \frac{ds^* - ds}{ds} = \frac{\sqrt{(dx + d\bar{u})^2 + d\bar{v}^2} - dx}{dx} . \quad \text{Let } \bar{u}' = d\bar{u}/dx \quad \text{and} \quad \bar{v}' = d\bar{v}/dx , \quad \text{then}$$

$$\bar{\varepsilon}_{xx} = \sqrt{(1 + \bar{u}')^2 + (\bar{v}')^2} - 1 .$$

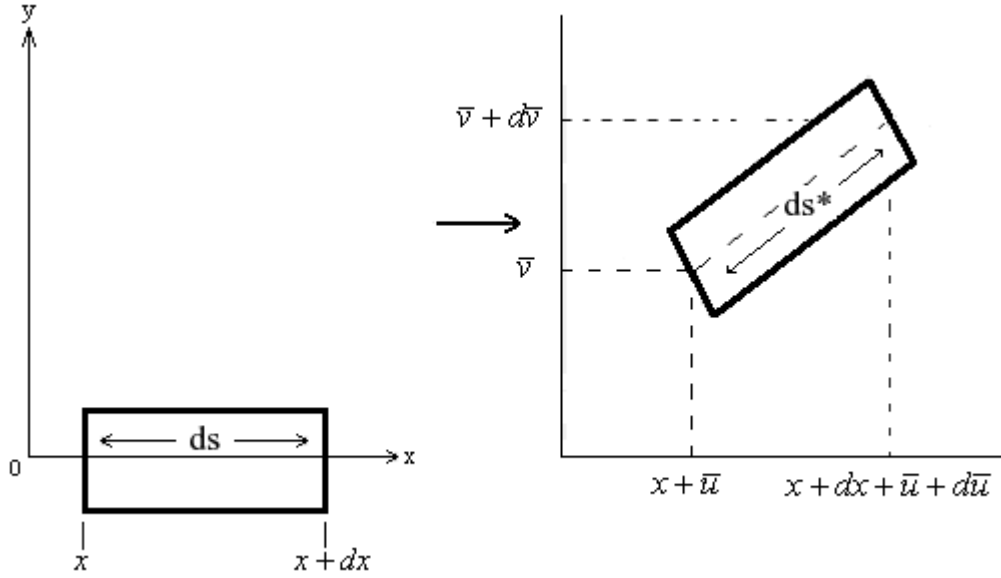


Figure 2.5: Deformation of differential beam element

Now $\sqrt{(1 + \bar{u}')^2 + (\bar{v}')^2} = \{1 + 2\bar{u}' + \bar{u}'^2 + \bar{v}'^2\}^{1/2}$. Employing a binomial series expansion and retaining only the larger terms, it is possible to then write $\bar{\varepsilon}_{xx} \approx 1 + \frac{1}{2}(2\bar{u}' + \bar{u}'^2 + \bar{v}'^2) - 1 = \frac{1}{2}(2\bar{u}' + \bar{u}'^2 + \bar{v}'^2)$. As it has been assumed that $\bar{u} = O(\bar{v}^2)$, so the term \bar{u}'^2 may be neglected in this formula, resulting in the approximation $\bar{\varepsilon}_{xx} \approx \frac{1}{2}(2\bar{u}' + \bar{v}'^2) = \frac{d\bar{u}}{dx} + \frac{1}{2}\left(\frac{d\bar{v}}{dx}\right)^2$. (2.1)

Now consider elemental fibres parallel to, but displaced from, the centre line. For these fibres, the strain is reduced by an amount proportional to the y displacement from the centre line (see figure 2.6). Note that Euler-Bernoulli theory assumes that normals to the centre line remain normal under deformation. The gradient of a normal to the centre line is $-\frac{dx}{d\bar{v}}$. If the axial displacement on the centre line is \bar{u} , then away from the centre line the displacement u is given by $u = \bar{u} - y \frac{d\bar{v}}{dx}$. With this reduction in displacement, so the strain along the x-axis direction is reduced. Let the reduction in strain be expressed $\partial\varepsilon = \frac{u - \bar{u}}{\partial x} = \frac{1}{\partial x}\left(-y \frac{d\bar{v}}{dx}\right)$. As $\partial x \rightarrow 0$ so the reduction

in strain becomes $-y \frac{d^2 \bar{v}}{dx^2}$. Therefore the axial strain on any fibre in the beam, ϵ_{xx} ,

$$\text{can be represented as } \epsilon_{xx} \approx \frac{d\bar{u}}{dx} + \frac{1}{2} \left(\frac{d\bar{v}}{dx} \right)^2 - y \frac{d^2 \bar{v}}{dx^2} \quad (2.2)$$

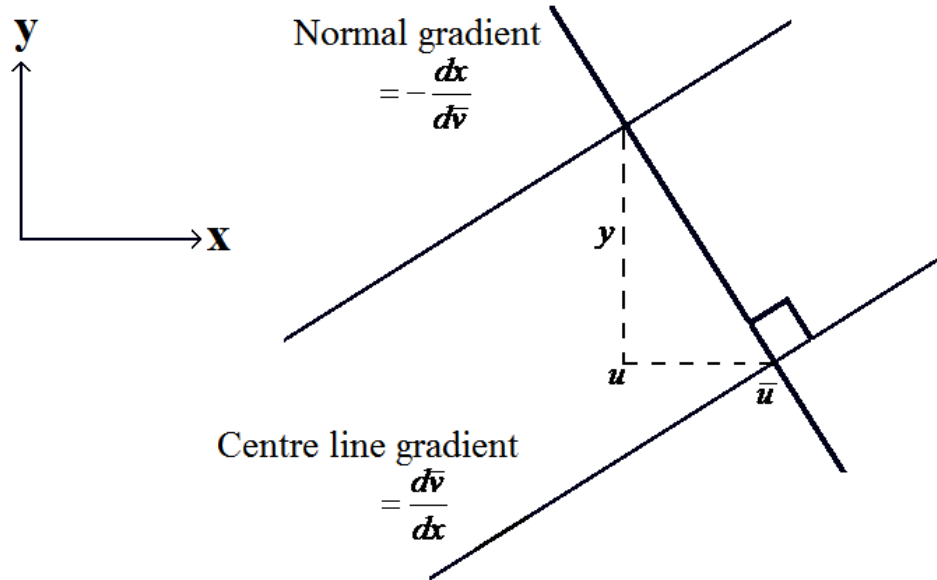


Figure 2.6: Displacements away from centre line

2.4.2. Kinetic energy

With the assumption for a slender beam that all mass is concentrated on the centre line, the kinetic energy T of the vibrating beam is given by

$$T = \int_0^L \frac{\rho A}{2} \left[\left(\frac{d\bar{u}}{dt} \right)^2 + \left(\frac{d\bar{v}}{dt} \right)^2 \right] dx, \text{ where } \rho \text{ is the beam material density and } A \text{ the cross-}$$

sectional area of the beam ($=bd$ in this case).

2.4.3. Potential Energy

The potential strain energy in the vibrating beam is calculated by first considering the strain energy density $U_0 = \int_0^{\epsilon_{xx}} E \epsilon_{xx} d\epsilon_{xx} = \frac{1}{2} E \epsilon_{xx}^2$. The strain energy U is then

given by $U = \int_V U_0 dV = \int_{AL} U_0 dA dx$. Substituting and rearranging gives

$$U = \int_L \frac{1}{2} EA \left[\frac{d\bar{u}}{dx} + \frac{1}{2} \left(\frac{d\bar{v}}{dx} \right)^2 \right]^2 dx + \int_L \frac{1}{2} EI \left[\left(\frac{d^2\bar{v}}{dx^2} \right)^2 \right] dx - \iint_{AL} E \left[\frac{d\bar{u}}{dx} + \frac{1}{2} \left(\frac{d\bar{v}}{dx} \right)^2 \right] \left[\frac{d^2\bar{v}}{dx^2} \right] y dA dx$$

where I is the second moment of area about the z axis. Now $\int_A y dA = 0$, meaning

$$\text{that the expression reduces to } U = \int_L \frac{1}{2} EA \left[\frac{d\bar{u}}{dx} + \frac{1}{2} \left(\frac{d\bar{v}}{dx} \right)^2 \right]^2 dx + \int_L \frac{1}{2} EI \left[\left(\frac{d^2\bar{v}}{dx^2} \right)^2 \right] dx.$$

The first term in this expression is the potential energy due to midplane stretching, whereas the second term represents the linearised bending potential energy.

2.4.4. Hamilton's principle

The differential equations of motion for the beam can be obtained from a variational approach using Hamilton's principle. This can be written $\int_{t_1}^{t_2} \delta(T - U) dt + \int_{t_1}^{t_2} \delta W_{nc} dt = 0$, where δ is the first variation operator, T is the total kinetic energy of the system, U is the potential energy, and δW_{nc} is the virtual work done by the non-conservative forces and/or moments. For a beam in a vacuum, the non-conservative forces are taken to be zero, such that $\int_{t_1}^{t_2} \delta(T - U) dt = 0$.

The variations in kinetic energy and potential energy are then given by

$$\delta T = \int_0^L \frac{\rho A}{2} \left[\frac{d\bar{u}}{dt} \delta \left(\frac{d\bar{u}}{dt} \right) + \frac{d\bar{v}}{dt} \delta \left(\frac{d\bar{v}}{dt} \right) \right] dx \text{ and}$$

$$\delta U = \int_L \frac{EA}{2} \left[\frac{d\bar{u}}{dx} + \frac{1}{2} \left(\frac{d\bar{v}}{dx} \right)^2 \right] \left[\delta \frac{d\bar{u}}{dx} + \frac{d\bar{v}}{dx} \delta \left(\frac{d\bar{v}}{dx} \right) \right] dx + \int_L \frac{EI}{2} \frac{d^2\bar{v}}{dx^2} \delta \left(\frac{d^2\bar{v}}{dx^2} \right) dx$$

$$\text{Consider the kinetic energy: } \int_{t_1}^{t_2} \delta T dt = \int_{t_1}^{t_2} \int_0^L \frac{\rho A}{2} \left[\frac{d\bar{u}}{dt} \delta \left(\frac{d\bar{u}}{dt} \right) + \frac{d\bar{v}}{dt} \delta \left(\frac{d\bar{v}}{dt} \right) \right] dx dt .$$

Separating integrals, reversing the order of integration then integrating by parts gives

$$\int_{t_1}^{t_2} \delta T dt = \frac{\rho A}{2} \int_0^L \left\{ \left[\frac{d\bar{u}}{dt} \delta \bar{u} \right]_{t_1}^{t_2} - \int_{t_1}^{t_2} \frac{d^2\bar{u}}{dt^2} \delta \bar{u} dt \right\} dx + \frac{\rho A}{2} \int_0^L \left\{ \left[\frac{d\bar{v}}{dt} \delta \bar{v} \right]_{t_1}^{t_2} - \int_{t_1}^{t_2} \frac{d^2\bar{v}}{dt^2} \delta \bar{v} dt \right\} dx$$

By definition for Hamilton's principle, $\delta\bar{u}$ and $\delta\bar{v}$ are both zero at t_1 and t_2 .

$$\text{Therefore } \int_{t_1}^{t_2} \delta T dt = -\frac{\rho A}{2} \int_0^L \int_{t_1}^{t_2} \frac{d^2 \bar{u}}{dt^2} \delta \bar{u} dt dx - \frac{\rho A}{2} \int_0^L \int_{t_1}^{t_2} \frac{d^2 \bar{v}}{dt^2} \delta \bar{v} dt dx.$$

Now consider the potential energy:

$$\int_{t_1}^{t_2} \delta U dt = \int_{t_1}^{t_2} \left\{ \int_L \frac{EA}{2} \left[\frac{d\bar{u}}{dx} + \frac{1}{2} \left(\frac{d\bar{v}}{dx} \right)^2 \right] \left[\delta \frac{d\bar{u}}{dx} + \frac{d\bar{v}}{dx} \delta \left(\frac{d\bar{v}}{dx} \right) \right] dx + \int_L \frac{EI}{2} \frac{d^2 \bar{v}}{dx^2} \delta \left(\frac{d^2 \bar{v}}{dx^2} \right) dx \right\} dt$$

Separating the integrals and integrating by parts yields

$$\begin{aligned} \int_{t_1}^{t_2} \delta U dt &= -\int_{t_1}^{t_2} \left\{ \int_0^L \frac{d}{dx} \frac{EA}{2} \left[\frac{d\bar{u}}{dx} + \frac{1}{2} \left(\frac{d\bar{v}}{dx} \right)^2 \right] \delta \bar{u} dx \right\} dt - \int_{t_1}^{t_2} \int_0^L \frac{d}{dx} \left\{ \frac{EA}{2} \left[\frac{d\bar{u}}{dx} + \frac{1}{2} \left(\frac{d\bar{v}}{dx} \right)^2 \right] \frac{d\bar{v}}{dx} \right\} \delta \bar{v} dx dt \\ &+ \int_{t_1}^{t_2} \int_0^L \frac{EI}{2} \frac{d^4 \bar{v}}{dx^4} \delta \bar{v} dx dt \end{aligned}$$

Hamilton's principle then requires that $\int_{t_1}^{t_2} (\delta T - \delta U) dt = 0$, that is

$$\int_{t_1}^{t_2} \left\{ \int_0^L \rho A \frac{d^2 \bar{u}}{dt^2} \delta \bar{u} dx + \int_0^L \rho A \frac{d^2 \bar{v}}{dt^2} \delta \bar{v} dx - \int_0^L \frac{d}{dx} EA \left[\frac{d\bar{u}}{dx} + \frac{1}{2} \left(\frac{d\bar{v}}{dx} \right)^2 \right] \delta \bar{u} dx \right. \\ \left. - \int_0^L \frac{d}{dx} \left\{ EA \left[\frac{d\bar{u}}{dx} + \frac{1}{2} \left(\frac{d\bar{v}}{dx} \right)^2 \right] \frac{d\bar{v}}{dx} \right\} \delta \bar{v} dx + \int_0^L EI \frac{d^4 \bar{v}}{dx^4} \delta \bar{v} dx \right\} dt = 0$$

Consider $\delta\bar{u}$ terms: $\int_0^L \rho A \frac{d^2 \bar{u}}{dt^2} dx - \int_0^L \frac{d}{dx} EA \left[\frac{d\bar{u}}{dx} + \frac{1}{2} \left(\frac{d\bar{v}}{dx} \right)^2 \right] dx = 0$. With the

assumption that longitudinal inertia is negligible, then $\int_0^L \rho A \frac{d^2 \bar{u}}{dt^2} dx = 0$. This implies

that $\frac{d}{dx} \left\{ EA \left[\frac{d\bar{u}}{dx} + \frac{1}{2} \left(\frac{d\bar{v}}{dx} \right)^2 \right] \right\} = 0$. On integration, $EA \left[\frac{d\bar{u}}{dx} + \frac{1}{2} \left(\frac{d\bar{v}}{dx} \right)^2 \right] = N$ where N

is some constant. Therefore it follows that $\int_0^L N dx = EA \int_0^L \left[\frac{d\bar{u}}{dx} + \frac{1}{2} \left(\frac{d\bar{v}}{dx} \right)^2 \right] dx$, which

yields $NL = EA \left\{ \left[\bar{u} \right]_0^L + \frac{1}{2} \int_0^L \left(\frac{d\bar{v}}{dx} \right)^2 dx \right\}$. Suppose now that the beam supports are fixed

at a distance of $(1+\eta)L$ apart. Letting the boundary condition at L be $u(L,t)=\eta L$,

$$\text{then } N = EA \left(\eta + \frac{1}{2L} \int_0^L \left(\frac{d\bar{v}}{dx} \right)^2 dx \right).$$

Now consider the $\delta\bar{v}$ terms:

$$\int_0^L \rho A \frac{d^2\bar{v}}{dt^2} dx - \int_0^L \frac{d}{dx} \left\{ EA \left[\frac{d\bar{u}}{dx} + \frac{1}{2} \left(\frac{d\bar{v}}{dx} \right)^2 \right] \frac{d\bar{v}}{dx} \right\} dx + \int_0^L EI \frac{d^4\bar{v}}{dx^4} dx = 0$$

$$\text{This can be rewritten as } \int_0^L \left\{ \rho A \frac{d^2\bar{v}}{dt^2} - N \frac{d^2\bar{v}}{dx^2} + EI \frac{d^4\bar{v}}{dx^4} \right\} dx = 0.$$

Therefore the equation of motion for the free vibrations of the beam in a vacuum becomes

$$\rho A \frac{d^2\bar{v}}{dt^2} - EA \left(\eta + \frac{1}{2L} \int_0^L \left(\frac{d\bar{v}}{dx} \right)^2 dx \right) \frac{d^2\bar{v}}{dx^2} + EI \frac{d^4\bar{v}}{dx^4} = 0 \quad (2.3)$$

2.5. Intrinsic damping

The analysis to this point has yet to account for any of the intrinsic damping mechanisms outlined in section 1.4.4. As Bishop and Johnson [10] discussed, it is difficult to know the magnitude of these damping forces with great accuracy. In the presence of fluid damping this problem is compounded. Hao et al [11] suggested that for a beam resonator operating in a vacuum, the sources of energy loss mainly consist of support loss, thermoelastic loss and surface loss. By estimating the quality factor relating to each of these loss mechanisms, Q_{sup} , Q_{TED} and Q_{surf} respectively, the overall quality factor Q_{int} due to intrinsic losses is given by

$$\frac{1}{Q_{\text{int}}} = \frac{1}{Q_{\text{sup}}} + \frac{1}{Q_{\text{TED}}} + \frac{1}{Q_{\text{surf}}}.$$

2.5.1. Support loss

An analytical model for support loss is presented by Hao et al [11]. An elastic wave is taken to be excited by a vibrating shear force at the clamped ends, which is propagated in the support structure. This model depends on the following assumptions:

1. Dimensions of the supports in the x-y plane are much larger than the beam dimensions.
2. The wavelength λ_T of the transverse elastic wave is far greater than the width b of the beam.
3. Beam vibration is described using Euler-Bernoulli theory.
4. The behaviour of the supports is described using 2D elastic wave theory, and supports are modelled as infinite thin plates of width b .
5. All of the vibration energy entering the support structure is considered to be lost.

The transverse wavelength λ_T can be expressed as $\lambda_T = \frac{C_T}{f}$, where C_T is the propagation velocity for transverse waves, and f is the resonant frequency of the beam. C_T is given by $C_T^2 = \frac{E}{2\rho(1+\nu)}$, where ν is Poisson's ratio. If the elastic wavelength is also very large when compared to beam length, then the quality factor associated with support loss can be estimated using the following formula:

$$Q_{\text{sup}} = \frac{4.86}{(3-\nu)(1+\nu)} \frac{1}{(\beta_n \chi_n)^2} \left[\frac{L}{d} \right]^3 \cdot \beta_n$$
 and χ_n are, respectively, mode constants and mode shape factors. For a clamped-clamped beam vibrating in its first mode, these have the value $\beta_1 = 1.5056$ and $\chi_1 = -0.983$.

2.5.2. Thermoelastic damping (TED)

In a vibrating structure, compressed regions become hotter and extended regions cooler, creating a temperature gradient in most materials. This is a consequence of the strain field causing changes in internal energy. Should any irreversible heat flow then occur, so energy is dissipated. This process is known as thermoelastic damping, or TED for short. A study of TED in vibrating beams was first presented by Zener [12], who noted that alternating compressive and tensile strains build up on opposing sides of the beam's neutral axis, resulting in energy loss. Developing on from Zener's work, Lifshitz and Roukes [13] presented the following formula for estimating Q_{TED} :

$$\frac{1}{Q_{TED}} = \frac{E\alpha_T^2 T}{C_p \rho} \left\{ \frac{6}{\zeta^2} - \frac{6}{\zeta^3} \cdot \frac{\sinh(\zeta) + \sin(\zeta)}{\cosh(\zeta) + \cos(\zeta)} \right\}, \text{ where } \zeta = d \sqrt{\frac{\omega \rho C_p}{2\kappa_T}},$$

T is the absolute temperature, C_p the specific heat at constant pressure, κ_T the thermal conductivity, and ω the angular frequency of the resonator.

2.5.3. Surface damping

It has been experimentally observed that the quality factor of micro- and nano-scale resonators decreases as surface-to-volume ratios increase. This dependence on dimension is believed to indicate the presence of surface loss mechanisms. The precise nature of these mechanisms has yet to be determined, although much of the literature attributes the losses to surface imperfections, adsorbents or oxidation [14,15,16,17,18,19]. It has been observed that surface treatments may reduce surface losses by reducing surface roughness [11,15,20,21].

For an approximation of the magnitude of surface losses, an analytic model is required. Yang et al [15] presented a formula for determining the quality factor associated with surface losses: $Q_{surf} = \frac{bd}{3b+d} \frac{E}{2E_{ds}\delta_s}$, where E_{ds} is the dissipation value of the Young's modulus of the surface layer, and δ_s is the thickness of the surface layer. As Hao et al [11] discuss however, it is very difficult to know the values of E_{ds} and δ_s . They proposed an experimentally determined value $E_{ds}\delta_s = 1.38$ for beams of width 20 μm and varying lengths and depths. Using

this formula and empirically determined values then allows for a rough approximation to the contribution of surface losses to the total intrinsic damping.

2.5.4. Equation of motion with intrinsic damping

Making the assumption that the intrinsic damping mechanisms are viscous in nature i.e. proportional to $\frac{d\bar{v}}{dt}$, the equation of motion for the free vibrations of the beam in a vacuum is modified to

$$\rho A \frac{d^2 \bar{v}}{dt^2} - EA \left(\eta + \frac{1}{2L} \int_0^L \left(\frac{d\bar{v}}{dx} \right)^2 dx \right) \frac{d^2 \bar{v}}{dx^2} + EI \frac{d^4 \bar{v}}{dx^4} + c_I \frac{d\bar{v}}{dt} = 0 \quad (2.4)$$

where c_I is an intrinsic damping coefficient.

2.6. References

1. Crespo da Silva, M.R.M. 'Non-linear-flexural-torsional-extensional dynamics of beams II. Response analysis', *International Journal of Solids and Structures A* (134), 1988, pp. 98-108.
2. Hull, R. *Properties of crystalline silicon [electronic resource]*. London: INSPEC, the Institution of Electrical Engineers, c1999.
3. King, J.L. 'The free transverse vibrations of anisotropic beam', *Journal of Sound and Vibration*, **98** (4), 1985, pp. 575-585.
4. Malatkar, P. *Nonlinear vibrations of cantilever beams and plates*. PhD Thesis. Virginia Polytechnic Institute and State University, USA, 2003.
5. Shigley, J., Mischke, C., Budynas, R. *Mechanical Engineering Design*, London: McGraw-Hill, 2004.
6. Parnes, R. 'On the accuracy of linear beam theory', *AIAA Journal*, **17** (2), 1979, pp. 219-220.
7. Sun, Y., Fang, D., Soh, A.K. 'Thermoelastic damping in micro-beam resonators', *International journal of solids and structures*, **43**, 2006, pp. 3213-3229.
8. Thomsen, J.J. *Vibrations and Stability: Advanced theory, analysis and tools*. 2nd ed. Springer, 2003.
9. Nayfeh, A.H., Mook, D.T. *Nonlinear oscillations*. Weinheim: Wiley-VCH, 2004.
10. Bishop, R.E.D., Johnson, D.C., *The mechanics of vibration*. Cambridge [Eng.] University Press, 1960.
11. Hao, Z., Erbil, A., Ayazi, F. 'An analytical model for support loss in micromachined beam resonators with in-plane flexural vibrations', *Sensors and Actuators A*, **109**, 2003.
12. Zener, C. 'Internal friction in solids: I. Theory of internal friction in reeds', *Physical Review*. **V52**, 1937.
13. Lifshitz, R., Roukes, M.L. 'Thermoelastic damping in micro- and nanomechanical systems', *Physical Review B*, **61**, 2000, pp 5600-5609.
14. Steeneken, P.G. et al. 'Parameter extraction and support-loss in MEMS resonators'. *Proceedings of COMSOL conference 2007*, Boston, USA, 2007.
15. Yang, J., Ono, T., M. Esashi, M. 'Energy dissipation in submicrometer thick single-crystal silicon cantilevers', *Journal of Microelectromechanical Systems*, **11** (6), 2002.
16. Weinberg, M. et al. 'Energy loss in MEMS resonators and the impact on inertial and RF devices', *Transducers 2009*, Denver, USA, June 21-25, 2009.
17. Yasumura, K.Y. et al. 'Quality factors in micron- and submicron-thick cantilevers', *Journal of microelectromechanical systems*, **9**(1), 2000, pp.117-125.
18. Roukes, M.L. 'Nanoelectromechanical systems', *Technical digest of the 2000 solid-state sensor and actuator workshop*, Hilton Head Isl., SC, June 4-8 2000.
19. Wang, Y. et al. 'Surface chemical control of mechanical energy losses in micromachined silicon structures', *Journal of physical chemistry B*, **107**, 2003, pp. 14270-14277.
20. Lobontiu, N. *Dynamics of microelectromechanical systems*. Springer, 2007.
21. Pandey, M. et al. 'Reducing anchor loss in MEMS resonators using mesa isolation', *Journal of microelectromechanical systems*, **18** (4), 2009, pp. 836-844.

Chapter 3

Fluid damping

The behaviour of the beam is now considered for the case of total immersion in an incompressible, homogeneous Newtonian fluid, of density ρ_f and dynamic viscosity μ , at constant temperature and pressure. Operating the resonator in a fluid environment introduces further damping mechanisms to the system. Deformation of a fluid by resonator motion is inherently dissipative due to fluid viscosity, whereas fluid inertia allows for the propagation of sound waves. Fluid behaviour can vary greatly, depending on the relative importance of viscous to inertial forces.

Newtonian fluids obey Newton's law of viscosity. These fluids have constant dynamic viscosity and density at constant temperature and pressure, regardless of shear rate. Dynamic viscosity is temperature dependent but independent of the pressure [1]. Non-Newtonian fluids however show variable viscosity at a constant temperature and pressure, dependent on the rate of shear [2].

Gases may be considered as incompressible viscous fluids when the maximum speed of the vibrating beam in the gas is much lower than the speed of sound in the gas. The Mach number, which is the ratio of the magnitude of the fluid velocity to the speed of sound in the fluid, is used to measure the tendency of a fluid to compress on interaction with a structure. Various authors have suggested that a fluid may reasonably be considered incompressible when the Mach number remains significantly less than 1, since compressibility should not then influence the analysis. Blevins [3] suggested an upper limit of 0.3, whereas Weiss et al [4] presented an upper limit of 0.01.

The governing equations for fluid behaviour are intrinsically nonlinear, and cannot be solved analytically for the beam in the fluid. Instead, an approximate solution is sought by using an established solution for a similar oscillating body.

The fluid damping mechanisms of primary concern in this work are viscous drag, added mass and molecular damping. The experimental devices, apparatus and

procedure are designed to avoid or minimise any pressure drag or squeeze-film damping. The damping mechanisms are discussed below.

3.1. Flow regimes

The fluid damping on a resonator is greatly affected by the pressure of the fluid. Depending on the ambient fluid pressure, fluid motion can range from continuum flow to molecular flow. To simplify the analysis of fluid damping, it is convenient to define pressure, or ‘flow’, regimes.

The appropriate approach to analysing the fluid field around a resonator depends upon the fluid flow regime. Flow regimes in gases, also referred to as pressure regimes, can be characterised by using the dimensionless Knudsen number Kn .

$Kn = \lambda/w$, where λ is the mean free path of a fluid gas molecule and w is the width of the gas layer in motion. λ is defined $\lambda = k_B T / \sqrt{2\pi p} d_g^2$ where k_B is the Boltzmann constant, T the temperature, p the gas pressure and d_g the diameter of the gas molecule. The parameter w can be taken as the beam width [5]. The flow regime then directs the analysis: for certain regimes continuum theory may be employed, while in other cases molecular theory may be required. Table 3.1 outlines flow regimes and the associated Knudsen numbers.

Flow regime	Kn range
Continuum	$Kn < 0.001$ [6,7]
	$Kn < 0.01$ [8,9]
Slip	$0.001 < Kn < 0.1$ [6, 7]
	$0.01 < Kn < 0.1$ [8, 9]
Viscous i.e. continuum plus slip	$Kn < 0.01$ [5]
	$Kn < 0.1$ [10]
Transition	$0.01 < Kn < 10$ [5]
	$0.1 < Kn < 10$ [6, 7, 8, 9, 10]
Free molecular	$Kn > 10$ [5, 6, 7, 8, 9, 10]

Table 3.1: Flow regimes

The boundaries between each regime are not easily defined. It can be seen from table 3.1 that although there seems to be consensus over the Knudsen values for the free molecular regime, there is disagreement over the continuum, slip and transition regimes.

3.1.1. Fluid damping in each flow regime

The fluid damping on a resonator has different mechanisms according to the pressure range in which the resonator is operated. Gas rarefaction reduces the viscous effect of the gas, such that the fluid damping varies from the highest value in the continuum regime to the lowest value in the free molecular regime [8]. Damping models vary according to the flow regime under consideration.

Viscous regime (continuum and slip)

In the viscous flow regime, which includes both the continuum and slip regimes, gas properties are mainly governed by molecule-molecule collisions [5], and the fluid may be considered a continuum. In this regime, an incompressible fluid is governed by the Navier-Stokes equation [7], and viscous flow models are used to

predict the damping. The contributions to the damping are discussed in detail in section 3.2, and models in section 3.3.

The continuum and slip regimes are differentiated by considering the conditions at the resonator surface. In the slip regime, the fluid velocity at the surface, with respect to the surface, is non-zero, and the Navier-Stokes equation starts to degenerate. The no-slip condition for viscous fluids states that at the surface, the fluid has zero velocity relative to the surface i.e. fluid velocity is equal to surface velocity. In the continuum regime, no-slip boundary conditions prevail [6,8].

Free molecular regime

In the free molecular regime, the fluid is considered a rarefied gas rather than a continuum. Damping occurs due to the molecular bombardment of an object by discrete, noninteracting gas particles. The viscous flow model is no longer valid and a free molecular model must be considered for the damping. Models similar to that proposed by Christian [11] are frequently used to estimate the damping on an isolated oscillator i.e. in the absence of any nearby structures. The momentum transfer between the oscillating body and the gas molecules is determined using the Maxwell-Boltzmann distribution function, from which the damping may then be calculated. An alternative approach by Bao et al [12] considers instead an energy transfer mechanism, and in doing so accounts for the presence of any neighbouring objects. A model based on momentum exchange considerations is presented in section 3.4.

Transition regime

In the transition flow regime, the mean free path of molecules is of the same order as the typical characteristic flow length. The collisions of the molecules with the surface of the body and intermolecular collisions are of similar importance and so analysis becomes very complicated [6,8]. In this regime, the Navier-Stokes equation and the Boltzmann equation start to lose validity [7].

There are generally two theoretical models used to explain behaviour in this regime: a molecular damping model as outlined above, or an ‘effective’ viscous damping model, used particularly in cases where squeeze-film damping is present [8,13,14]. With the latter, it is assumed that viscous damping is still dominant, but

with a modified ‘effective’ viscosity coefficient to account for rarefaction in the gas. Both approaches have their disadvantages: molecular damping models are only strictly valid at near vacuum pressures (for $Kn > 10$) [10], whereas the concept of effective viscosity is questionable at low pressures where it may be inappropriate to consider the fluid a viscous fluid [12].

3.2. Damping force in a continuum

The beam motion will induce an oscillating fluid force applied by the surrounding fluid to the beam, which acts as a damping force. Where device dimensions are such that the gap between the oscillating beam and the surrounding structure are small (i.e. $gap \ll L$), then this damping is dominated by squeeze-film damping [7,8,15]. Squeeze-film damping is caused by the squeezing of the fluid flow between a moving structure and fixed surroundings. When the beam moves towards the fixed surroundings, the pressure in the fluid between the two is increased, and the fluid is squeezed out from the edges of the beam. As the beam moves away, the situation reverses: the pressure drops between the beam and the surroundings, and fluid is sucked back into the space. The viscous drag of the fluid during the flow creates a damping force, opposing the motion – this is squeeze-film damping [15]. Where the gap between the oscillating beam and surrounding structure is large however, as is the case in this work, then fluid drag forces are the dominant loss mechanisms and squeeze-film effects may be considered negligible.

In the absence of squeeze-film damping, a rectangular beam oscillating in an otherwise stationary fluid continuum may then be considered to experience a fluid damping force composed of three parts [16]: one part due to the inertia of the accelerating outer flow; another due to the influence of viscous boundary layers; and a third due to the separation of these boundary layers leading to vortex shedding. These shall subsequently be referred to as the added mass, skin friction drag and pressure drag respectively.

3.2.1. Added mass

Acceleration of the beam causes the surrounding fluid to accelerate also. For convenience, this can be modelled as an entrained volume of fluid moving with the beam. The inertia of the entrained fluid is known as the added mass, and it acts with

the same sign, frequency and phase as the beam mass. Added mass acts to decrease the resonant frequency of the beam from the natural frequency measured in a vacuum. The effect of added mass becomes significant when fluid density is comparable to beam density.

3.2.2. Skin friction drag

Skin friction drag arises from the interaction between the fluid particles and the moving beam surface. The fluid exerts a shearing stress over the beam surface, opposing the motion. Across the surface of the beam, a boundary layer of low energy flow is generated, and it is this boundary layer which is responsible for the drag. The skin friction drag is the resultant, in the drag direction, of the shear stresses at the beam surface, and has a magnitude dependent upon the fluid viscosity.

3.2.3. Pressure drag

Pressure drag arises from differences of pressure over the surface of an oscillating body. Separation, where a fluid breaks free of a surface after being attached to it, can create a wake behind a moving body. In turn, the pressure acting on the front of the body may exceed that acting on the rear, resulting in a force opposing forward motion. Pressure drag depends on the shape of the body and is therefore also known as form drag.

The regime for attached flow depends on two dimensionless parameters: the Reynolds number (Re) and the Keulegan-Carpenter number (Kc). The Reynolds number gives the measure of the ratio of inertial forces to viscous forces, and is given by $Re = \rho_f D U_m / \mu$, where D is a characteristic length, and U_m the maximum velocity of the fluid free stream with respect to the surface. The Keulegan-Carpenter number describes the relative importance of drag forces over inertia forces for an oscillating body in a fluid otherwise at rest, and is defined $Kc = U_m T_o / D$, where T_o is the period of the oscillation.

For certain bodies, such as a circular cylinder, there is a regime at sufficiently small Kc where the fluid remains attached, regardless of Re [16]. For bodies with

sharp edges, such as a rectangular beam, separation will always occur to some extent at the sharp edges [16,17].

3.2.4. Resultant damping force

The resultant inline damping force can be represented by the following equation. For an oscillating body with velocity $U(t)$ in an otherwise stationary fluid, the inline damping force is:

$$F(t) = \rho_f C_a V \dot{U} + \frac{1}{2} \rho_f C_D A U |U| \quad (3.1)$$

where

- $F(t)$ is the total inline force on the object
- $U(t)$ is the velocity of the object relative to the fluid
- $\rho_f C_a V \dot{U}$ is the inertial force due to the added mass
- $\frac{1}{2} \rho_f C_D A U |U|$ is the total drag force, or ‘profile drag’ [18], which acts in phase with $U(t)$
- C_a is the added-mass coefficient
- V is the volume of the body
- C_D is the drag coefficient
- A is a reference area, e.g. the cross-sectional area of the body perpendicular to the flow direction

The inertia force acts in phase with the acceleration of the body, whereas the drag force acts in phase with the velocity. Viscous effects contribute to both of these forces [16]. The drag coefficient C_D accounts for both the skin friction drag and the pressure drag, allowing for the sum of the skin friction and pressure drag to be expressed as a single ‘profile’ drag. [17,18].

The profile drag is represented as a quadratic force. However, in the absence of separation, and therefore pressure drag, the drag coefficient C_D can be formulated

so as to reduce this to a linear viscous drag term i.e. the drag force becomes proportional to velocity.

For a general approximation, the Reynolds number can indicate which form the profile drag term may take:

- At very low Reynolds number, pressure drag may be neglected and the drag force may be considered proportional to velocity
- At high Re, there is flow separation and the drag force is nearly proportional to the square of the velocity
- At moderate Re, the drag force lies somewhere between the linear and quadratic forms [19].

For example, Douglas et al [18] suggest that for incompressible flow past a cylinder, pressure drag may be considered negligible where $Re < 0.5$, whereas separation may occur at higher levels of Re, e.g. $2 < Re < 30$. Shames [17] suggests that, for a cylinder, when $Re < 10$, then the drag is overwhelmingly due to skin friction.

Alternatively, considering the Keulegan-Carpenter number, the flow remains predominantly attached to a cylinder where $Kc < 0.1$ [20].

3.3. Viscous regime damping models

In the viscous flow regime, the flow of an incompressible fluid around an oscillating beam will be described by the Navier-Stokes equation. When the gravitational force on the fluid is neglected, this is expressed

$$\frac{\partial v}{\partial t} + (v \cdot \text{grad})v = -\frac{1}{\rho} \text{grad}p + \frac{\mu}{\rho} \Delta v \quad (3.2)$$

where v is the velocity of the fluid at a given point in space and time.

For oscillatory motion in an otherwise stationary fluid, the term $(v \cdot \text{grad})v$ may be neglected where one of the following conditions is met [1]:

- The viscous penetration depth $\delta \gg D$ and $Re \ll 1$.
- $D \gg \delta$ and the amplitude of oscillations are small compared to D .

where the viscous penetration depth $\delta = \sqrt{2\mu/\rho_f\omega}$, and ω is the circular frequency.

From the reduced equation, the flow distribution around a simple body (e.g. a sphere) can be determined, and consequently the fluid force acting on that body.

However, even if the Navier-Stokes equation is simplified by neglecting $(v.grad)v$, it still cannot be solved analytically for the rectangular beam in the fluid. Instead, an approximate solution is sought by using an established solution for a similar oscillating body. For a first approximation, modelling the beam as a string of spheres was considered, as this approach has been taken in several studies [21,22]. However, for greater consistency with the geometry of the beam, models based on circular and elliptic cylinders were favoured.

3.3.1. Circular cylinder model

To inform beam design, it is necessary to have an analytical approximation to the fluid damping in advance. For this purpose, the approach taken by Blevins [3] is considered, with rectangular beams being approximated as circular cylinders.

Added mass

The added mass coefficient for a circular cylinder in an oscillating flow of circular frequency ω is given by

$$C_a = 1 + 4(\pi\beta_D)^{-1/2} + (\pi\beta_D)^{-3/2} \quad (3.3)$$

where $\beta_D = \rho_f D^2 \omega / 2\pi\mu$ and D is the characteristic length (here, the diameter of the cylinder) [3]. It is assumed that the added mass coefficient for an oscillating cylinder in an otherwise still fluid is identical. The added mass per unit length for a cylinder, M_A , is then given by $M_A = C_a \rho_f \pi b^2 / 4$.

The added mass M_A for a rectangular beam under free vibration in a fluid has been specified using potential flow theory. It is given by $M_A = \alpha \rho_f \pi b^2 / 4$ where the coefficient α depends upon the width to depth ratio of the beam, b/d [23]. This is a factor of α greater than the similarly determined added mass for a circular cylinder.

Therefore, for the oscillating case, it is assumed that added mass may be approximated as $M_A = \alpha C_a \rho_f \pi b^2 / 4$. Values of α are presented in table 3.2.

b/d	α
0.1	2.23
0.2	1.98
0.5	1.70
1.0	1.51
2.0	1.36
5.0	1.21
10.0	1.14
∞	1.0

Table 3.2: coefficient α

Profile drag

For slightly viscous fluids at $Kc < 1$, so that there is no flow separation, the drag coefficient for a smooth circular cylinder is given by [3]:

$$C_D = Kc^{-1} \left[\frac{3}{2} \pi^3 (\pi \beta_D)^{-\frac{1}{2}} + \frac{3}{2} \pi^2 \beta_D^{-1} - \frac{3}{8} \pi^3 (\pi \beta_D)^{-\frac{3}{2}} \right] \quad (3.4)$$

Sarpkaya [24] explains that the above formula only strictly holds for $Kc \ll 1$, $Re.Kc \ll 1$, $\beta_D \gg 1$. Outside of this range, the drag coefficient must be determined experimentally.

The viscous drag force per unit length is then given by

$$F_D = \frac{1}{2} \rho_f |U_{rel}| U_{rel} D C_D = \frac{1}{2} \rho_f \left(\frac{dv}{dt} \right)^2 D C_D$$

This is a linear drag term. As Kuiper et al [20] point out, the inverse dependence of C_D on Kc compensates for expressing the linear drag through a quadratic

dependence on velocity. Letting $\alpha_D = \frac{1}{2} \rho_f \frac{D}{\mu} \frac{dv}{dt} C_D$ allows the drag force to be

$$\text{expressed } F_D = \alpha_D \mu \frac{dv}{dt}.$$

A rectangular beam will have a larger drag coefficient than a similarly sized circular cylinder [25]. Consequently, the beam drag is approximated by multiplying

the cylinder drag by a factor C (to be determined experimentally). Letting $\Phi = C\alpha_D$, the viscous drag force per unit length on a rectangular beam becomes $F_D = \Phi\mu \frac{dv}{dt}$. For the purpose of predicting approximate beam behaviour, it is simplest to use $C=1$. The characteristic length is taken to be the width of the beam b .

3.3.2. Elliptic cylinder model

The previously outlined circular cylinder model is only valid for Reynolds numbers and Keulegan-Carpenter numbers significantly smaller than 1. When it comes to operating the resonators in the nonlinear regime it is likely that Reynolds numbers will be encountered in the region of, or in excess of, 1. It is therefore necessary to look for a more appropriate damping model.

Zhang and Turner [26] proposed a linear fluid damping model based on experimental observations for MEMS cantilevers with rectangular cross-section shape. It seems reasonable to try extending this model to clamped-clamped beams of similar shape.

In this model the damping coefficient is given by

$$C_{damping} = \pi\mu(a + b\lambda) \quad (3.5)$$

where (a,b) is a cross-section shape dependent constant pair, and λ is a dimensionless parameter defined as the ratio of the width of cantilever to the penetration depth δ of the viscous fluid: $\lambda = width/\delta$. The drag force is then given as $F_D = C_{damping} \frac{dv}{dt}$. It should be noted that in this model, added mass is not considered.

Parameter a

Parameter a cannot be analytically derived for a rectangular beam [27]. However, by treating the beam as an elliptic cylinder it is possible to approximate using the following expression as derived by Oseen [28]:

$$a = \frac{4}{d_1 \sqrt{(d_1 + d_2)^{-\gamma} - \ln\left(\frac{\text{Re } d_1 + d_2}{16 d_2}\right)}} \quad (3.6)$$

Here γ is the Euler constant and Re is the Reynolds number. Equation (3.6) assumes steady flow, that the minor axis (d_1) is parallel to the velocity direction (see figure 3.1), and that the Reynolds number is smaller than 1. It has been shown that equation (3.6) offers a good approximation of parameter a with less than 10% relative error [27]. In the case of oscillatory motion, rather than steady flow, the Reynolds number is not uniform across the beam. It is therefore necessary to interpolate an average value of a to use in the approximation. For Reynolds number above 1, the approximation may no longer be valid, and it becomes necessary to experimentally fit a value of a .

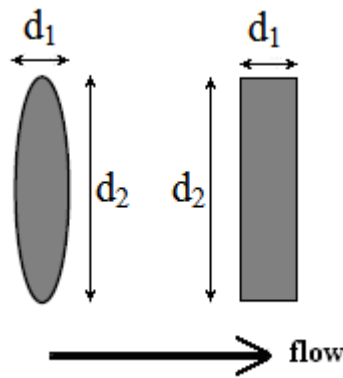


Figure 3.1: Comparison of elliptical cylinder to rectangular beam

Parameter b

Parameter b is determined by numerical analysis and comparison to experimental results [27]. Numerical simulations indicate that the thickness d_1 has negligible effect on the damping provided that the width to thickness ratio, d_2/d_1 , is greater than 5 [27]. Below this aspect ratio, the damping coefficient may not be as reliable since thickness effects become important.

3.4. Molecular and transition regimes damping model

In the absence of squeeze-film damping, a molecular damping model is assumed for both the molecular and transition flow regimes.

3.4.1. Molecular model

In the molecular regime at low pressure, the drag force due to gas molecules impinging on the beam can be represented by $F_D = \left(\frac{pbL}{v_T} \right) \frac{dv}{dt}$, where p is the pressure of the gas, $v_T = \sqrt{\frac{k_B T}{m_g}}$ is the thermal velocity of the gas molecules, m_g is the mass of a gas molecule, and $v(x,t)$ is the displacement of the beam element with respect to the inertial frame [29].

3.5. Equation of motion with fluid damping

The equation of motion for the free vibrations of the rectangular beam in fluid becomes

$$EI \frac{d^4 \bar{v}}{dx^4} + (\rho_s b d + M_A) \frac{d^2 v}{dt^2} + c_f \frac{dv}{dt} - Ebd \left[\eta + \frac{1}{2L} \int_0^L \left(\frac{d\bar{v}}{dx} \right)^2 dx \right] \frac{d^2 \bar{v}}{dx^2} = 0 \quad (3.7)$$

where c_f represents the appropriately selected fluid drag coefficient, according to the flow regime, intrinsic damping has been neglected, and v represents the displacement of a beam element with respect to the otherwise stationary fluid.

3.6. Summary

Models for the fluid damping on a rectangular beam, oscillating in fluids at various pressures, have been identified. The circular cylinder model facilitates the design of suitable resonators, whereas the elliptic cylinder model may be modified by use of subsequent experimental results. All of the models discussed may be incorporated into the beam equation of motion where appropriate.

3.7. References

1. Landau, L.D., Lifshitz, E.M. *Fluid mechanics*. Pergamon Press, 1959.
2. Ronaldson, K.A. et al. 'Transversely oscillating MEMS viscometer: The "Spider"', *International Journal of Thermophysics*, **27**(6), 2006, pp.1677-1695.
3. Blevins, R.D. *Flow-induced vibration*. 2nd ed. Van Nostrand Rheinhold, 1990.
4. Weiss, B., Reichel, E.K., Jakoby, B. 'Modeling of a clamped-clamped beam vibrating in a fluid for viscosity and density sensing regarding compressibility', *Sensors and Actuators A*, **143**, 2008, pp. 293-301.
5. Mertens, J. et al. 'Effects of temperature and pressure on microcantilever resonance response', *Ultramicroscopy*, **97**, 2003, pp. 119-126.
6. Hutcherson, S., Ye, W. 'On the squeeze-film damping of micro-resonators in the free-molecule regime', *Journal of Micromechanics and Microengineering*, **14**, 2004, pp. 1726-1733.
7. Young, J.Y.J., *Squeeze-film damping for MEMS structures*, MSc Thesis, Massachusetts Institute of Technology, 1998.
8. Pandey, A.K., Pratap, R., Chau, F.S. 'Effect of pressure on fluid damping in MEMS torsional resonators with flow ranging from continuum to molecular regime', *Experimental Mechanics*, **48**, 2008, pp. 91-106.
9. Nayfeh, A.H., Younis, M.I. 'A new approach to the modelling and simulation of flexible microstructures under the effect of squeeze-film damping', *Journal of Micromechanics and Microengineering*, **14**, 2004, pp. 170-181.
10. Bidkar, R.A. et al. 'Unified theory of gas damping of flexible microcantilevers at low ambient pressures', *Applied Physics Letters*, **94**, 2009, 163117.
11. Christian, R.G. 'The theory of oscillating-vane vacuum gauges', *Vacuum* **16** (4), 1966, pp. 175-178.
12. Bao, M. et al. 'Energy transfer model for squeeze-film air damping in low vacuum', *Journal of Micromechanics and Microengineering*, **12**, 2002, pp. 341-346.
13. Veijola, T. et al. 'Model for gas film damping in a silicon accelerator', *Transducers '97*, Chicago, USA, 1997.
14. Bao, M., Yang, H. 'Squeeze film air damping in MEMS', *Sensors and Actuators A*, **136**, 2007, pp. 3-27.
15. Senturia, S.D. *Microsystem design*. Springer, 2001.
16. Bearman, P.W. et al. 'Forces on cylinders in viscous oscillatory flow at low Keulegan-Carpenter numbers', *Journal of Fluid Mechanics*, **154**, 1985, pp. 337-356.
17. Shames, I. *Mechanics of fluids*. 3rd ed. Mcgraw-Hill, 1992.
18. Douglas, J.F., Gasiorek, J.M., Swaffield, J.A. *Fluid mechanics*. 3rd ed. Harlow: Longman, 1996.
19. Nayfeh, A.H., Mook, D.T. *Nonlinear oscillations*. Weinheim: Wiley-VCH, 2004.
20. Kuiper, G.L., Metrikine, A.V., Battjes, J.A. 'A new time-domain drag description and its influence on the dynamic behaviour of a cantilever pipe conveying fluid', *Journal of fluids and structures*, **23**, 2007, pp. 429-445.
21. Hosaka, H., Itao, K., Kuroda, S. 'Evaluation of energy dissipation mechanisms in vibrational microactuators', *IEEE Micro Electro Mechanical Systems Workshop, 25-28th January*. MEMS '94, Oiso, Japan, 1994.
22. Hirai, Y. et al. 'Resonance characteristics of micro cantilever in liquid', *Japanese Journal of Applied Physics*, **37**, 1998, pp. 7064-7069.

23. Blevins, R.D. *Formulas for natural frequency and mode shape*. Van Nostrand Rheinhold, 1979, pp. 386-392.
24. Sarpkaya, T. 'Force on a circular cylinder in viscous oscillatory flow at low Keulegan-Carpenter numbers', *Journal of Fluid Mechanics*, **165**, 1985, pp. 61-71.
25. Zhang, C., Xu, G., Jiang, Q. 'Analysis of the air-damping effect on a micromachined beam resonator', *Mathematics and Mechanics of Solids*, **8** (3), 2003, pp. 315-325.
26. Zhang, W., Turner, K.L. 'Pressure-dependent damping characteristics of micro silicon beam resonators for different resonant modes', *2005 IEEE Sensors*, **1 and 2**, 2005, pp. 357-260.
27. Zhang, W., Requa, M., Turner, K. 'Determination of frequency dependent fluid damping of micro and nano resonators for different cross-sections', *Nanotech 2006*, Boston, USA, 2006.
28. Lamb, H. *Hydrodynamics*. Cambridge, 1932.
29. Ekinici, K.L., Yang, Y.T., Roukes, M.L. 'Ultimate limits to inertial mass sensing based upon nanoelectromechanical systems', *Journal of applied physics*, **95**(5), 2004, pp. 2682-2689.

Chapter 4

Problem formulation and solution modelling

In this chapter the system is analysed by means of modal analysis and approximation methods. Following this analysis, numerical predictions are made in order to inform subsequent design and experimental work. For these predictions, the circular cylinder approximation to the damping model is utilised. Although constraints of this damping model are expected to be broken, it is the most appropriate of the damping models considered as it requires no experimental data in advance.

4.1. Harmonic displacement

In chapter 3 the equation of motion for an unforced beam in fluid was developed, and this equation presented in section 3.5. The inclusion of forcing on the beam, in the form of an applied harmonic displacement, is considered in this section.

Let the ends of the beam be displaced by an amount $\hat{v}(x,t)$ with respect to the inertial frame (see figure 4.1). Each infinitesimal beam element, and associated entrained fluid, is then also displaced by $\hat{v}(x,t)$. If both ends of the beam are displaced identically, then this reduces to $\hat{v}(t)$.



Figure 4.1: Harmonic displacement of resonator beam

Now let the total displacement of a beam element and entrained fluid, with respect to the inertial frame, be $v(x, t)$, where $v(x, t) = \bar{v}(x, t) + \hat{v}(x, t)$. The total displacement with respect to inertial frame is the sum of the applied displacement and that due to deformation. The equation of motion for the beam is thus:

$$EI \frac{d^4 \bar{v}}{dx^4} + (\rho_s bd + M_A) \frac{d^2 \bar{v}}{dt^2} + c \frac{d \bar{v}}{dt} - Ebd \left[\eta + \frac{1}{2L} \int_0^L \left(\frac{d \bar{v}}{dx} \right)^2 dx \right] \frac{d^2 \bar{v}}{dx^2} = 0$$

where c represents the appropriately selected drag coefficient for the rectangular beam. This coefficient is assumed to account for all viscous damping on the body, including any intrinsic damping. This approach is justified on the grounds that intrinsic damping cannot be known with great accuracy (see section 2.5), the fluid damping coefficient is expected to dominate over the intrinsic damping coefficient in the continuum flow regime (confirmed in sections 8.3.1 and 8.3.2), and at the centre of the beam where velocity, and hence viscous damping, is greatest, so $v \approx \bar{v}$ for nonlinear vibrations (see section 7.1.4).

Note that the viscous damping on the body is dependent on the velocity of body with respect to the fluid. The fluid is assumed to be at rest with respect to the inertial frame.

For a harmonic displacement of $\hat{v} = h \sin \omega t$ applied at both ends (i.e. at $x=0, L$), where h is the displacement amplitude, the equation of motion then becomes

$$EI \frac{d^4 \bar{v}}{dx^4} + (\rho_s bd + M_A) \frac{d^2 \bar{v}}{dt^2} + c \frac{d \bar{v}}{dt} - Ebd \left[\eta + \frac{1}{2L} \int_0^L \left(\frac{d \bar{v}}{dx} \right)^2 dx \right] \frac{d^2 \bar{v}}{dx^2} = (\rho_s bd + M_A) \omega^2 h \sin \omega t - c \omega h \cos \omega t \quad (4.1)$$

4.2. Modal analysis

A weakly damped, weakly nonlinear system can be analysed by employing modal discretisation to obtain a reduced-order model of the system [1]. Such a reduced-order model should encapsulate most of the properties of the complete system.

The approach is to expand the system response in terms of the undamped, unforced linear mode shapes, and to introduce this expansion into the equation of motion. The effect is to replace the partial differential equation with a set of coupled ordinary differential equations. Subsequent approximation of the system response can then be achieved by selecting an appropriate number of modes to include in the expansion. It is essential though that neglected modes do not significantly affect the system response.

4.2.1. Analysis of fundamental mode

A solution to equation (4.1) can be sought by using the modal expansion $\bar{v} = \sum T(t)X(x)$, where $T(t)$ represents the temporal functions and $X(x)$ spatial functions. This general solution consists of an infinite number of modes.

The resonator will be operated at close to its fundamental mode of vibration. As Bishop and Johnson [2] noted, where the higher modes have much higher frequencies than this fundamental mode, so these higher modes may be neglected. The forced motion will be almost entirely in the fundamental mode. Where damping is present, those modes that are not directly or indirectly excited will decay with time [3]. It is therefore reasonable to consider only the fundamental mode shape $\bar{v} = T(t)X(x)$.

In the absence of damping, external displacement and midplane stretching, equation (4.1) then reduces to $EI \frac{d^4 \bar{v}}{dx^4} + \rho b d \frac{d^2 \bar{v}}{dt^2} = 0$. Inserting the fundamental mode yields $\frac{1}{X} \frac{d^4 X}{dx^4} = -\frac{\rho A}{TEI} \frac{d^2 T}{dt^2} = k_r^4$, where k_r^4 is a constant. The general solution for the spatial component is then given by

$$X = C_1 \cos k_r x + C_2 \sin k_r x + C_3 \cosh k_r x + C_4 \sinh k_r x \quad (4.2)$$

The boundary conditions on the clamped-clamped beam are as follows:

$$\begin{aligned} \bar{v}_{x=0} &= 0 & \bar{v}_{x=L} &= 0 \\ \left(\frac{d\bar{v}}{dx} \right)_{x=0} &= 0 & \left(\frac{d\bar{v}}{dx} \right)_{x=L} &= 0 \end{aligned}$$

Applying the boundary conditions gives $C_1=C_3=0$, and the following relation:

$$\begin{bmatrix} (\cos k_r L - \cosh k_r L) & (\sin k_r L - \sinh k_r L) \\ (-\sin k_r L - \sinh k_r L) & (\cos k_r L - \cosh k_r L) \end{bmatrix} \begin{bmatrix} C_2 \\ C_4 \end{bmatrix} = 0$$

For non-trivial solutions, the determinant of the first matrix must be zero, yielding $\cos k_r L \cosh k_r L = 1$. This has eigenvalues as shown in table 4.1:

Solution	Value
$k_0 L$	0
$k_1 L$	4.730041
$k_2 L$	7.853205
$k_3 L$	10.995608

Table 4.1: First four eigenvalues for mode shape

This approach predicts an infinite number of modes of vibration, with each mode having its own particular shape and natural frequency. The first non-trivial solution, i.e. the fundamental mode, occurs where $kL \approx 4.730041$. This corresponds to the solution $X = -1.0177(\cos kx - \cosh kx) + (\sin kx - \sinh kx)$. Figure 4.2 shows an illustrative plot of this fundamental mode shape.

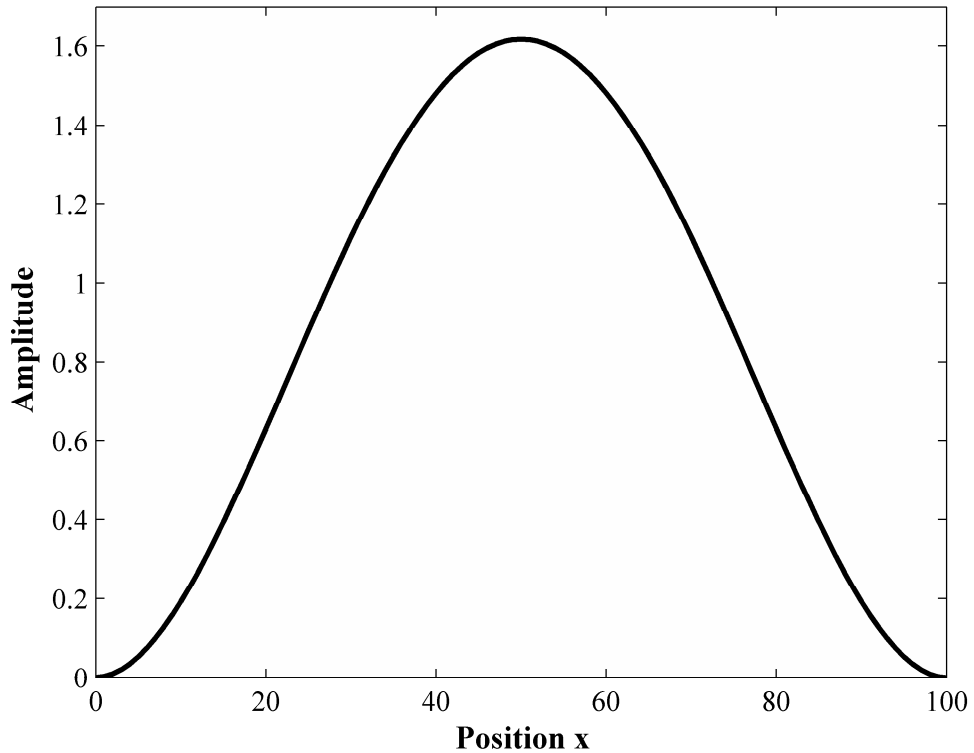


Figure 4.2: Fundamental mode shape

This fundamental mode is now inserted into equation (4.1):

$$EIT \frac{d^4 X}{dx^4} + (\rho_s bd + M_A) X \frac{d^2 T}{dt^2} + cX \frac{dT}{dt} - EbdT \left[\eta + \frac{T^2}{2L} \int_0^L \left(\frac{dX}{dx} \right)^2 dx \right] \frac{d^2 X}{dx^2}$$

$$= (\rho_s bd + M_A) \omega^2 h \sin \omega t - c \omega h \cos \omega t$$

Multiplying the equation through by the mode shape, and integrating from 0 to L gives

$$EIT \int_0^L X \frac{d^4 X}{dx^4} dx + c \frac{dT}{dt} \int_0^L XX dx + (\rho_s bd + M_A) \frac{d^2 T}{dt^2} \int_0^L XX dx$$

$$- EbdT \left[\eta + \frac{T^2}{2L} \int_0^L \left(\frac{dX}{dx} \right)^2 dx \right] \int_0^L X \frac{d^2 X}{dx^2} dx = \int_0^L X [(\rho_s bd + M_A) \omega^2 h \sin \omega t - c \omega h \cos \omega t] dx$$

Now employ the following substitutions and relations:

$\xi = x/L$
$\beta = kL$
$F_p = \int_0^1 X d\xi$
$F_1 = LF_p (\rho_s bd + M_A) \omega^2 h$
$F_2 = -LF_p c \omega h$
$\gamma = \int_0^1 X^2 d\xi$
$\varphi_1 = \int_0^1 \left(\frac{dX}{d\xi} \right)^2 d\xi$
$\varphi_2 = \int_0^1 X \frac{d^2 X}{d\xi^2} d\xi$
$\frac{d^4 X}{dx^4} = k^4 X$

Table 4.2: substitutions and relations

Thus

$$(\rho_s bd + M_A) L \gamma \ddot{T} + c L \dot{T} \gamma + \left(\frac{EI \beta^4 \gamma}{L^3} - \frac{Ebd \eta \varphi_2}{L} \right) T - \frac{Ebd \varphi_1 \varphi_2}{2L^3} T^3$$

$$= F_1 \sin \omega t + F_2 \cos \omega t \quad (4.3)$$

In order to evaluate the integrals, Matlab software was employed. The quad function was used to numerically evaluate the integrals using recursive adaptive Simpson quadrature. The numerical values are given in table 4.3.

Parameter	Value
γ	1.0344 ¹
φ_1	12.7473
φ_2	-12.7473
F_p	0.8455

Table 4.3: Integral values

It can now be observed that the undamped natural frequency (in Hz) for the fundamental mode is given by $\omega_0 = \frac{1}{2\pi} \sqrt{\frac{Ed^2\beta^4}{12\rho_s L^4}}$, where ρ_s is the density of the beam and η is assumed to be zero. This allows for the evaluation of ω_0 for the first mode for a range of dimensions. This is of interest as the resonator response will be measured near this natural frequency.

Consider the following proposed beams:

Material	Density ρ_s (kg.m^{-3})	Young's modulus E ($\text{kg.m}^{-1}.\text{s}^{-2}$)	Beam	Length L (μm)	Width b (μm)	Depth d (μm)
Silicon 100	2329	169E+9	A	1200	30	15
Silicon 100	2329	169E+9	B	1500	75	15

Table 4.4: Proposed silicon beams

The first two natural frequencies for each beam are shown in table 4.5. It is apparent that the second modes are at considerably higher frequencies than the fundamental modes. This suggests that the higher modes may then be neglected when exciting the fundamental mode only.

β	Natural frequency (Hz)	
	Beam A	Beam B
4.730041	91,211	58,375
7.853205	251,426	160,913

Table 4.5: Natural frequencies for first two modes

¹ Note here that the true value for γ is actually 1 [2, p.323], and is subsequently adopted.

Equation (4.3) can be reformulated with nondimensional parameters, by making the following substitutions:

$\tau = \sqrt{\frac{\left(\frac{EI\beta^4\gamma}{L^3} - \frac{Ebd\eta\phi_2}{L}\right)}{(\rho_s bd + M_A)L\gamma}} t$
$r = \omega \sqrt{\frac{(\rho_s bd + M_A)L\gamma}{\left(\frac{EI\beta^4\gamma}{L^3} - \frac{Ebd\eta\phi_2}{L}\right)}}$
$2\zeta = \frac{cL\gamma}{\sqrt{(\rho_s bd + M_A)L\gamma \left(\frac{EI\beta^4\gamma}{L^3} - \frac{Ebd\eta\phi_2}{L}\right)}}$
$\lambda = \frac{-\frac{Ebd\phi_1\phi_2}{2L^3}}{\left(\frac{EI\beta^4\gamma}{L^3} - \frac{Ebd\eta\phi_2}{L}\right)}$
$K_1 = \frac{F_1}{\left(\frac{EI\beta^4\gamma}{L^3} - \frac{Ebd\eta\phi_2}{L}\right)}$
$K_2 = \frac{F_2}{\left(\frac{EI\beta^4\gamma}{L^3} - \frac{Ebd\eta\phi_2}{L}\right)}$

Table 4.6: Nondimensional parameters

This gives

$$\frac{d^2T}{d\tau^2} + 2\zeta \frac{dT}{d\tau} + T + \lambda T^3 = K_1 \sin r\tau + K_2 \cos r\tau \quad (4.4)$$

This equation is in the form of the damped Duffing equation. The equation can have 1, 2 or 3 real solutions, depending on system coefficients. In the latter case, the solutions exhibit two distinct jump points [4]. These singularities are separated by a frequency difference δF , as illustrated in figure 4.3. Note that the model predicts $\lambda > 0$, which corresponds to a hardening spring i.e. the stiffness increases as a function of displacement, as a result of the mechanical restoring force from midplane stretching.

Figure 4.3 shows the known frequency response of equation (4.4) for four different levels of forcing, where $P^2 = K_1^2 + K_2^2$. At the lowest forcing P1, the frequency

response of the beam is linear. The second level of forcing P2 is close to critical forcing at which jump phenomena appear. Forcing P3 is at a sufficient level to bring on nonlinear behaviour, and clear jump phenomena can be observed. If the frequency is increased from A, then a bistable region is reached at point U_1 , which shall be referred to as the upper jump point. Here, the amplitude drops to U_2 , before following the path towards B. Conversely, on decreasing frequency from B, the amplitude makes a jump from the lower jump point L_1 up to L_2 , then follows the path towards A. At higher forcing again, P4, the resonance peak is further deflected, plus the bistable region is wider [5].

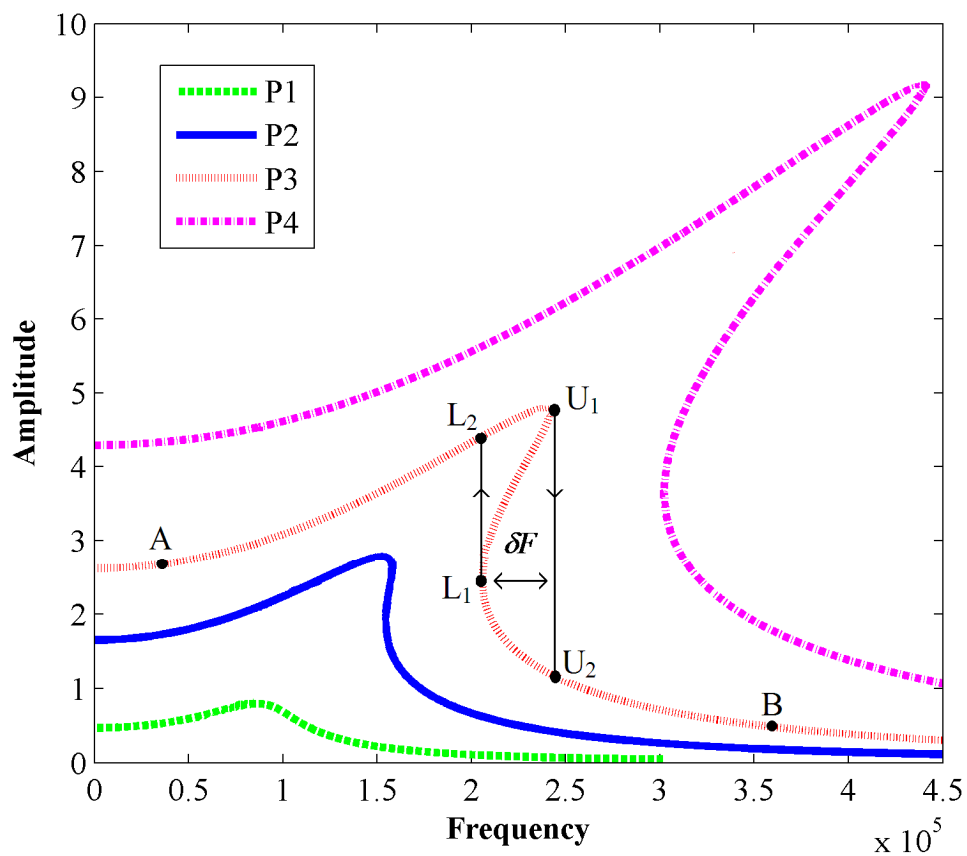


Figure 4.3: Plot of frequency versus amplitude for a generic damped Duffing equation – hardening spring

4.3. Quantitative analysis

It is required now to analyse equation (4.4) formally to confirm that it matches predicted behaviour. Commonly applied methods for approximately solving nonlinear systems will be used. First, the harmonic balance method is used to predict the frequency response of the system. Later, the stability of the system is examined by using the Krylov-Bogoliubov averaging method. Such methods are restricted to weakly nonlinear systems [6] so it is necessary here to establish whether this is true of the system.

To evaluate the strength of the nonlinearity, it is necessary to fully nondimensionalise the problem, to allow comparison of the sizes of terms in equation (4.4). Take h , the displacement amplitude (subsequently referred to as the background displacement amplitude), as a characteristic length such that $T = h\hat{T}$. Substituting into equation (4.4) then yields

$$\left(\frac{d^2\hat{T}}{d\tau^2}\right) + 2\zeta\left(\frac{1}{\omega_a}\frac{d\hat{T}}{d\tau}\right) + \left(\frac{1}{\omega_a^2}\hat{T}\right) + \frac{h^2\lambda}{\omega_a^2}(\hat{T})^3 = \frac{K_1}{h\omega_a^2}\sin r\tau + \frac{K_2}{h\omega_a^2}\cos r\tau$$

$$\text{where } \omega_a = \sqrt{\frac{\left(\frac{EI\beta^4\gamma}{L^3} - \frac{Ebd\eta\phi_2}{L}\right)}{(\rho_s bd + M_A)L\gamma}}$$

The nonlinear coefficient is then $\frac{h^2\lambda}{\omega_a^2}$. The ratio of this coefficient to the linear displacement coefficient is $h^2\lambda = h^2\left(\frac{-6\phi_1\phi_2}{d^2\beta^4\gamma}\right) \approx 1.95\frac{h^2}{d^2}$. Therefore there is a weak nonlinearity in cases where $d \gg h$. Making the assumption that a ratio of 0.01 or less guarantees a weak nonlinearity, then it is approximately required that $d \geq 14h$. This is assumed to be the case, and is confirmed at the beginning of chapter 7.

4.3.1. Harmonic balance solution

With the method of harmonic balance, a periodic solution is assumed in the form of a harmonic series. Upon substitution and matching (balancing) of harmonic terms, a set of coupled equations is obtained. In general, it is sufficient to consider the first few harmonics only, as they tend to dominate typical periodic behaviour. It should be noted though that neglected higher terms may be important in improving the accuracy of the solution [7].

Let a solution to equation (4.4) be expressed in the form

$$T(\tau) = \sum_{p=1}^{\infty} A_p \frac{e^{ip\tau}}{2} + \sum_{p=1}^{\infty} A_p^* \frac{e^{-ip\tau}}{2}$$

Inputting this series solution to equation (4.4) and matching where $p=r$ yields

$$\begin{aligned} & -r^2 A_r \frac{e^{ir\tau}}{2} - r^2 A_r^* \frac{e^{-ir\tau}}{2} + 2i\zeta \left\{ r A_r \frac{e^{ir\tau}}{2} - r A_r^* \frac{e^{-ir\tau}}{2} \right\} + A_r \frac{e^{ir\tau}}{2} + A_r^* \frac{e^{-ir\tau}}{2} \\ & + \lambda \left\{ A_r^3 \frac{e^{i3r\tau}}{8} + A_r^*{}^3 \frac{e^{-i3r\tau}}{8} + 3A_r^2 \frac{e^{ir\tau}}{8} A_r^* + 3A_r \frac{e^{-ir\tau}}{8} A_r^*{}^2 \right\} \\ & = K_1 \left[-\frac{i}{2} (e^{ir\tau} - e^{-ir\tau}) \right] + K_2 \left[\frac{1}{2} (e^{ir\tau} + e^{-ir\tau}) \right] \end{aligned}$$

Harmonic terms are then collected and equated. Choosing only to consider terms of the order $e^{ir\tau}$ yields $(1 - r^2)A_r + 2i\zeta r A_r + \frac{3}{4}\lambda A_r^2 A_r^* = -iK_1 + K_2$

Letting $A_r = a_r e^{i\phi_r}$ results in

$$\begin{aligned} & a_r (1 - r^2) (\cos \phi_r + i \sin \phi_r) + 2i\zeta r a_r (\cos \phi_r + i \sin \phi_r) + \frac{3}{4} \lambda a_r^3 (\cos \phi_r + i \sin \phi_r) \\ & = -iK_1 + K_2 \end{aligned}$$

Taking the real and imaginary parts of the equation, squaring and adding, yields

$$\left[a_r (1 - r^2) + \frac{3}{4} \lambda a_r^3 \right]^2 + (2\zeta r a_r)^2 = K_1^2 + K_2^2 \quad (4.5)$$

This is a frequency-response relationship which can subsequently be used to approximate the behaviour of the system.

The phase ϕ_r is similarly determined to be given by the formula

$$\tan \phi_r = \frac{-K_1 \left[a_r (1-r^2) + \frac{3}{4} \lambda a_r^3 \right] - 2\zeta r a_r K_2}{K_2 \left[a_r (1-r^2) + \frac{3}{4} \lambda a_r^3 \right] - 2\zeta r a_r K_1} \quad (4.6)$$

In addition to harmonic oscillations, a nonlinear system will exhibit subharmonic and superharmonic oscillations [4]. With a forcing frequency of ω , and for $N=2,3,4,\dots$, subharmonic oscillations occur at frequencies $\omega_N = \frac{\omega}{N}$, whereas superharmonic oscillations are at frequencies $\omega_N = N\omega$. For the system under consideration, of significance would be superharmonic resonance at $\omega \approx \frac{\omega_0}{3}$, or subharmonic resonance at $\omega \approx 3\omega_0$ [6]. However, operation will occur at close to the fundamental frequency. Therefore superharmonics and subharmonics are not considered further in this work.

4.3.2. Frequency response

The frequency-response relationship given in equation (4.5) was used to plot the behaviour of beams A and B in argon, with the background displacement amplitude h fixed at 5nm. This was achieved using Matlab software, employing the **roots** function to solve the polynomial, and plotting the real solutions. Figure 4.4 shows this plot and illustrates the occurrence of jump points in the vicinity of the fundamental natural frequencies.

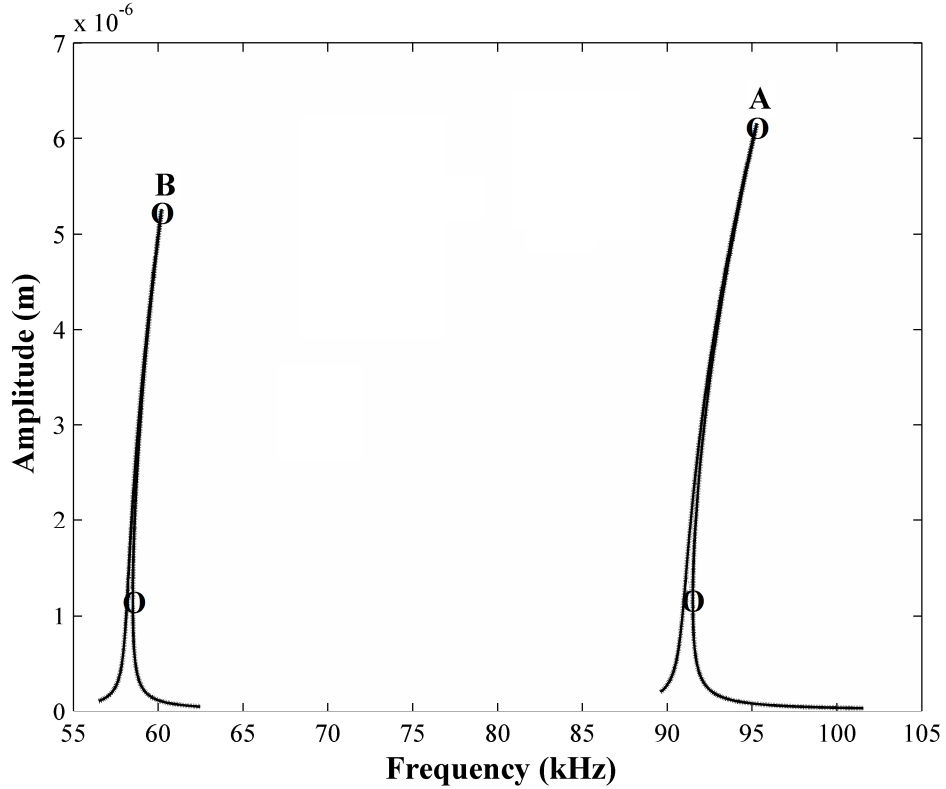


Figure 4.4: Predicted frequency response for beams A and B in argon, with an external displacement $h=5\text{nm}$. Jump points indicated by O

4.4. Stability

The discussion so far has predicted the occurrence of a bistable region when forcing is above some critical value. In the following sub-sections this is examined further in order to confirm these predictions.

4.4.1. Jump points and peak response

Examine equation (4.5). For convenience let $P^2 = K_1^2 + K_2^2$, then expanding gives

$$(1 - r^2)^2 a_r^2 + \frac{9}{16} \lambda^2 a_r^6 + (1 - r^2) \frac{3}{2} \lambda a_r^4 + 4\zeta^2 r^2 a_r^2 = P^2 \quad (4.7)$$

From figure 4.3 it is apparent that jump points occur where $\frac{d\omega}{da} = 0$, and the peak response where $\frac{da}{d\omega} = 0$.

Considering the jump points first, differentiate (4.7) with respect to a , and equate $\frac{d\omega}{da}$ to zero. Note first that $r = \frac{\omega}{\omega_a}$, so $\frac{d\omega}{da} = \frac{d(r\omega_a)}{da} = \omega_a \frac{dr}{da} + r \frac{d\omega_a}{da}$. In the case that M_A is negligible, then $\frac{d\omega_a}{da} \approx 0$ and $\omega_a \approx \omega_0$. This assumption is made here, and its validity confirmed in section 4.5.1. With this approximation then, $\frac{d\omega}{da} = \omega_0 \frac{dr}{da}$, meaning that to set $\frac{d\omega}{da}$ to zero simply requires $\frac{dr}{da} = 0$.

Differentiating as indicated results in the following formula from which the jump points can be determined:

$$0 = 4r^2 \zeta^2 + \left(1 - r^2 + \frac{9}{4} \lambda a_r^2\right) \left(1 - r^2 + \frac{3}{4} \lambda a_r^2\right) \quad (4.8)$$

To predict the position of the peak response, follow a similar procedure, except differentiating (4.7) with respect to r and equating $\frac{da}{dr}$ to zero. This results in the formula $r^2 = 1 + \frac{3}{4} \lambda a^2 - 2\zeta^2$. (4.9)

This can be rewritten $\omega^2 = \omega_a^2 \left(1 + \frac{3}{4} \lambda a^2 - 2\zeta^2\right)$, and indicates that the peak response frequency depends on the magnitude and sign of the nonlinearity, as well as the damping and displacement. It is apparent that in the linear case, at $\lambda=0$, the peak occurs at $\omega = \omega_a \sqrt{(1 - 2\zeta^2)}$, indicating that damping reduces the peak frequency, as expected.

4.4.2. Stability condition

To this point it has been stated that, given sufficient forcing, a bistable region will occur. To confirm this, the Krylov-Bogoliubov averaging method of slowly changing phase and amplitude may be employed. This is a perturbation method which looks to obtain the response of the nonlinear system by perturbing the response of the corresponding linearised system. It should be noted that the accuracy of such perturbation solutions typically decreases as amplitudes of motion increase [6].

Consider a linearised version of equation (4.4) with $\lambda = 0$. This could be investigated by using a solution of the form $T = a_0 \sin(r\tau + \psi_0)$. It is assumed that the nonlinear solution is similar to the linear one, except with amplitude and phase allowed to vary with time. Consequently take

$$T = a(\tau)\sin(r\tau + \psi(\tau)) \quad (4.10)$$

There are now three unknowns: T , $a(\tau)$ and $\psi(\tau)$. A third equation is needed, in addition to (4.4) and (4.10), in order ensure uniqueness of the transformation. For this purpose the condition is posed that the velocity has a similar functional form to that of the linear case. The subsequent transformation, known as a Van der Pol transformation [6], then states the requirement that

$$\dot{T} = ar \cos(r\tau + \psi) \quad (4.11)$$

Equations (4.4), (4.10) and (4.11) yield

$$\begin{aligned} \dot{a} = & \left\{ \frac{K_1}{r} \sin(r\tau) + \frac{K_2}{r} \cos(r\tau) \right\} \cos(r\tau + \psi) - \frac{a(1-r^2)}{r} \sin(r\tau + \psi) \cos(r\tau + \psi) \\ & - 2\zeta a \cos^2(r\tau + \psi) - \frac{\lambda}{r} a^3 \sin^3(r\tau + \psi) \cos(r\tau + \psi) \end{aligned} \quad (4.12)$$

$$\begin{aligned} \dot{\psi} = & -\frac{K_1}{r} \frac{\sin(r\tau + \psi)}{a} \sin r\tau - \frac{K_2}{r} \frac{\sin(r\tau + \psi)}{a} \cos r\tau \\ & + \frac{(1-r^2)}{r} \sin^2(r\tau + \psi) + 2\zeta \sin(r\tau + \psi) \cos(r\tau + \psi) + \frac{\lambda}{r} a^2 \sin^4(r\tau + \psi) \end{aligned}$$

Now it is necessary to introduce the approximation involved in Krylov-Bogoliubov averaging. \dot{a} and $\dot{\psi}$ are taken to be small quantities, such that a and ψ change very little during one period of oscillation. It is then possible to replace the equations for \dot{a} and $\dot{\psi}$ with their average values over one period. This gives

$$\begin{aligned}\dot{a} &\approx \bar{\dot{a}} = \frac{r}{2\pi} \int_0^{2\pi/r} \dot{a}(\tau) d\tau \\ &= -\left[\frac{K_1}{2r}\right] \sin(\psi) + \left[\frac{K_2}{2r}\right] \cos(\psi) - \zeta a \\ \dot{\psi} &\approx \bar{\dot{\psi}} = \frac{r}{2\pi} \int_0^{2\pi/r} \dot{\psi}(\tau) d\tau \\ &= -\left[\frac{K_1}{2ra}\right] \cos(\psi) - \left[\frac{K_2}{2ra}\right] \sin(\psi) - \frac{1}{2r}(r^2 - 1) + \frac{3}{8} \frac{\lambda}{r} a^2\end{aligned}\tag{4.13}$$

At stationary points, $\dot{a} = \dot{\psi} = 0$, so

$$\begin{aligned}\dot{a} = 0 &= -\left[\frac{K_1}{2r}\right] \sin \varphi_s + \left[\frac{K_2}{2r}\right] \cos \varphi_s - \zeta C \\ \dot{\psi} = 0 &= -\left[\frac{K_1}{2rC}\right] \cos \varphi_s - \left[\frac{K_2}{2rC}\right] \sin \varphi_s - \frac{1}{2r}(r^2 - 1) + \frac{3}{8} \frac{\lambda}{r} C^2\end{aligned}$$

which together yield

$$\begin{aligned}\sin \varphi_s &= \left[\frac{K_2}{K_1^2 + K_2^2}\right] \left[-C(r^2 - 1) + \frac{6}{8} \lambda C^3 \right] - \left[\frac{K_1}{K_1^2 + K_2^2}\right] 2r\zeta C \\ \cos \varphi_s &= \left[\frac{K_2}{K_1^2 + K_2^2}\right] 2r\zeta C + \left[\frac{K_1}{K_1^2 + K_2^2}\right] \left[-C(r^2 - 1) + \frac{6}{8} \lambda C^3 \right]\end{aligned}$$

Now consider small perturbations such that $a = C + a'$, $\varphi = \varphi_s + \varphi'$. This gives

$$\begin{aligned}\dot{a}' &= -\left[\frac{K_1}{2r}\right] \sin(\varphi_s + \varphi') + \left[\frac{K_2}{2r}\right] \cos(\varphi_s + \varphi') - \zeta(C + a') \\ \dot{\psi}' &= -\left[\frac{K_1}{2ra}\right] \cos(\varphi_s + \varphi') - \left[\frac{K_2}{2ra}\right] \sin(\varphi_s + \varphi') - \frac{1}{2r}(r^2 - 1) + \frac{3}{8} \frac{\lambda}{r} (C + a')^2\end{aligned}$$

Using trigonometric identities, and linearising for small φ' :

$$\dot{a}' = -\left[\frac{K_1}{2r}\right]\left[\sin \varphi_s + \varphi' \cos \varphi_s\right] + \left[\frac{K_2}{2r}\right]\left[\cos \varphi_s - \varphi' \sin \varphi_s\right] - \zeta(C + a')$$

$$\dot{\varphi}' = -\left[\frac{K_1}{2ra}\right]\left[\cos \varphi_s - \varphi' \sin \varphi_s\right] - \left[\frac{K_2}{2ra}\right]\left[\sin \varphi_s + \varphi' \cos \varphi_s\right] - \frac{1}{2r}(r^2 - 1) + \frac{3}{8} \frac{\lambda}{r}(C + a')^2$$

Substituting and then linearising by ignoring a'^2 and a'^3 terms:

$$\dot{a}' = -\zeta a' + \frac{C}{2r} \left(r^2 - 1 - \frac{3}{4} \lambda C^2 \right) \varphi'$$

$$\dot{\varphi}' = \frac{1}{2r(C + a')} \left(1 - r^2 + \frac{9}{4} \lambda C^2 \right) a' - \frac{1}{2r(C + a')} 2rC\zeta\varphi'$$
(4.14)

Linearising again by letting $(C + a') = C$ (since $C \gg a'$):

$$\dot{\varphi}' = \frac{1}{2rC} \left(1 - r^2 + \frac{9}{4} \lambda C^2 \right) a' - \zeta \varphi'$$
(4.15)

Take $a' = e_1 e^{\phi t}$, $\varphi' = e_2 e^{\phi t}$ and look for the characteristic equation. Inserting these values into (4.14) and (4.15) and combining yields

$$\phi^2 + 2\phi\zeta + \frac{1}{4r^2} \left[4r^2\zeta^2 + \left(1 - r^2 + \frac{9}{4} \lambda C^2 \right) \left(1 - r^2 + \frac{3}{4} \lambda C^2 \right) \right] = 0$$

It is required for stability that the real part of ϕ is zero or negative i.e. the perturbations do not grow. By defining a stability parameter S as

$$S = 4r^2\zeta^2 + \left(1 - r^2 + \frac{9}{4} \lambda C^2 \right) \left(1 - r^2 + \frac{3}{4} \lambda C^2 \right)$$
(4.16)

then it is found that $\phi = -\zeta \pm \sqrt{\zeta^2 - \frac{1}{4r^2} S}$.

Consider three conditions as follows:

S=0:

In this case $0 = 4r^2\zeta^2 + \left(1 - r^2 + \frac{9}{4}\lambda C^2\right)\left(1 - r^2 + \frac{3}{4}\lambda C^2\right)$, which is identical to equation (4.8) which defines the jump points. ϕ is zero and such solutions are said to be neutrally stable.

S>0:

ϕ is negative and these solutions are asymptotically stable

S<0:

One of the real values of ϕ is greater than zero and so these solutions are unstable.

For accuracy, it is stated then that solutions are stable for $t > 0, S \geq 0$. The regions as identified above are illustrated in figure 4.5.

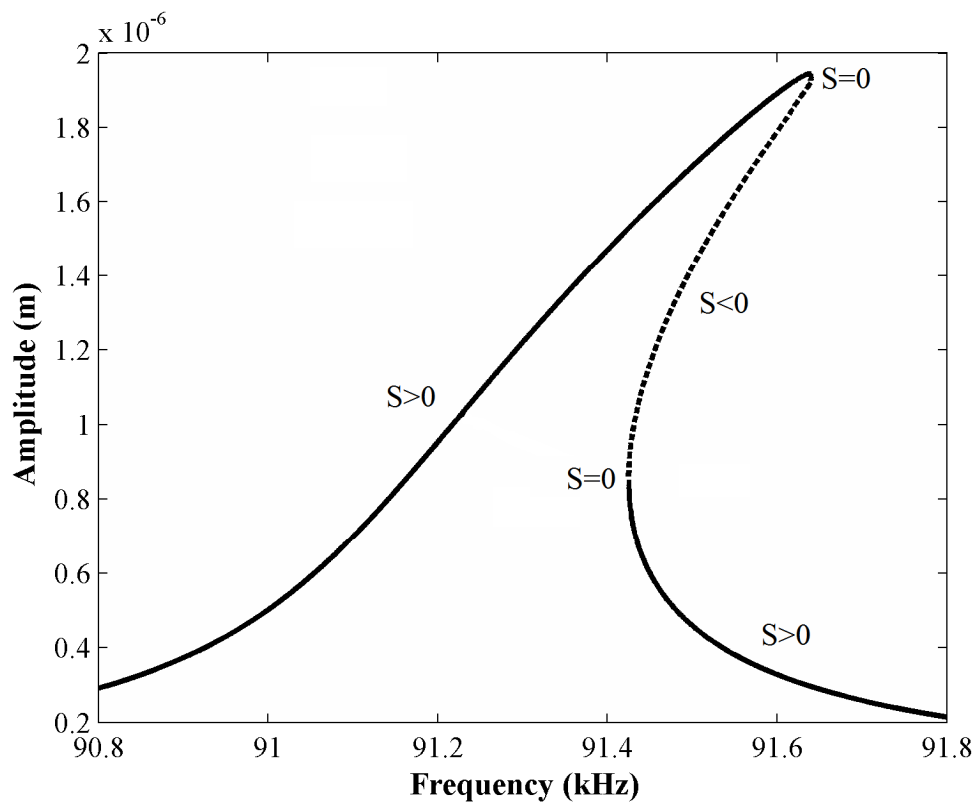


Figure 4.5: Stability condition

Using the above analysis it is possible to predict the region in the amplitude-frequency domain where instabilities will occur. Figure 4.6 shows this prediction for beam B in air. The solid line represents the locus of points where $S=0$, i.e. the locus of jump points. The dashed lines represent the bistable region for the particular given forcing level.

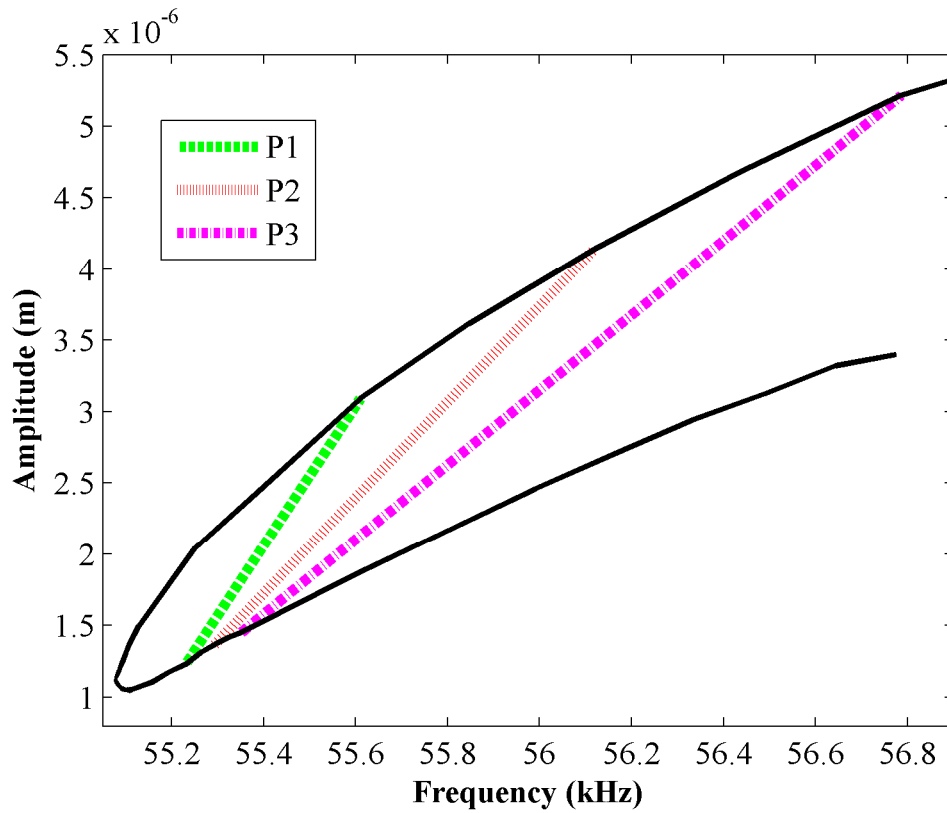


Figure 4.6: Unstable regions for beam B in air

4.5. Numerical predictions

This section employs the circular cylinder model of damping in order to make predictions about beam behaviour in fluids at atmospheric pressure. The relevant properties of the chosen fluids can be found in Appendix A. The damping model constraints, regarding size of Reynolds number and/or the Keulegan-Carpenter number, are seen to be broken; however, the degree to which the constraints are broken suggests that this approach may still offer a useful indication of real system behaviour.

Unless stated otherwise, the following predictions use beam A, under zero pre-tension, at a temperature of 298.15 K, and with parameter C left at 1.0.

4.5.1. Added mass effect

The effect of including added mass was investigated for beam A. Figure 4.7 shows the predictions for immersion in gases, whereas figure 4.8 considers immersion in liquids.

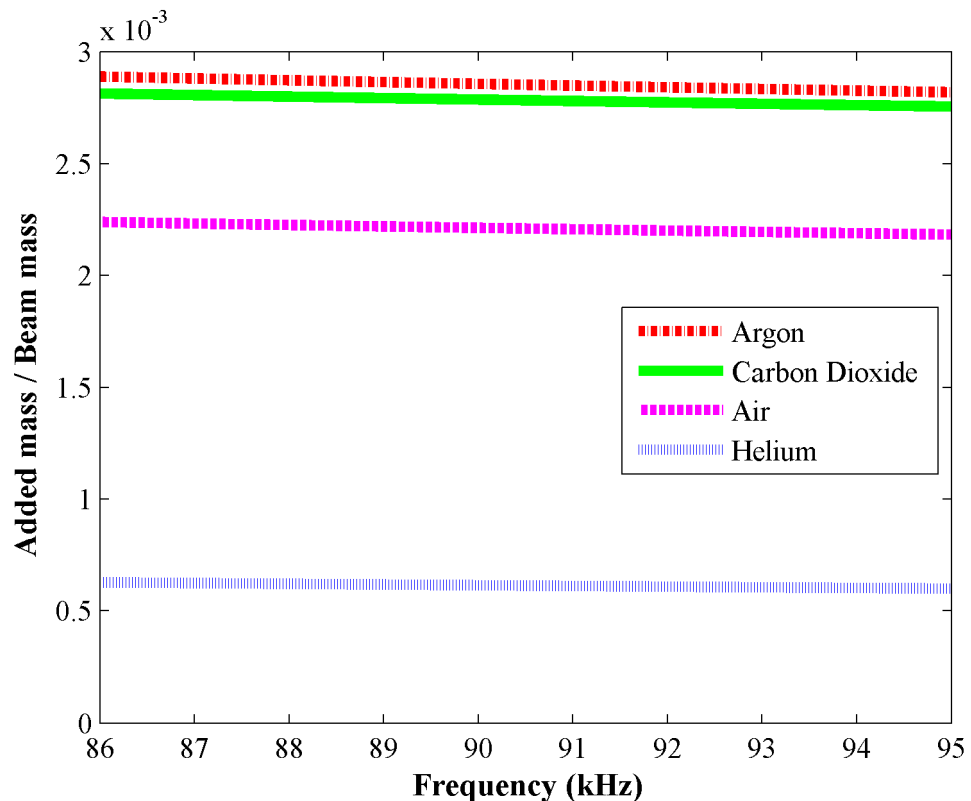


Figure 4.7: Ratio of added mass to beam A mass, for various gases in vicinity of the natural undamped frequency of the beam

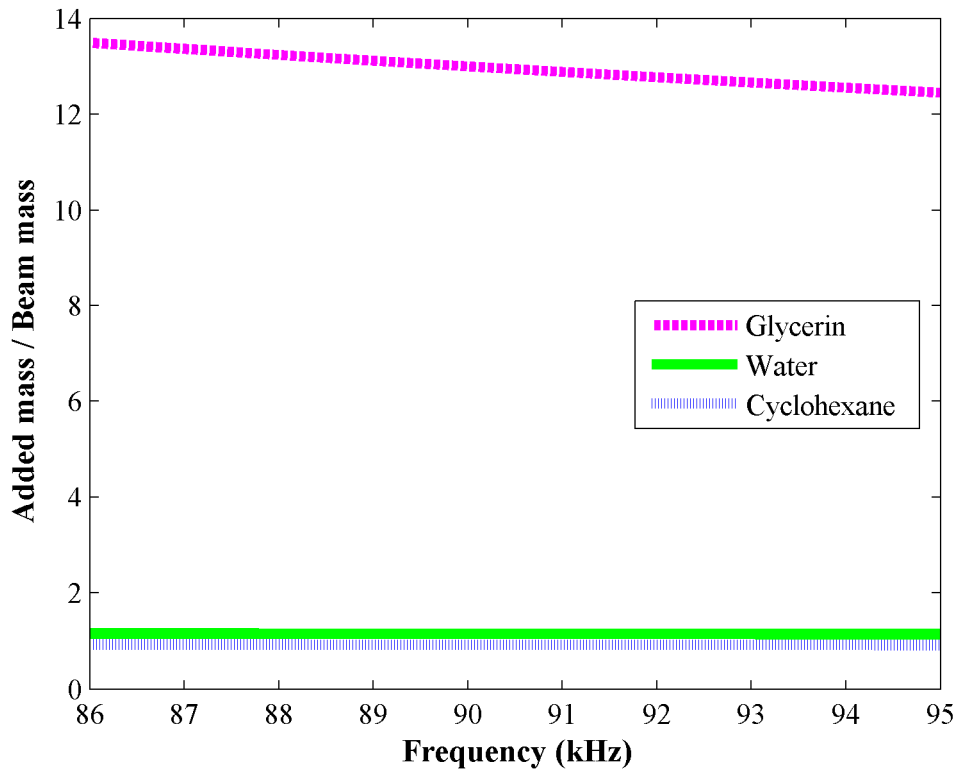


Figure 4.8: Ratio of added mass to beam A mass, for various liquids in vicinity of the natural undamped frequency of the beam

It is apparent from figures 4.7 and 4.8 that the ratio of the added mass to beam mass is insignificant for immersion in gases, but of importance for immersion in liquids. It may then be acceptable to neglect added mass in cases where the fluid density is far lower than the beam density.

To investigate further, the effect of including or discluding added mass was examined. The resonant peak, bandwidth and δF were calculated for beams A and B under both conditions, and the results compared. The gathered data is compiled in table 4.7, and demonstrates that added mass has little appreciable effect in the gases under consideration. Results for water however suggest that added mass is crucial when evaluating behaviour in liquids.

In conclusion it can reasonably be assumed that added mass is negligible in the work with gases. This assumption then validates the approach in section 4.4.1.

Fluid	Beam	h	Resolution (Hz)	With Added Mass			Without Added Mass			% change		
				δF (Hz)	Bandwidth (Hz)	Peak (kHz)	δF (Hz)	Bandwidth (Hz)	Peak (kHz)	δF	Bandwidth	Peak
Argon	A	3.0E-09	23.873	644.578		668.451			-3.704			
Argon	B	3.0E-09	23.873	286.479		286.479			0			
Helium	A	3.0E-09	23.873	6.14E+03		6.09E+03			0.777			
Helium	B	3.0E-09	23.873	3.51E+03		3.51E+03			0			
Water	A	2.5E-06	50.930	7.07E+04		8.56E+03			87.900			
Water	B	2.5E-06	39.789	5.30E+04		119.366			99.770			
Argon	A	1.0E-10	0.955		127.961	91.083	128.916	91.212		-0.746	-0.142	
Argon	B	1.0E-10	0.955		93.583	58.235	93.583	58.375		0	-0.240	
Helium	A	1.0E-10	0.955		50.611	91.190	50.611	91.218		0	-0.030	
Helium	B	1.0E-10	0.955		34.378	58.355	33.423	58.379		2.778	-0.041	
Water	A	1.0E-10	9.550		7.61E+03	61.682	2.01E+04	91.731		-163.744	-48.715	
Water	B	1.0E-10	9.550		3.41E+03	31.790	1.59E+04	58.840		-367.513	-85.092	

Table 4.7: Effect of added mass

4.5.2. Effect of fluid properties

The resonant frequency, bandwidth and jump point separation were modelled for beam A in a range of gases at various values of background displacement h . Figures 4.9, 4.10 and 4.11, respectively, illustrate the predicted behaviour. It is apparent that gases might be uniquely identified by using one or more of these measurands.

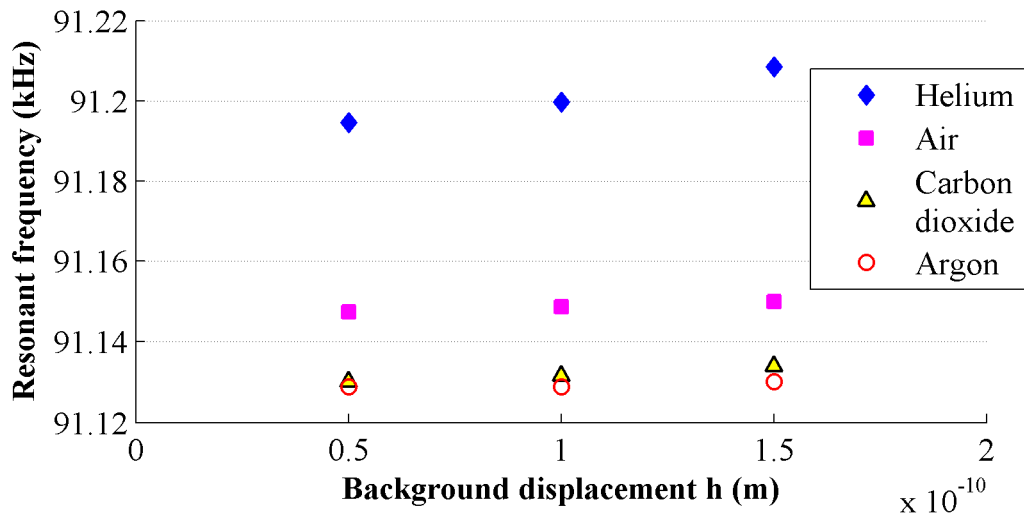


Figure 4.9: Modelled resonant frequency for beam A

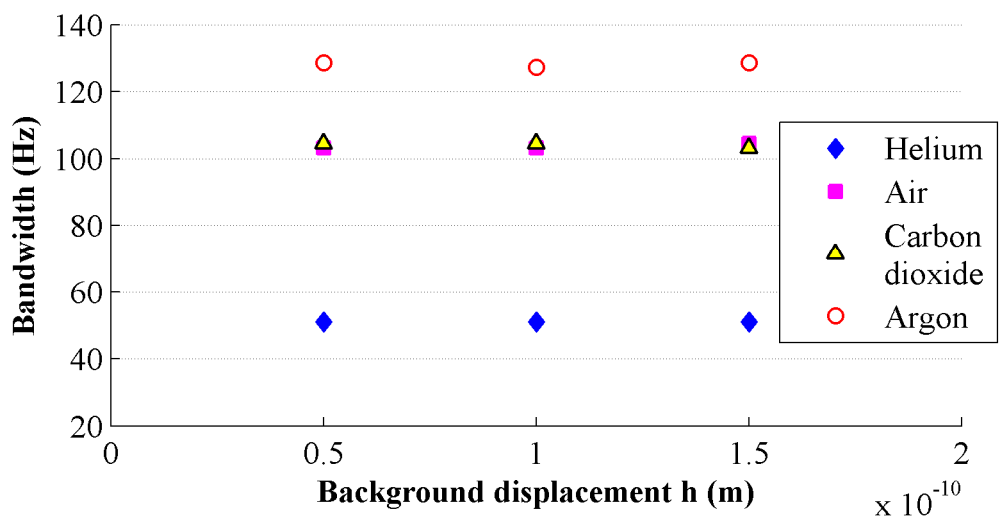


Figure 4.10: Modelled bandwidth for beam A

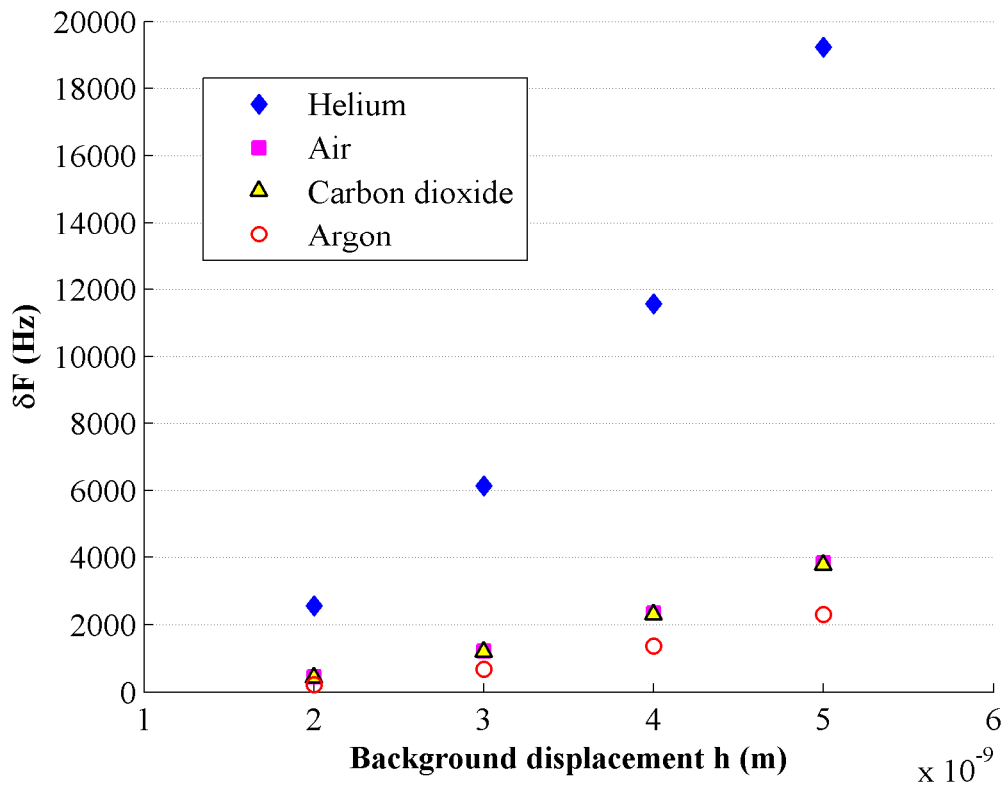


Figure 4.11: Modelled δF for beam A

Table 4.8 shows the maximum calculated values for Reynolds number, Keulegan-Carpenter number and Mach number, for the data displayed in figure 4.11. The constraints placed on the circular cylinder damping model are seen to be broken, with the Reynolds and Keulegan-Carpenter numbers exceeding the allowable values as discussed in sections 3.2.4 and 3.3.1. However it can be seen that Mach number remains low enough to allow the gases to be considered incompressible.

Fluid	Max Re	Max Kc	Max Mach
Air	7.6151	1.2958	0.0107
Helium	2.3654	2.9035	0.0095
Argon	6.6702	1.0341	0.0090
Carbon dioxide	14.4212	1.2882	0.0137

Table 4.8: Constraints

Figure 4.12 shows the jump point separation in gases for beam A with background displacement amplitude $h=2E-9m$. An increase in viscosity or density has the effect of reducing the jump point separation δF . There exist contours of equal δF across the plotted surface.

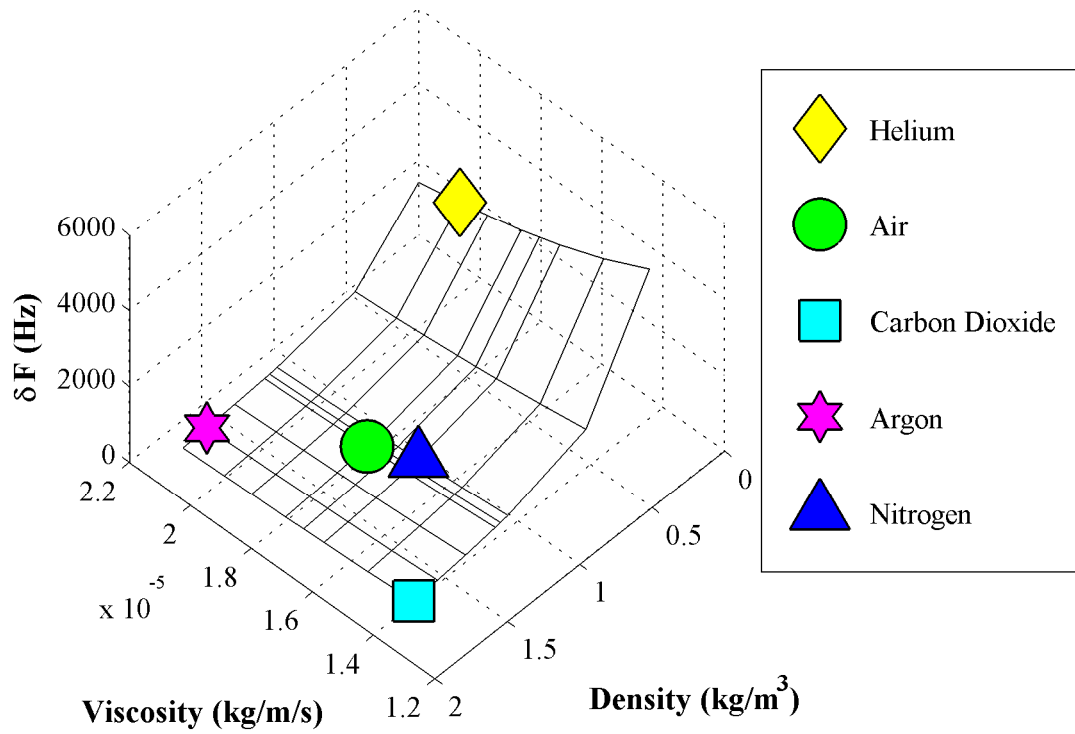


Figure 4.12: Three dimensional plot of jump point separation δF versus density and viscosity

4.5.3. Effect of boundary conditions

If the beam is subject to any pre-tension or compression, then this will affect the vibrations once it is actuated. To investigate the extent of this effect on the three pertinent measurands, the behaviour of beam A in argon was modelled. Temperature is assumed fixed as above, and extension term η varied to represent tension and compression. Figure 4.13 illustrates the predicted behaviour.

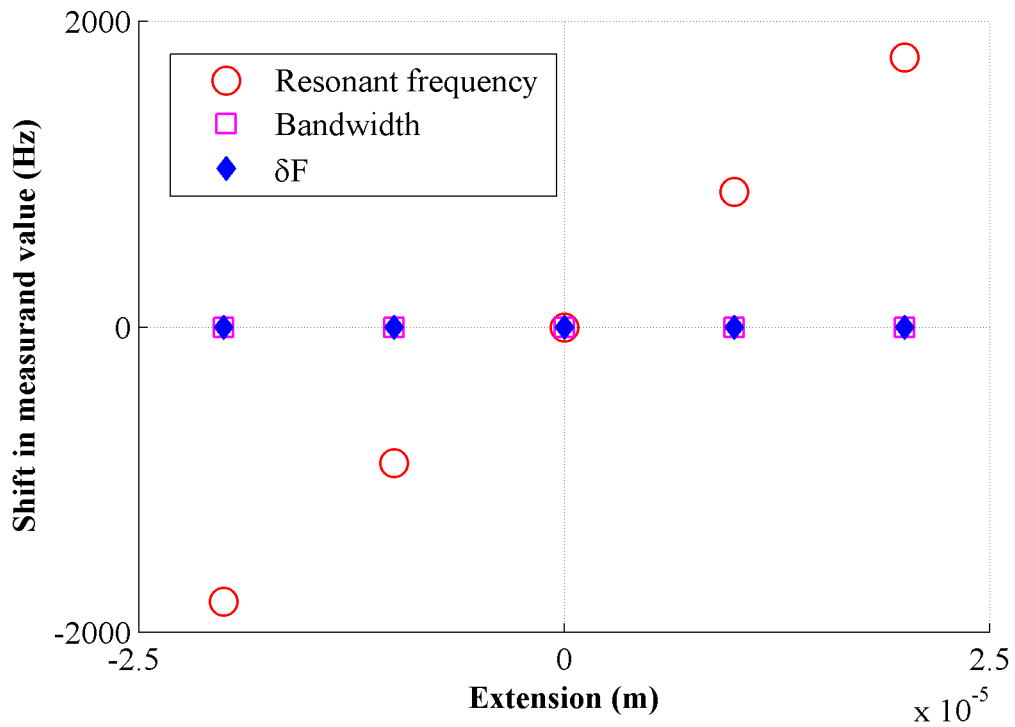


Figure 4.13: Sensitivity to boundary conditions.
Linear actuation at $h=1.45E-11$ m, nonlinear actuation at $h=2.2E-9$ m

It is apparent that over the range of consideration, extension η has negligible effect on bandwidth and δF , but a significant effect on the resonant frequency. Any changes in boundary conditions which effect the tension will alter the resonant frequency by a noticeable degree.

4.5.4. Sensitivity to changes in fluid properties

It was possible to investigate the relative effect of changing the density and the viscosity by equal amounts. Begin by assuming that the beam is immersed in carbon dioxide at 298.15K. Then model in two ways: the viscosity value is multiplied while the density is held constant, and vice versa. Resonant frequency, bandwidth and δF are then calculated, using appropriate values of h .

Figures 4.14 illustrates that, over the range of consideration, the resonant frequency of beam A changes more with density than with viscosity. The opposite is true however for bandwidth and δF ; Figures 4.15 and 4.16 show that changes in viscosity have the greater effect.

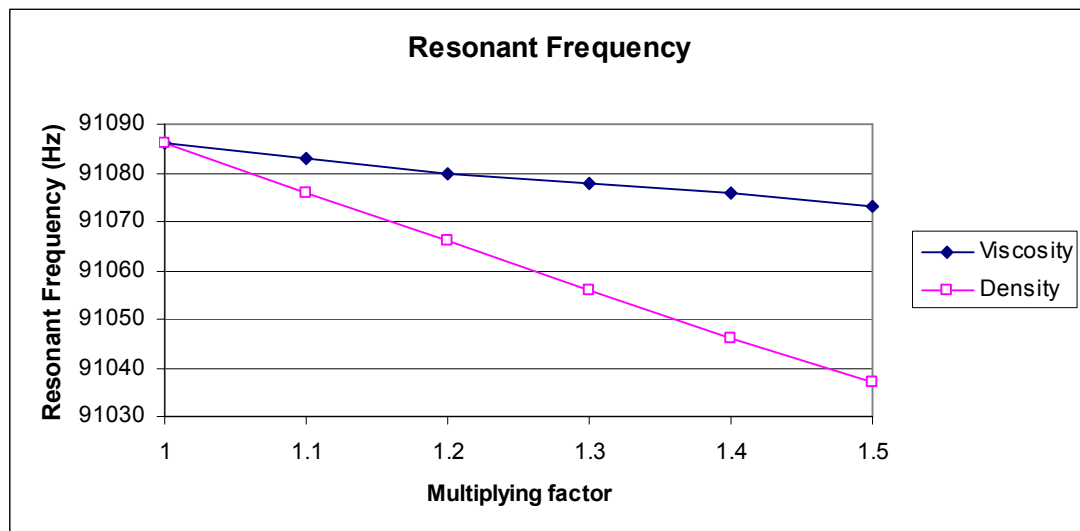


Figure 4.14: Sensitivity of resonant frequency. $h=8.5E-11$ m

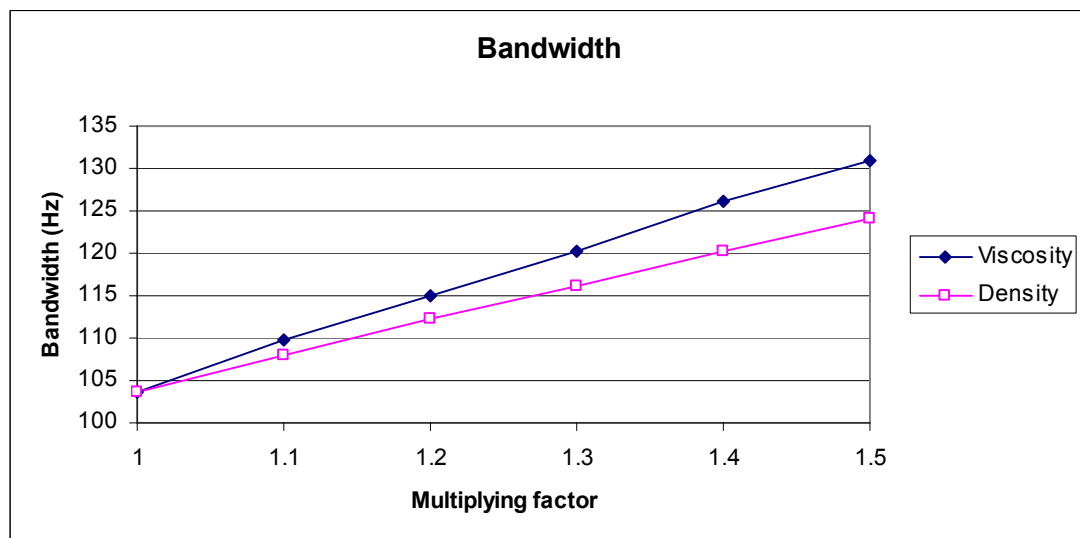


Figure 4.15: Sensitivity of bandwidth. $h=8.5E-11$ m

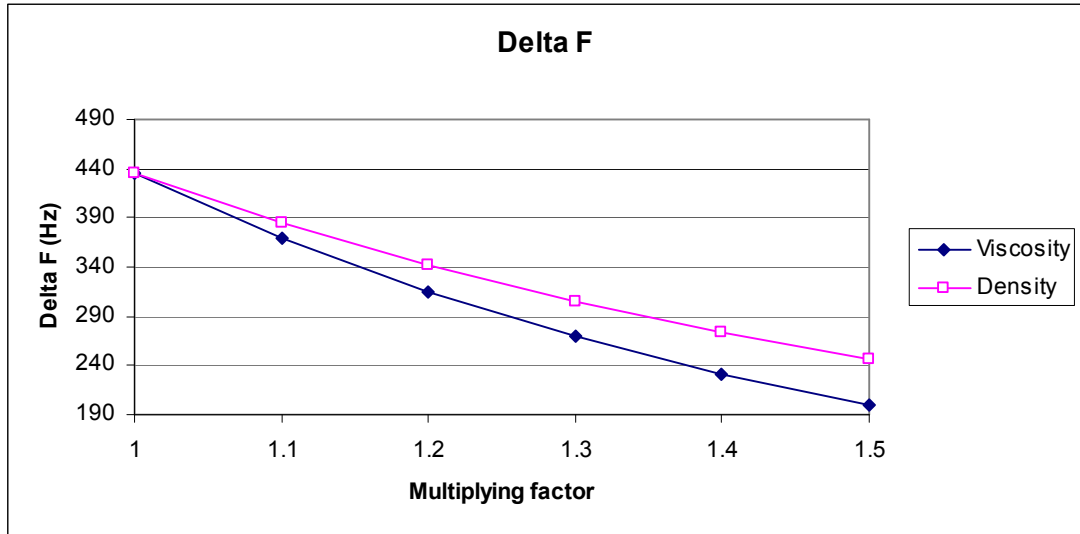


Figure 4.16: Sensitivity of ΔF . $h=2E-9$ m

The extent of the effect on each measurand is examined in figures 4.17 and 4.18. The shift in each measurand value is plotted against the viscosity and density change respectively. It is apparent that, over the considered range, ΔF is the most sensitive measure to changes in the fluid properties.

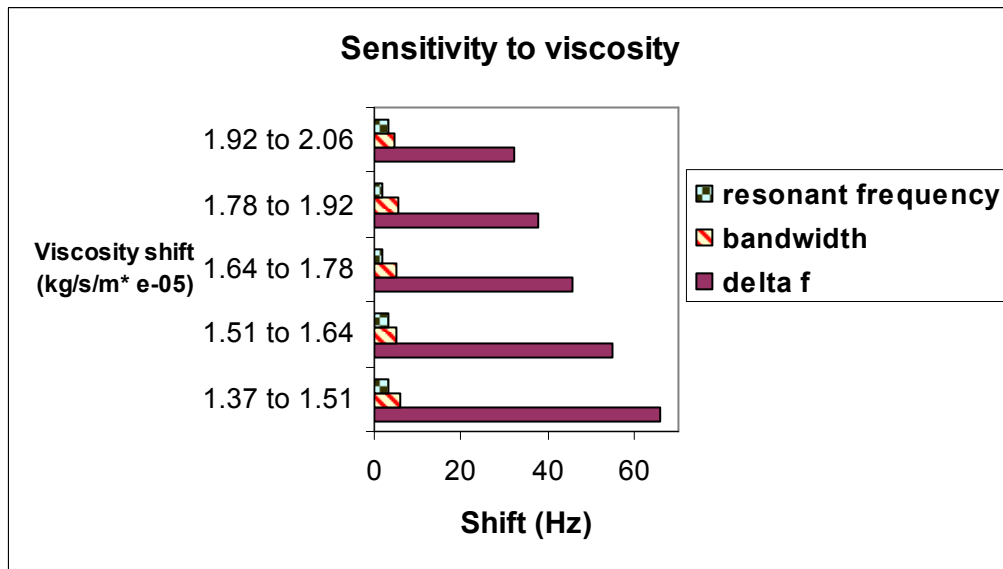


Figure 4.17: Sensitivity to viscosity. Constant density

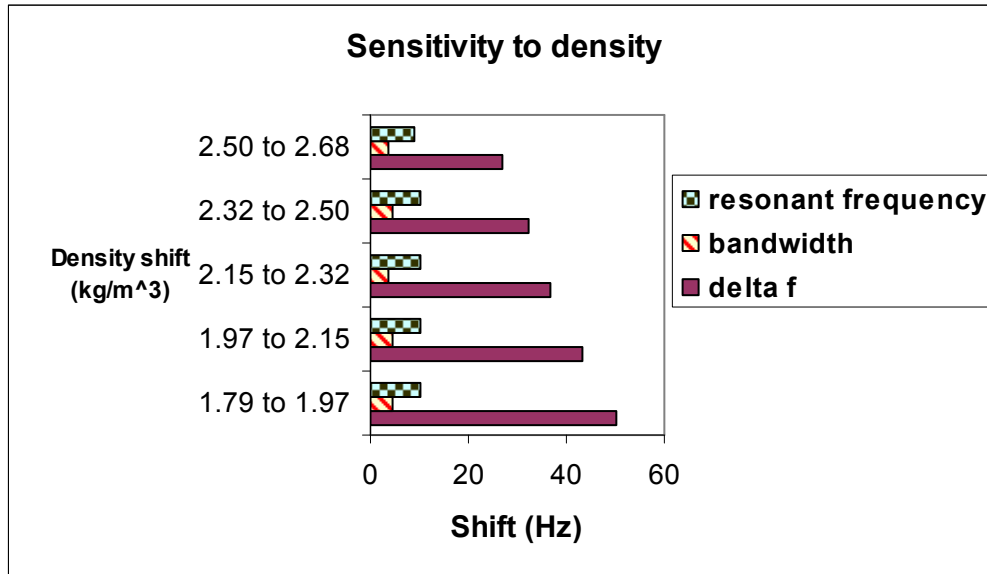


Figure 4.18: Sensitivity to density. Constant viscosity

4.5.5. Beam dimensions

In order to investigate the effect of altering beam dimensions, the behaviour of beams A and B in carbon dioxide was modelled for a range of background displacement h . Figure 4.19 shows that, over the range of consideration, displacement h gives a greater value of δF for beam A than beam B. It also appears that δF grows more rapidly with h for beam A than beam B.

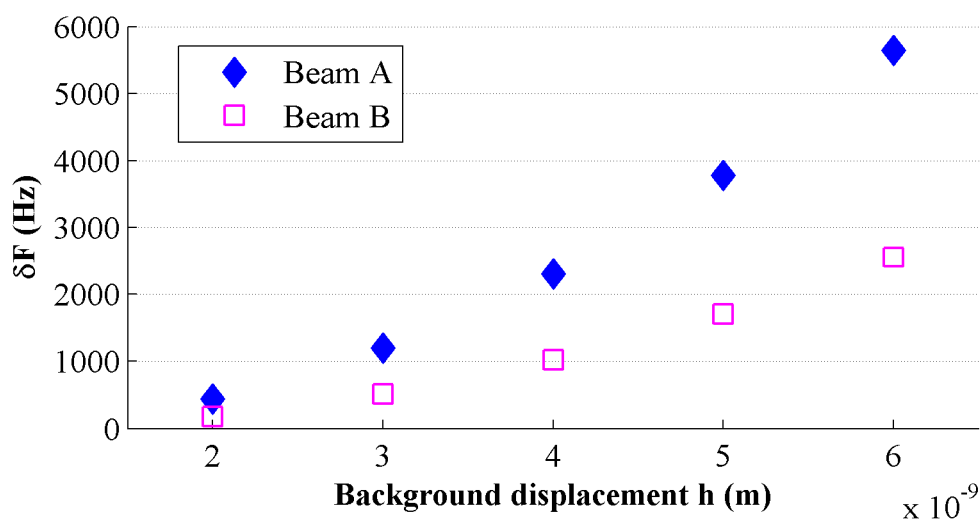


Figure 4.19: Comparison of beams A and B in carbon dioxide

A similar approach to that in section 4.5.4 was then taken, and the sensitivity of δF to changes in viscosity or density was examined at $h=2E-9$ m. Figures 4.20 and 4.21 indicate that the shorter, narrower beam A, with a higher resonant frequency, would exhibit the greater sensitivity to changes in fluid properties.

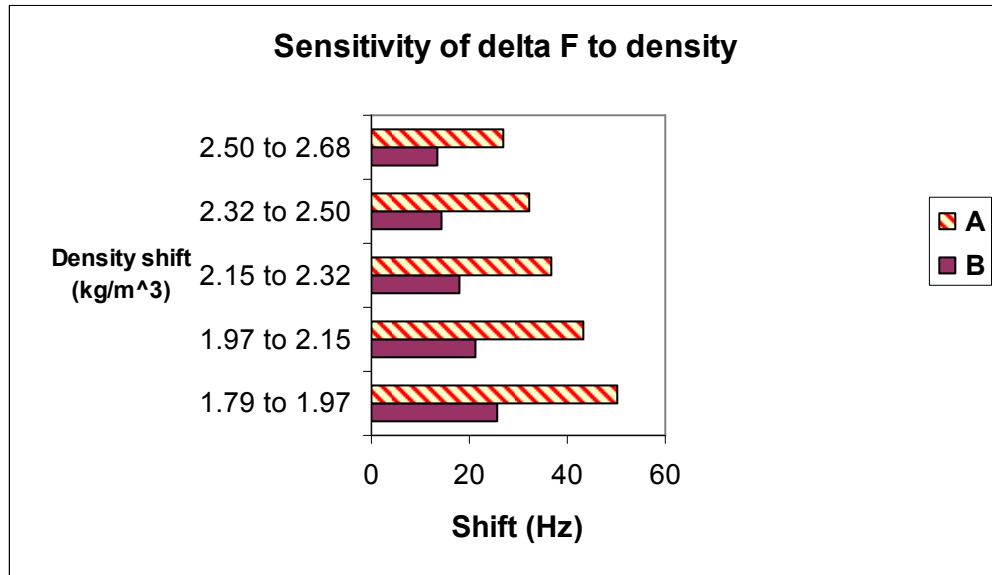


Figure 4.20: Shift in δF with density. Constant viscosity

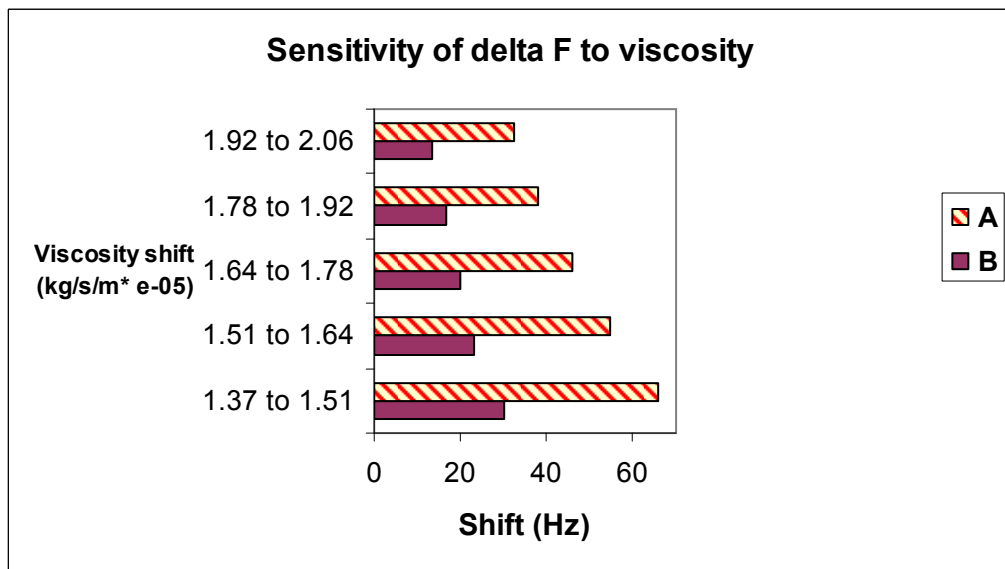


Figure 4.21: Shift in δF with viscosity. Constant density

4.5.6. Beam materials

The choice of beam material has an obvious effect on vibrational characteristics. As silicon devices are most likely to be used in the experimental work, it may be profitable to investigate the relative behaviour of silicon <100> and silicon <110> beams. As in section 4.5.4, behaviour was modelled in a gas initially with properties of carbon dioxide, then viscosity was varied and density held constant. Figure 4.22 shows that a silicon <110>, with higher Young's modulus, should outperform a similar <100> beam at equivalent h. It is apparent though that a relatively small increase in h can see the <100> beam reach the performance of its <110> counterpart.

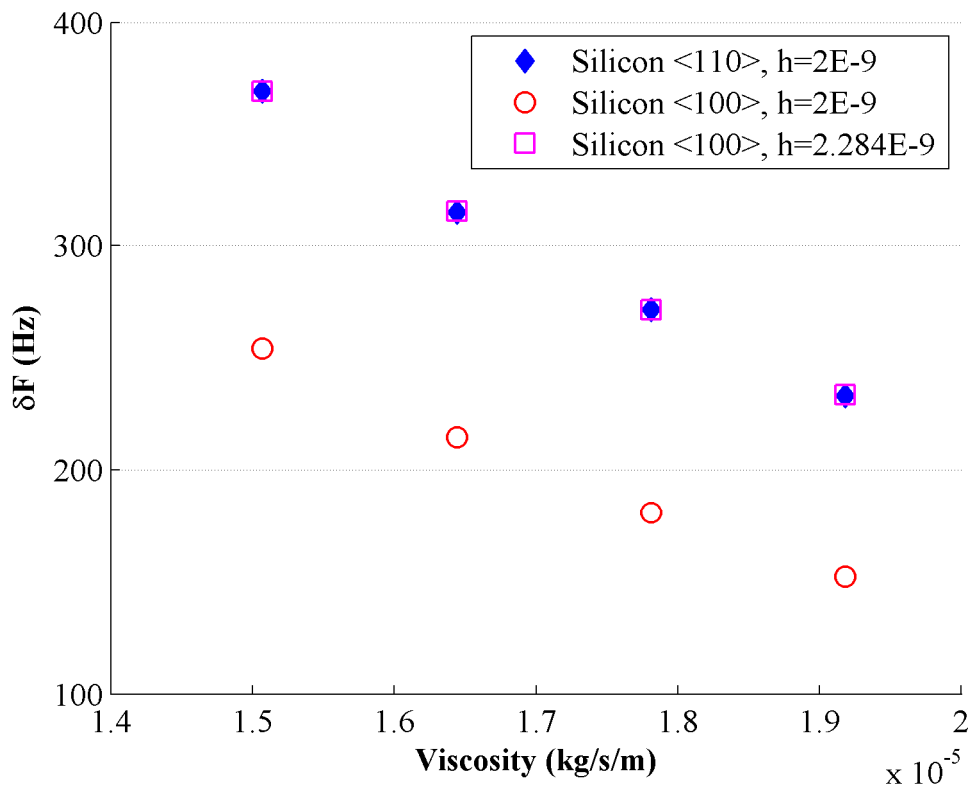


Figure 4.22: Comparison of Silicon <110> with <100>

4.5.7. Using ODE solvers in Matlab

Thus far, all modelling has been carried out using the single mode, single harmonic, frequency-response relationship developed in section 4.3.1. As a comparison, compare this approach to that of using an ODE solver in Matlab.

The equation to solve with such an ODE solver would then be $\ddot{T} = \frac{1}{C_1} \{ F_1 \sin \omega t + F_2 \cos \omega t - C_2 \dot{T} - C_3 T - C_4 T^3 \}$. This approach has the advantage of including all harmonics, but the disadvantage of only being able to predict one of the jump points, that for increasing frequency (i.e. the upper jump point). However, it can still be useful in indicating the correctness of the chosen harmonic balance method.

Figures 4.23 to 4.25 were produced by incorporating an ode45 solution with a harmonic balance solution. The ode45 solver is based on an explicit Runge-Kutta formula, and is recommended as a first-try solution, with medium accuracy.

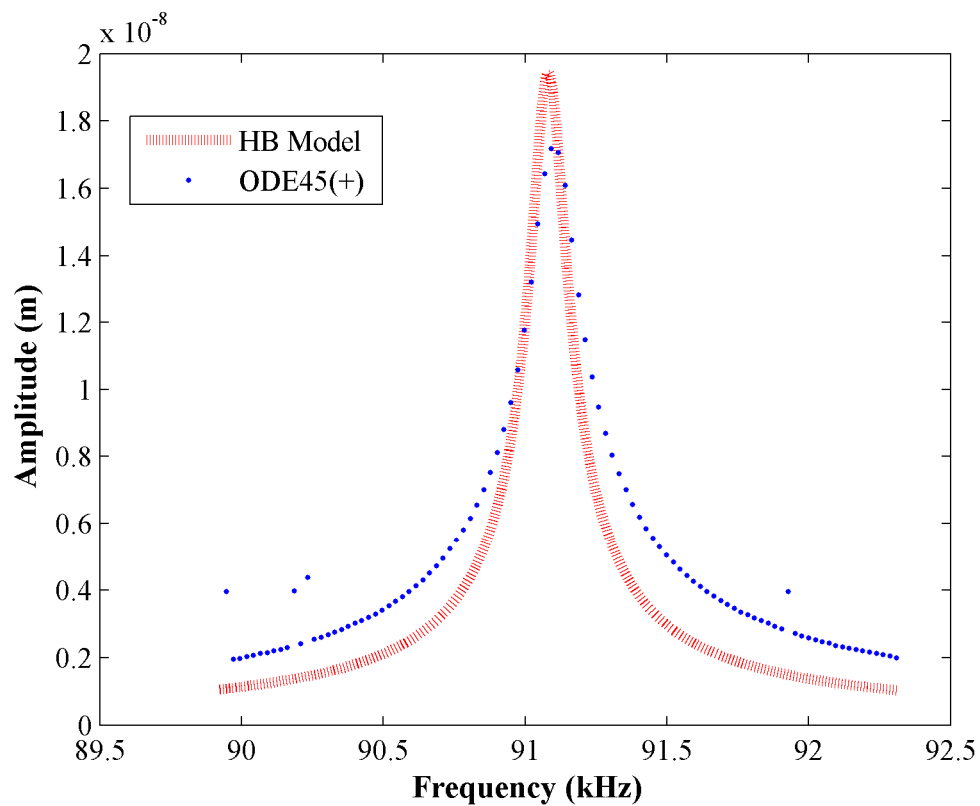


Figure 4.23: Harmonic balance versus ODE45 solver – linear. Argon with $h=2E-11$ m

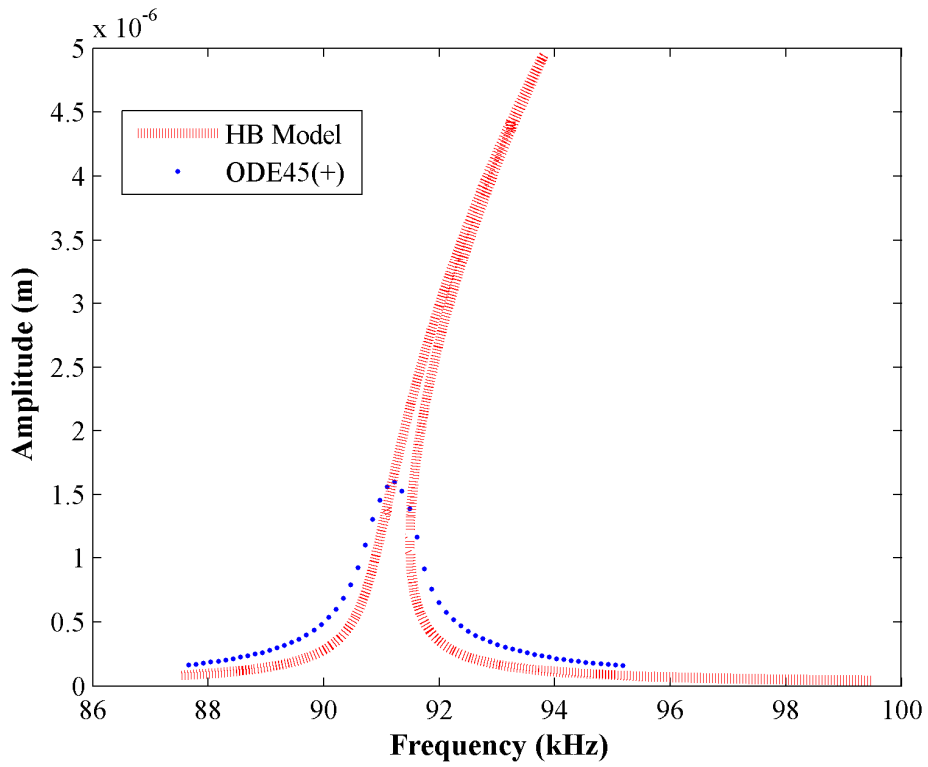


Figure 4.24: Harmonic balance versus ODE45 solver – nonlinear.
Argon with $h=5E-9m$

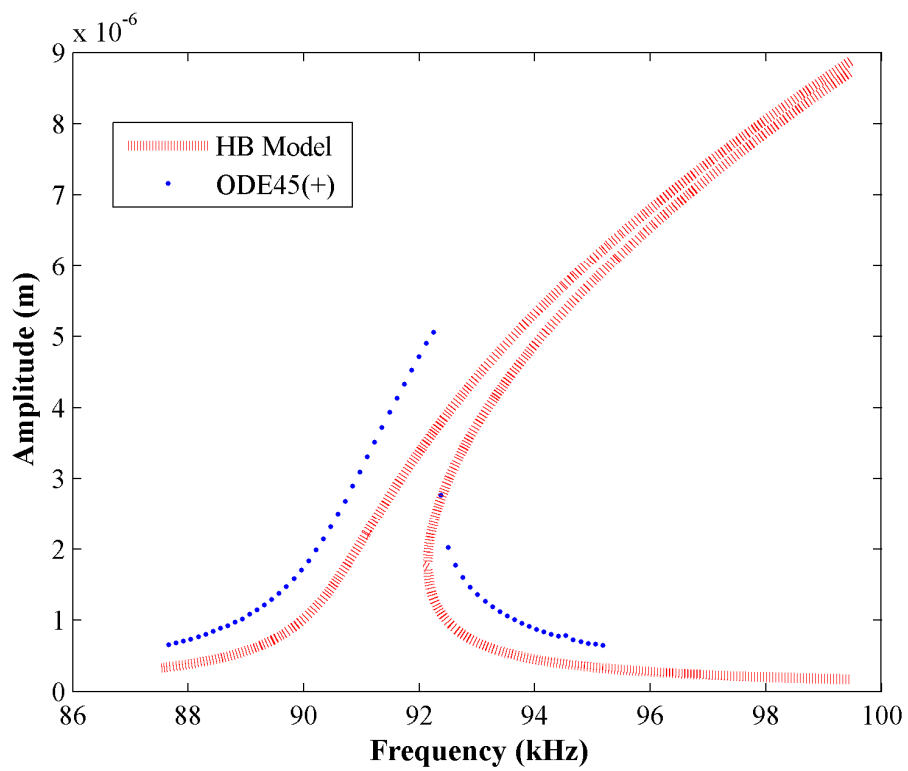


Figure 4.25: Harmonic balance versus ODE45 solver – nonlinear.
Argon with $h=2E-8m$

Figure 4.23 shows a reasonable agreement between the two methods of solution. There is some discrepancy in resonant frequency and bandwidth but it is difficult to draw any particular conclusions. Figures 4.24 and 4.25 however indicate that, as forcing is increased, so differences between the solutions are amplified. It would appear that using ode45 accounts for more damping on the system. In subsequent experimental work then, it might be expected that the damping encountered is greater than that included in the harmonic balance solution.

4.6. Summary

In this chapter a solution to the problem has been modelled and predictions made regarding beam dimensions and materials, actuation levels and expected behaviour in a range of fluids. Using this information, it is possible to proceed to the design and manufacture of suitable devices for experimental work.

4.7. References

1. Nayfeh, A.H., Mook, D.T. *Nonlinear oscillations*. Weinheim: Wiley-VCH, 2004.
2. Bishop, R.E.D., Johnson, D.C., *The mechanics of vibration*. Cambridge [Eng.] University Press, 1960.
3. Nayfeh, A.H., Pai, P.F. *Linear and nonlinear structural mechanics*. Hoboken: Wiley-Interscience, 2004.
4. Rao, S.S. *Mechanical vibrations*. 4th ed. Pearson Prentice Hall, 2004, pp. 912-914.
5. Bourouina, T. et al. 'Mechanical nonlinearities in a magnetically actuated resonator', *Journal of micromechanics and microengineering*, **10**, 2000, pp. 265-270.
6. Thomsen, J.J. *Vibrations and stability: advanced theory, analysis and tools*. 2nd ed. Berlin; New York: Springer, 2003.
7. Hassan, A., Burton, T.D. 'Extraneous solutions predicted by the harmonic balance method', *Journal of sound and vibration*, **182** (4), 1995, pp. 523-539.

Chapter 5

Design and fabrication of devices

This chapter starts by examining the material to be used in device fabrication. Initial modelling results are then used as a guide for synthesising suitable beam designs. There follows an overview of the fabrication process, and finally the fabricated devices are described and illustrated.

5.1. Material considerations

In the manufacture of MEMS devices, the choice of material is crucial. Material and device properties, durability, reliability, fabrication processes and cost must all be taken into account. When manufacturing a MEMS resonator, it is also desirable for the material to exhibit low intrinsic damping, so as to allow the exploitation of amplitude multiplication at resonance. Crystalline silicon performs favourably with regards to all of these criteria and is heavily used in MEMS manufacturing.

5.1.1. Crystalline silicon

Crystalline silicon behaves as an almost perfect Hookean material. On flexure, there is virtually no hysteresis and hence negligible energy dissipation. This allows for the manufacture of durable devices with high intrinsic quality factors. However, crystalline silicon possesses significant anisotropy, and an understanding of crystal orientation is essential when designing silicon structures.

Crystalline silicon has a cubic lattice structure. The lattice planes and directions are described by Miller indices. Crystalline silicon has three principal planes denoted (100), (110) and (111), as illustrated in figure 5.1. For a cubic crystal the direction $\langle lmn \rangle$ defines a vector normal to a particular plane (lmn) e.g. $\langle 100 \rangle$ defines the normal to plane (100).

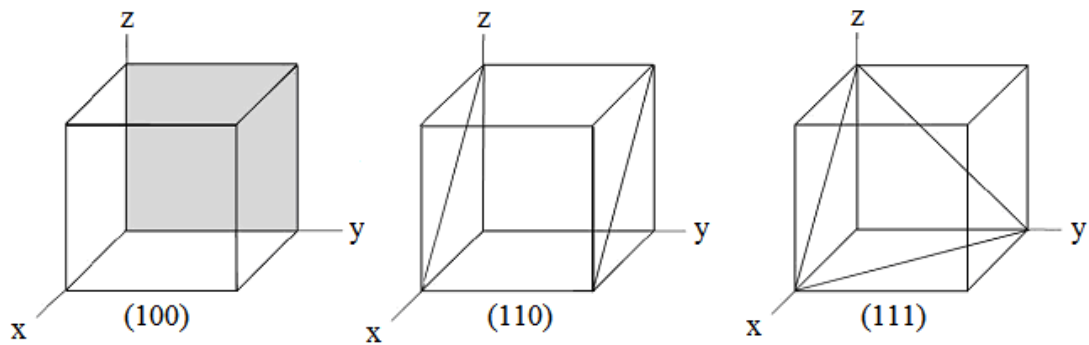


Figure 5.1: The principal planes of a silicon crystal

5.1.2. Silicon wafers

Due to the presence of anisotropy, it is essential to consider the precise cut of the silicon with respect to the principal planes. The majority of silicon MEMS devices are fabricated from silicon wafers cut from ingots along the (100) or (111) planes. Process limitations mean that small deviations of the wafer plane from (100) and (111) are however inevitable [1].

Wafers are characterised by their doping level, defined as n-type or p-type. Doping refers to the process of adding impurities to crystals to modify the electrical characteristics of the material. Dopants create mobile charge carriers in the silicon; n-type carriers behaving like negatively charged species, p-type like positively charged [2]. The silicon purity however still remains very close to 100%.

Figure 5.2 illustrates a (100) orientated silicon wafer and illustrates some of the planes within it. Flats are cut into wafers to indicate the planes.

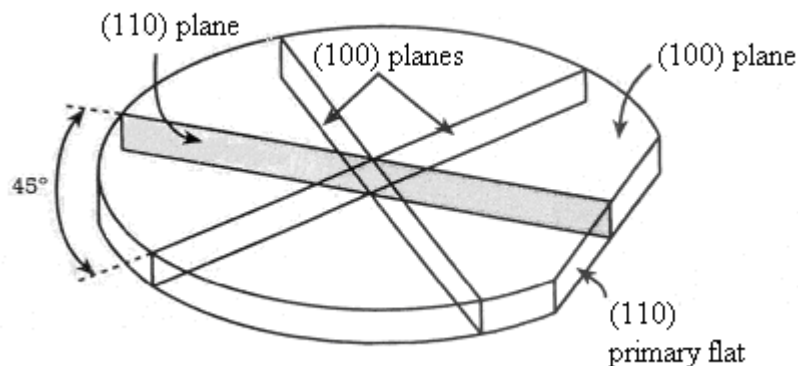


Figure 5.2: (100) type wafer, with various planes illustrated

5.1.3. Silicon On Insulator (SOI) substrates

Silicon on insulator technology (SOI) is commonly used in MEMS manufacture. SOI refers to the use of a layered silicon-insulator-silicon substrate, typically with silicon dioxide as the electrical insulator between a device wafer and a handle wafer. MEMS structures are fabricated in the device layer using processes which remove the underlying insulator to release the device.

5.2. Design considerations and limitations

Numerical predictions made in chapter 4 indicate some suitable beam dimensions and actuator displacements which will allow for the observation of jump phenomena in a range of gases (see sections 4.2.1 and 4.3.2). The beam depth is constrained by the choice of wafer. For the devices used in this work, a 15 μm thick device layer wafer was used. The length and width of resonator beams were then chosen so that the following conditions were met:

1. Jump phenomena can be observed with the available actuation technique.
2. Beam dimensions stay within the parameters required for Euler-Bernoulli theory to hold.
3. Beam width is sufficient to allow optical measurement of the device response.
4. Beam resonant frequencies remain within the range of signal analysing equipment.

In the following chapter the experimental equipment is discussed in more detail. An optical measurement method is employed, requiring the focusing of a laser beam onto the beam surface, hence condition 3. Condition 4 requires knowledge of silicon material properties, which are outlined in Appendix 2.

5.3. Fabrication process

The devices studied in this thesis were fabricated using an SOI-based micromachining process. The basic technique involves patterning of silicon layers using photolithography, followed by etching to produce the desired shapes. An SOI wafer with a 15 μm device layer, 2 μm silicon dioxide layer and 500 μm handle layer (see figure 5.3) was used to produce the resonator beams.

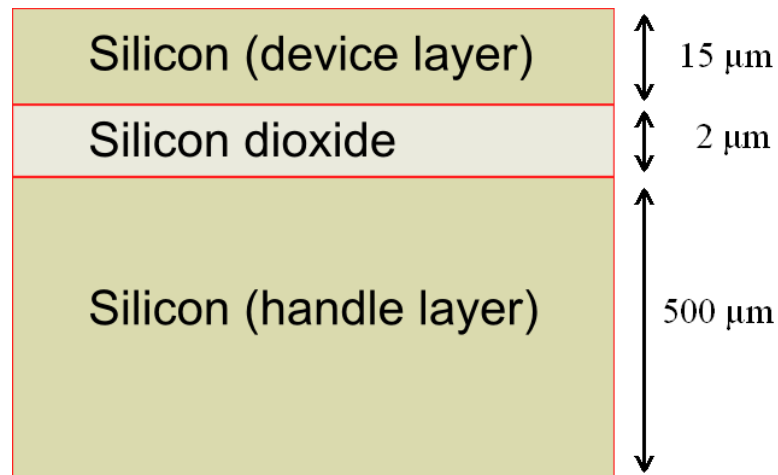



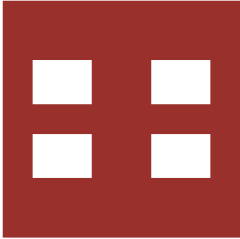







Figure 5.3: SOI wafer

5.3.1. Summary of process

Table 5.1 presents the steps involved in fabricating the beam resonators from the SOI wafer. Prior to fabrication, lithographic masks for beam definition were designed using L-Edit IC design software. The photolithography and etching processes are discussed in more detail in section 5.3.2.

Step No.	Process Description	Wafer Cross-Section	Mask Required	Notes
1.	Issue Silicon-On-Insulator (SOI) wafer			500 μm handle, 2 μm BOX (insulator) and 15 μm device layer thicknesses
2.	Deposit hard mask layer			Used later as mask for deep reactive ion etching (DRIE) of handle silicon
3.	Photolithography for DRIE etch			Positive photo-resist
4.	Plasma etch hard mask			
5.	Wet & dry removal of remaining photo-resist			
6.	Photolithography of device side silicon pattern			Photoresist used to define the beams
7.	DRIE of device side silicon, stopping on BOX layer			Short DRIE etch process used to cut through the device layer






8.	Protection layer			Protective resist applied to protect the beams during the DRIE of the handle layer silicon
9.	Wafer bond			Temporary bond to a backing wafer to assist with the DRIE etch process of the handle silicon
10.	DRIE Handle silicon layer			Longer DRIE process used, stopping on BOX layer
11.	Plasma etch BOX layer			This frees the beams from the BOX layer. They remain supported by the protective resist layer
12.	Solvent (acetone) release of die from backing wafer			Also has a plasma clean once die are removed from solvent. Finished die are ready

Table 5.1: Summary of fabrication process

5.3.2. Photolithography and etching processes

In photolithography, a photomask containing a geometric pattern of opaque and transparent regions is brought into contact with a silicon wafer coated with light-sensitive photoresist. Ultraviolet light is then directed through the mask, causing chemical changes in the exposed regions of the photoresist. If positive photoresist is used, then following processing the protected regions of the photoresist remain on the wafer. Subsequent etching removes clear regions on the wafer while opaque regions of the mask remain as oxide.

Plasma etching involves directing a high-speed stream of glow discharge (plasma) of an appropriate gas mixture at the wafer. The plasma source can be either neutral (free radicals and atoms) or charged (ions). Neutral particles react with the wafer surface creating volatile etch products which may be removed e.g. by vacuum pump. Ions can also have this effect, plus can produce sputtering effects, removing material by direct bombardment. There are numerous gases which may act as a source for the plasma, and they normally contain small molecules rich in chlorine or fluorine. For example, silicon can be etched with CF_4 and SF_6 , silicon dioxide with a CF_4/H_2 mixture, silicon nitride with a CF_4/O_2 mixture [2].

The shape of plasma-etched features depends strongly on the pressure in the plasma etcher. Reducing pressure also reduces the etch rate, but increases the directionality of the process. For a charged plasma source, at the extremes of low pressure and high directionality, the process is known as reactive ion etching. Etching processes may use a photoresist mask, although for very deep etches a harder mask may be required e.g. silicon nitride.

Deep reactive ion etching (DRIE) can create deep, steep-sided features in wafers with high precision. A side effect of glow discharge is the creation of polymers, and the deposition of polymer from the etchant may be exploited. In a process developed by Bosch, a DRIE etch proceeds in alternating steps:

- a standard reactive ion etch in a SF_6 plasma
- polymer deposition from a C_4F_8 plasma

Each step lasts for several seconds. Polymer at the bottom of the feature is removed rapidly by the reactive ion etch, but lingers on the sidewalls. As a

consequence, the top of the feature does not become wider as the sidewalls remain protected. Once the sidewall polymer is eventually eroded, so the polymer deposition step is repeated. By repeating these etch/deposit steps many times, it is possible to make a large number of very small etch steps with very little effect on the sidewalls. The DRIE process used for devices in this thesis was performed by INEX of Newcastle upon Tyne, using a STS Advanced Silicon ICP Etcher, and with an etch rate of between approximately 5 to 8 μm per minute.

5.4. Fabricated devices

The resonator beams were fabricated on an SOI wafer divided into multiple 8mm square dies. Dies containing resonator beams held four identical beams, oriented so that the neutral axis was perpendicular to the primary flat. As a consequence, when considering transverse vibrations of the beams, it was appropriate to consider the Young's modulus for the $\langle 110 \rangle$ direction.

Beams of varying dimensions were produced, although in this work the focus is on beams of dimensions 1200x30x15 μm (beam A), and 1500x75x15 μm (beam B), with a 500 μm thick handle layer in each case. Beams A and B, and the clearances around them, are shown in figures 5.4 and 5.5 respectively.

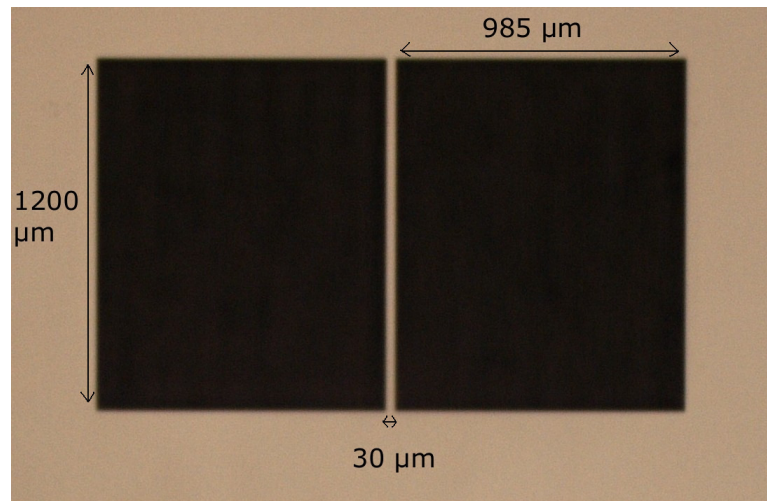


Figure 5.4: Photograph of beam A

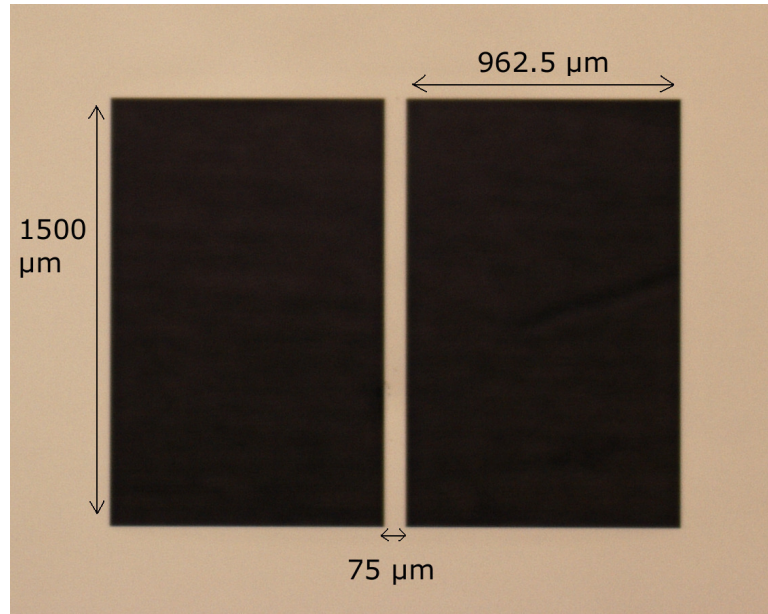


Figure 5.5: Photograph of beam B

For the SOI wafer, it is recognised that there will be some degree of misalignment in the crystal orientation. There is also likely to be some variation in the thickness of wafers or layers. The dimensions, properties and tolerances of the SOI wafer used in this work is given in table 5.2.

Manufacturer:	Ultrasil Corporation, Hayward, California
Device Layer:	
Diameter:	150+/- .2mm
Type/Dopant:	P/Boron
Orientation:	<100>+/- .5 degree
Thickness:	15+/- 1μm
Resistivity:	.01-.02 Ohm cm
Flats:	Semi std 1
Finish:	Polished
Buried Thermal Oxide:	
Thickness:	2μm +/- 5%
Handle Wafers:	
Type/Dopant	P/Boron
Orientation	<100>+/- .5 degree
Resistivity:	.01-.02 Ohm cm
Thickness:	500+/- 15μm
Finish:	Polished

Table 5.2: SOI wafer properties

5.5. References

1. Eley, R., Fox, C.H.J., McWilliam, S. 'Anisotropy effects on the vibration of circular rings made from crystalline silicon', *Journal of Sound and Vibration*, **228**(1), 1999, pp. 11-35.
2. Senturia, S.D. *Microsystem Design*. Springer, 2001.

Chapter 6

Experimental methodology and test equipment

This chapter describes the experimental equipment and procedures concerned with the testing of the beam resonators immersed in gases. The first section provides an overview of the optical workstation, comprising an optical profiler, laser vibrometer and signal analyser. The second section concentrates on the test jig and its component parts. Section three provides an overview of the gases used in the experiments. Section four outlines the testing and data gathering procedure.

6.1. Overview of test equipment

A suitable workstation was required to facilitate the measurement of the frequency response of the beam and the associated applied displacements. For this purpose an optical workstation was assembled, comprising of a Zygo NewView 5000 surface profiler alongside a Polytec OFV 3000 Vibrometer controller and OFV 501 Fiber Interferometer, with X-Y staging for control of device positioning, plus a HP 3562A dual channel dynamic signal analyser. Optical detection of device response is advantageous in that it is non-destructive. Figure 6.1 presents a schematic diagram of the workstation.

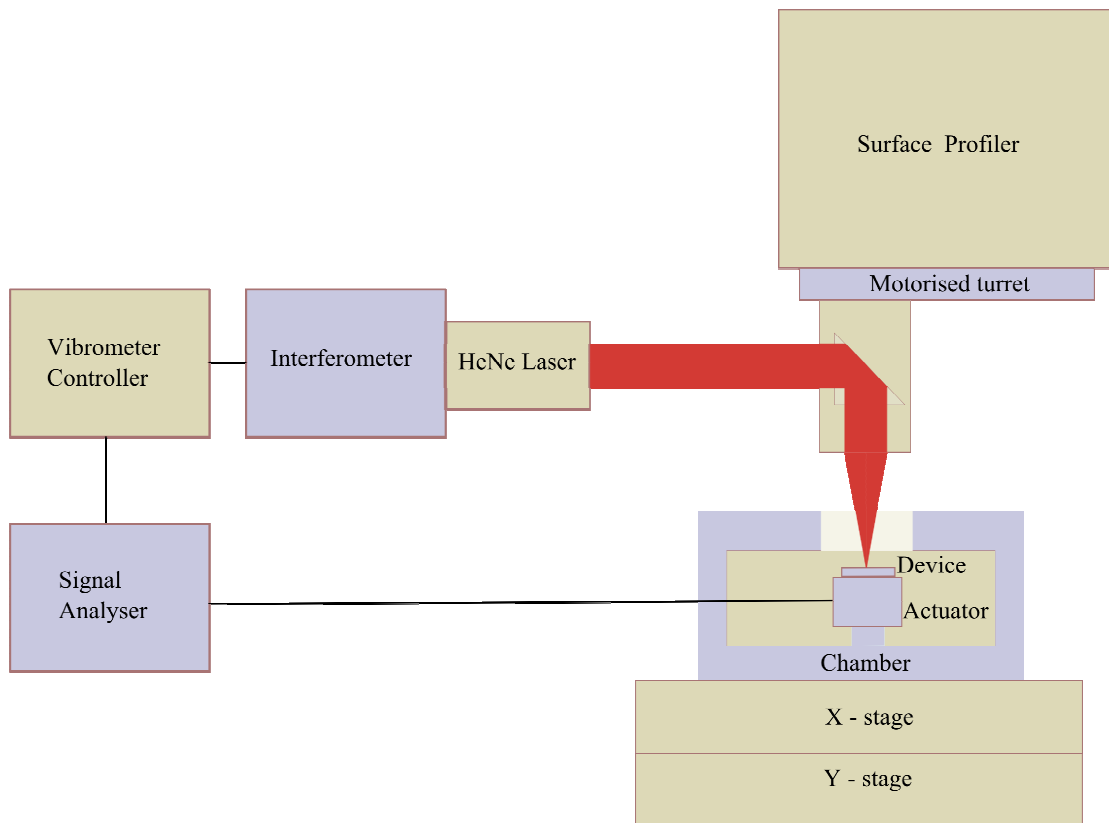


Figure 6.1: Schematic of optical workstation

6.1.1. Surface profiler

The Zygo NewView 5000 surface profiler uses scanning white light interferometry to acquire high resolution images. A white light source is collimated and a beam reflected down a microscope objective. This beam is split so that part of the light is passed to a reference mirror, while the remaining light is focused onto the surface of the sample to be imaged. The two beams are then reflected and recombined. The sample surface can be brought into focus by translating the objective so that the optical path lengths of each beam are identical. This then produces an intensity interference pattern on recombining the beams. When a vertical scan is performed across a surface, interference fringes appear on regions at the same height.

The Zygo NewView 5000 has various advantageous features [1]. Measurements are noncontact and fast. Profile heights from <math><1\text{nm}</math> up to 5mm can be scanned at speeds up to

The field of view can range from 0.04 to 17.5mm, although this can be increased using image stitching capabilities. The instrument comes packaged with MetroPro metrology software, which provides full system control.

For static measurements using scanning white light interferometry, a 10X Mirau objective was mounted on the turret. For vibratory measurements, an optical head was mounted for directing a laser beam from the interferometer onto the sample, and reflecting back to the interferometer.

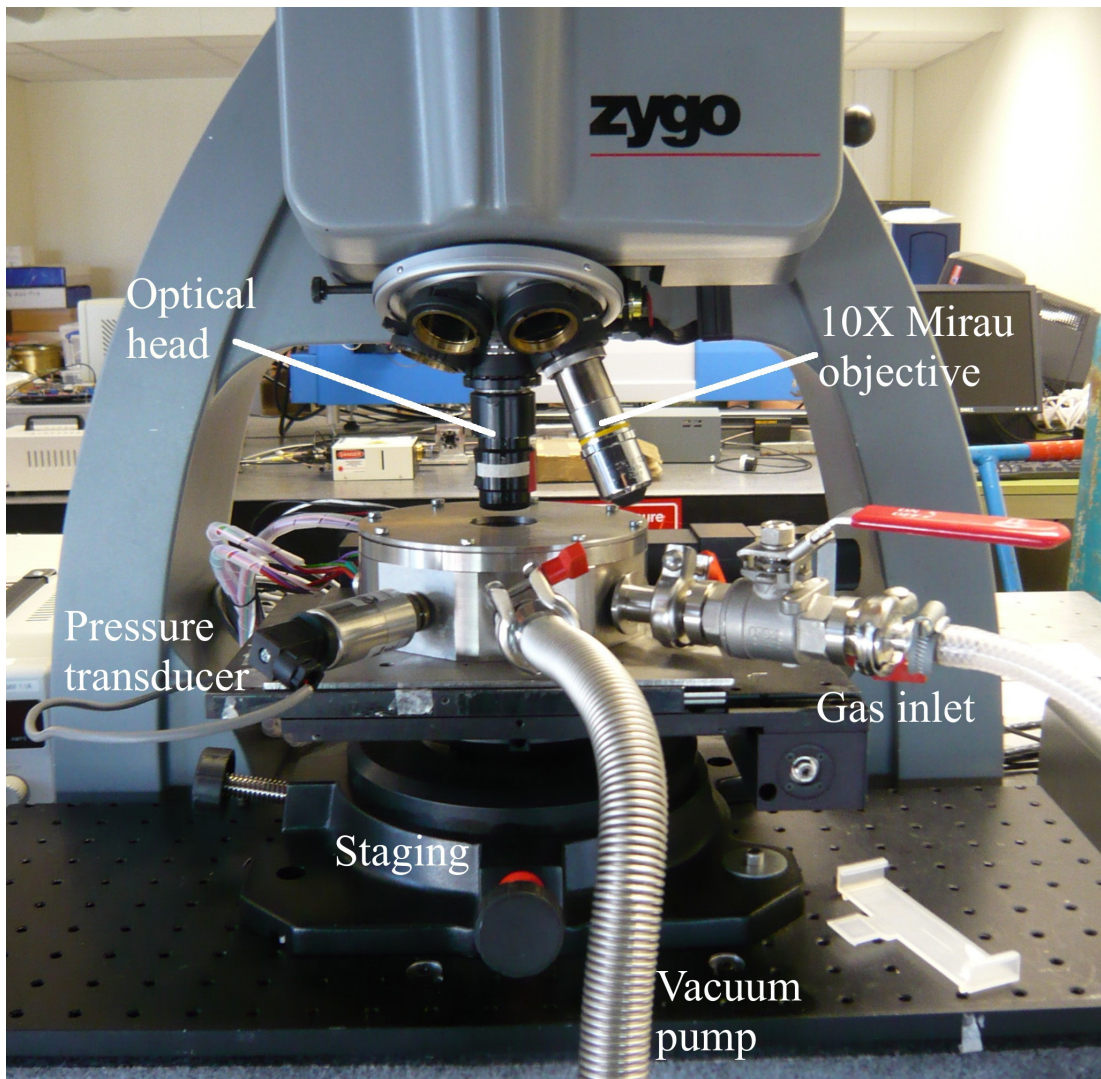


Figure 6.2: Zygo NewView 5000 surface profiler

6.1.2. Laser vibrometer

Vibratory measurements were performed using a Polytec laser vibrometer system, consisting of a Polytec OFV501 single mode fibre optic interferometer and a Polytec OFV3000 controller unit for the signal processing [2]. These instruments are shown in figures 6.3 and 6.4 respectively.



Figure 6.3: Polytec OFV 501 Fiber Interferometer



Figure 6.4: Polytec OFV 3000 Vibrometer controller

Vibratory motion is measured by measuring the Doppler frequency shift from laser light reflected back from the surface of the moving object. The optical arrangement of the vibrometer system is illustrated in figure 6.5.

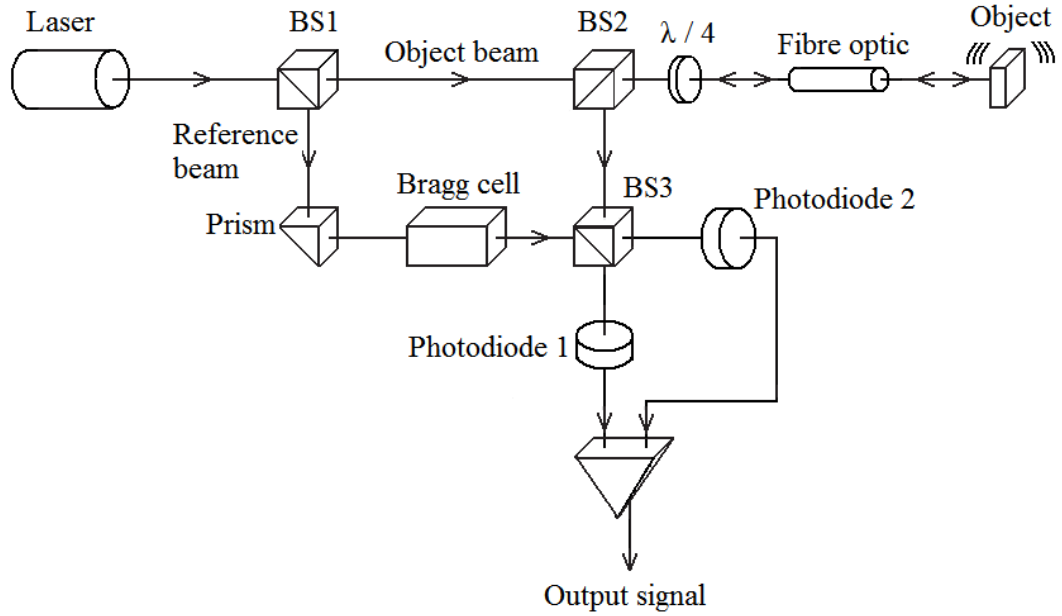


Figure 6.5: Laser vibrometer schematic

Light from a Helium Neon laser, of laser wavelength 633nm and cavity length 205mm, is divided by a beam splitter, labelled here BS 1. The object beam passes through a polarising beam splitter BS 2 and a quarter wave-plate before entering a single mode fibre optic cable. The object beam is then focused onto the object surface and back scattered laser light travels back up the fibre optic cable. The combination of the polarising beam splitter BS 2 and the quarter wave plate ensures that the beam returning from the object is directed towards the beam splitter BS 3. The reference beam is frequency shifted by a Bragg cell and thereafter interferes with the returning beam at the beam splitter BS 3. The output signals from BS 3 pass through a pair of photodiodes and are converted into electrical signals. These signals then enter a differential amplifier. The output signal voltage V_{output} from the amplifier is given by

$$V_{output} = K \cos \left[2\pi \left(f_{Bragg} + \frac{2v_o}{\lambda_{source}} \right) t \right] \quad (6.1)$$

where K is a constant denoting the conversion efficiency, f_{Bragg} is the Bragg frequency shift, v_o is the velocity of the object and λ_{source} is the wavelength of the source.

Equation (6.1) shows that the signal frequency is the sum of f_{Bragg} and the Doppler shift $f_{Doppler} = 2v_o / \lambda_{source}$. The Bragg frequency shift is required to determine the direction of the motion of the object relative to the source. The output voltage is fed into a RF signal-processing unit, which produces a voltage output proportional to the velocity of the object.

The vibrometer can provide both velocity and displacement signals. In this work the vibrometer was used to obtain velocity measurements, from which displacement amplitudes could then be calculated. For harmonic vibrations, the displacement amplitude \tilde{x} of the object is given by

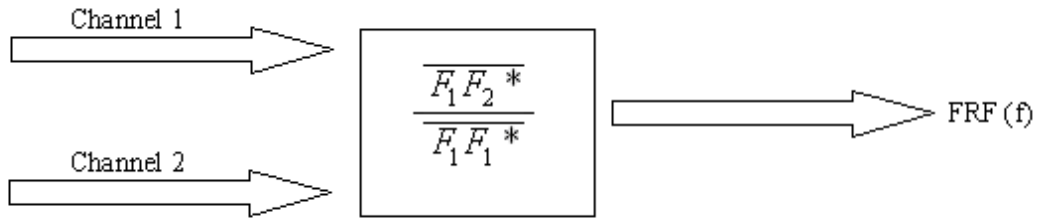
$$\tilde{x} = \frac{\tilde{v} V_R}{2\pi f} \quad (6.2)$$

where \tilde{v} is the velocity amplitude reading (in volts), V_R a velocity range setting on the vibrometer controller, and f the actuation frequency. The velocity range V_R is chosen so as to give optimal resolution of displacement readings; in this work, the settings of 125mm/s/V or 1000mm/s/V were used.

6.1.3. Signal analyser

A HP 3562A dual channel dynamic signal analyser allows dynamic testing from 64 μ Hz up to 100kHz [3]. Channel 1 of the signal analyser is the source and delivers voltages of up to 5V. This was used to provide excitation to the devices under test. Channel 2 of the signal analyser is the output signal produced by the vibrometer controller.

The HP 3562A is a Fast Fourier Transform (FFT)-based analyser. To calculate the frequency response function (FRF) of a device, the analyser begins by digitising the input at channel 1 by sampling at 256kHz. The sample data fills a data buffer. Once this buffer is full, a FFT of the data buffer calculates the frequency spectrum. The frequency response for the device is computed from the ratio of the cross spectrum to the power spectrum of channel 1, as referred to in figure 6.6.



where

F_1 is the FFT of the channel 1 signal

F_2^* is the complex conjugate of the FFT of the channel 2 signal and

$F_1 F_1^*$ and $F_1 F_2^*$ are the direct and cross spectra

Figure 6.6: Frequency Response Function from Signal Analyser operating in Linear Resolution Mode

In order to measure the frequency response of the devices, the operation mode of the analyser was set to Swept Sine. The analyser generates a fixed amplitude sine wave which excites the system. The frequency is slowly swept through the frequency range of interest. The response of the device is processed as described above and the FRF obtained. Monitoring of the device response was achieved by graphically displaying the power spectrum of channel 2.



Figure 6.7: HP 3562A Signal analyser

6.2. Description of test chamber

For testing of the beam resonators, the devices were mounted within a sealable test chamber. Figures 6.8 and 6.9 show the test chamber in its open and sealed states. The devices are mounted above a piezo-ceramic vibrator in the centre. Three peltier plates on the inner walls allow for temperature control within the chamber in its sealed state. Feeding into the chamber are gas inlets/outlets for gas introduction and vacuum pumping, a pressure transducer for pressure monitoring, and feedthroughs for a thermocouple and electrical wiring.

The test chamber was designed and drawn using Autodesk Inventor software, and is constructed from 303 stainless steel.

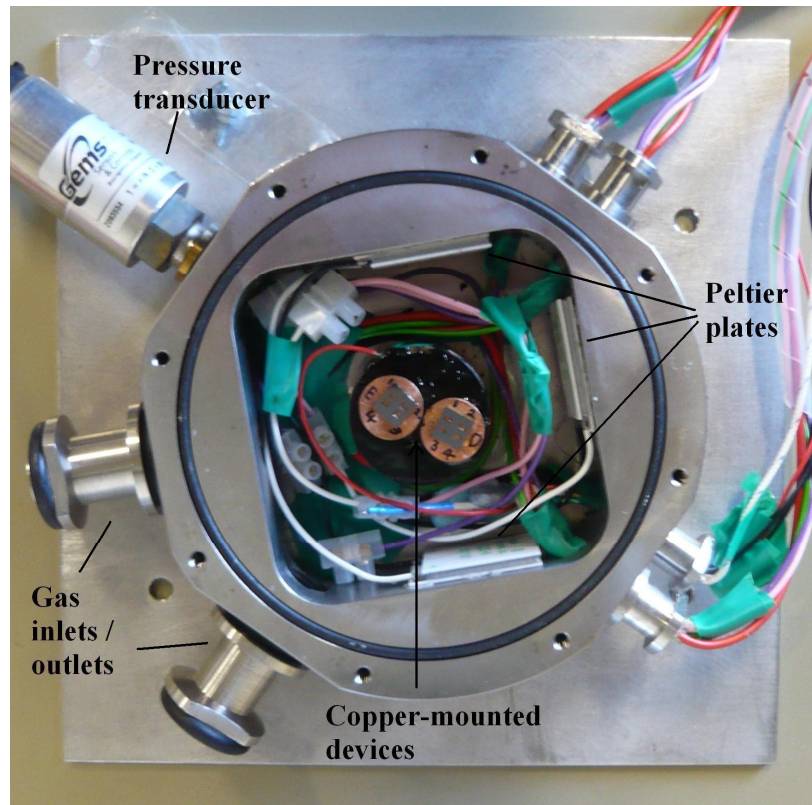


Figure 6.8: Plan view of open chamber

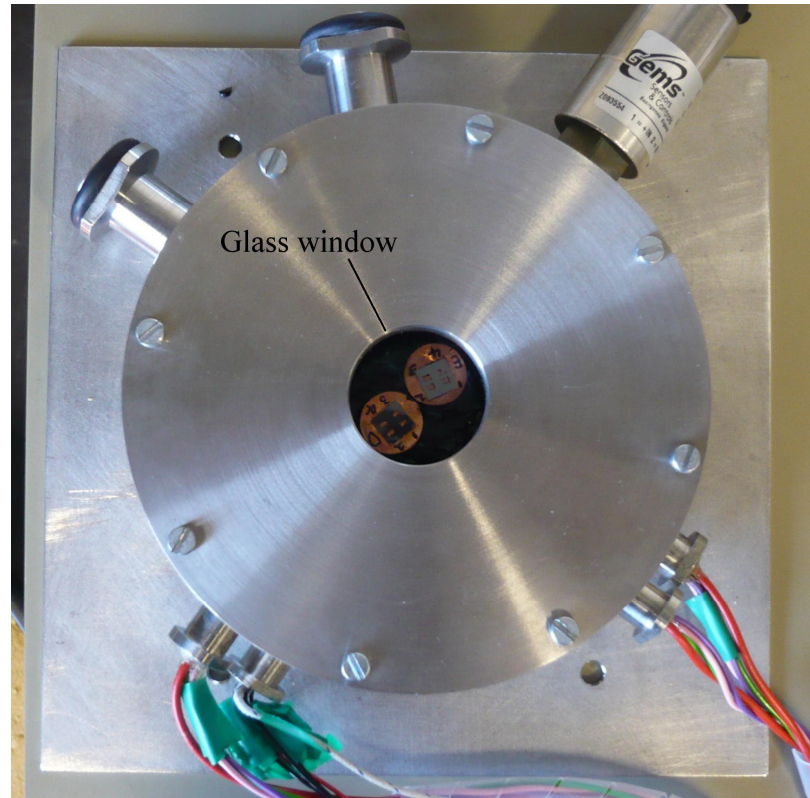


Figure 6.9: Plan view of sealed chamber

The test chamber allows for testing in low vacuum, in atmosphere, or at pressures reaching slightly above atmosphere when gases are introduced. Vacuum pumping achieved pressures down to approximately 2.8 mbar. The chamber is sealed by screwing a two-piece lid on top, resting upon a nitrile O-ring. Sandwiched between the lid pieces is a 2 inch diameter, 3mm thick Edmund Optics glass window with anti-reflection coating, secured with a nitrile O-ring. A 33mm diameter aperture in the lid then enables use of the laser vibrometer.

6.2.1. Peltier heating and temperature measurement

To provide some control of the ambient temperature within the test chamber, three Marlow Industries RC12-4 peltier plates were attached with Rite-Lok SL65 Silver Loaded Epoxy Adhesive to the inner walls of the chamber (see figure 6.8). When an electric current flows through a peltier plate, heat is absorbed at one face and liberated at the other. Heat is transferred from one side of the peltier plate to the other, against the temperature gradient. The direction of the temperature gradient is

determined by the direction in which the current flows. Peltiers are most commonly used as cooling devices.

Temperature within the chamber was measured using a Maplin K type thermocouple wire (Code: N37CB) with a FLUKE 53 II Thermometer. The thermocouple wire enters the chamber through one of the feedthroughs, and the thermocouple end positioned so as to be close to the devices in the centre of the chamber, without touching any part of the assembly.

Preliminary tests demonstrated that the peltiers could be used most effectively for introducing heat into the internal part of the chamber rather than extracting heat. By operating the peltiers in reverse, i.e. with a current flowing in the opposite direction to their normal mode of operation, it was possible to heat the chamber contents by an amount governed by the chosen operating voltage. Figure 6.10 shows how the temperature of the air within the chamber changed with time, for an operating voltage of 2V. The external air temperature is included for reference.

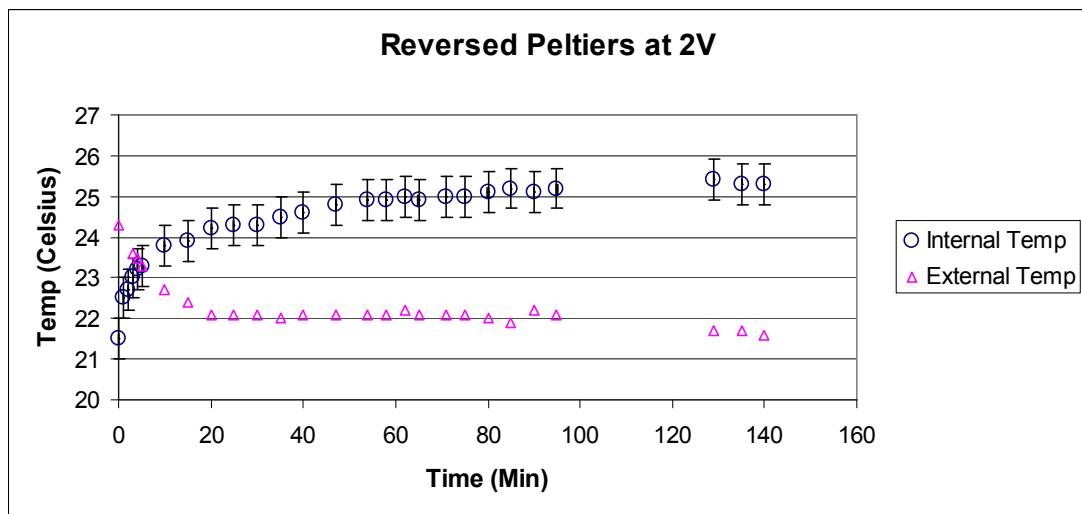


Figure 6.10: Internal temperature of test chamber versus time

6.2.2. Piezo-vibrator actuation

Actuation of beam resonator devices was achieved by means of a piezo-vibrator, as shown in figure 6.11(a). A Morgan Electro Ceramics PZT 5A1 piezo disk, of diameter 24mm and thickness 2mm, is sandwiched between a steel base and an upper

steel disk of diameter 35mm and thickness 2mm. Rite-Lok SL65 Silver Loaded Epoxy Adhesive fixes the piezo disk in place.

When a voltage is applied across the thickness of the piezo disk, it undergoes a change in dimensions in this direction, proportional to the applied voltage. When the steel base is earthed, applying a sinusoidal voltage to the upper steel disk causes the piezo disk to sinusoidally expand and contract, providing an actuation mechanism.

The silicon die containing the beam resonators were permanently attached to 2mm thick copper disks with Bond Lok B2012 Rapid 5-Minute Epoxy, to provide support to the fragile devices. These copper disks could then be temporarily attached to the top of the piezo-vibrator by using a wax resin – see figure 6.11(b). An electrical connection from the HP 3562A Dynamic Signal Analyser to the upper steel disk then allowed for control of actuation voltage and frequency, and hence a controlled method of transversely displacing the beam resonators.

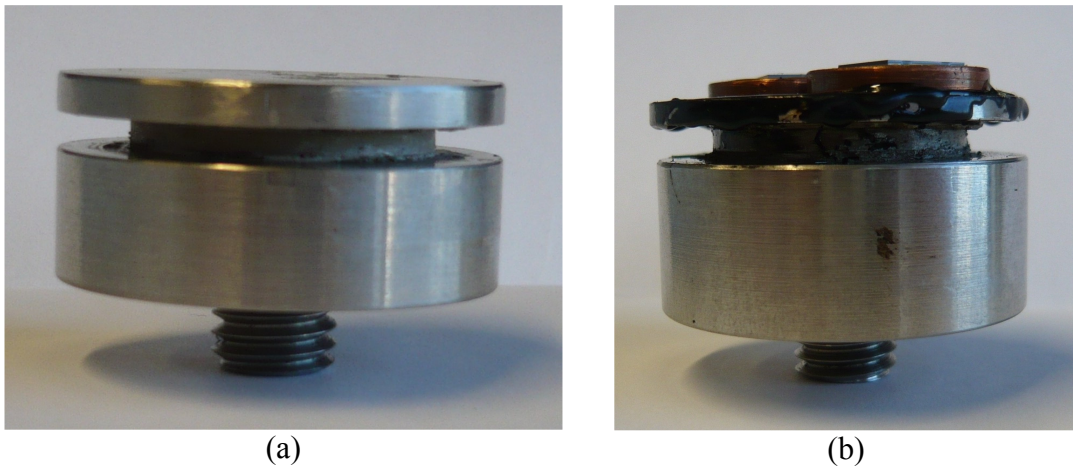


Figure 6.11: (a) Piezo-vibrator, (b) Piezo-vibrator with devices mounted

6.2.3. Pressure transducer

A Gems Series 2200 pressure transducer fitted to the test chamber allows for pressure monitoring (see figure 6.8). This is a 4 bar absolute transducer, with a 0-10V output. Attaching the output to a Wavetek Meterman Model DM9 digital multi-tester allows for output monitoring, and subsequent conversion of the output to bar provides the pressure within the chamber.

6.2.4. Imperfections

In setting up the experimental apparatus, certain imperfections were noted or anticipated.

Test chamber imperfections

To examine if the test chamber was perfectly airtight, the chamber was sealed and evacuated using a vacuum pump. The pump was then switched off, the pump outlet sealed and the pressure within the chamber monitored over a period of time. Figure 6.12 shows how the internal pressure varied with time, indicating that air was seeping into the chamber.

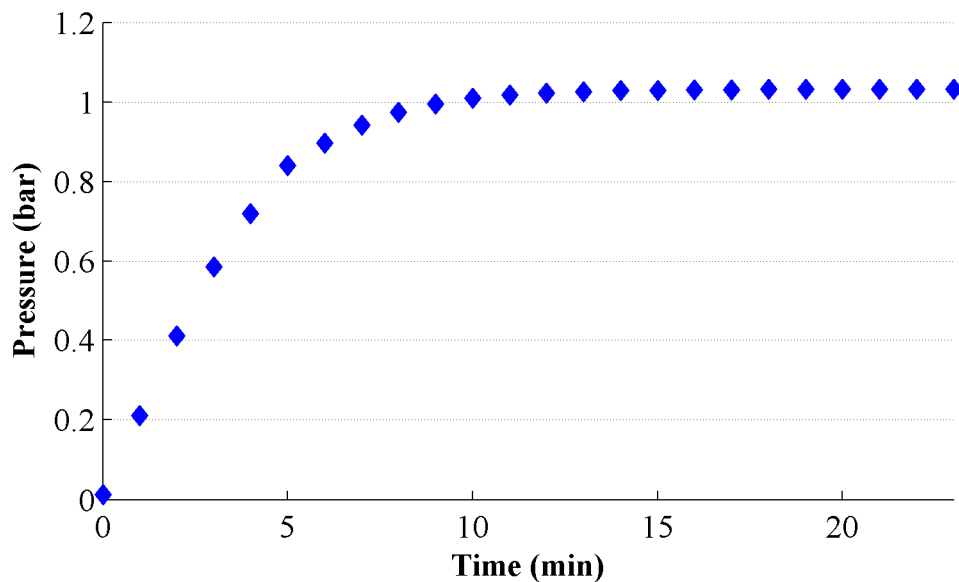


Figure 6.12: Pressure versus time for evacuated chamber

To further investigate, the chamber was evacuated of air, then filled with helium to a pressure above atmospheric. The gas inlet was then sealed and the internal pressure again monitored over a period of time. The results are shown in figure 6.13, and show that helium was escaping from the chamber.

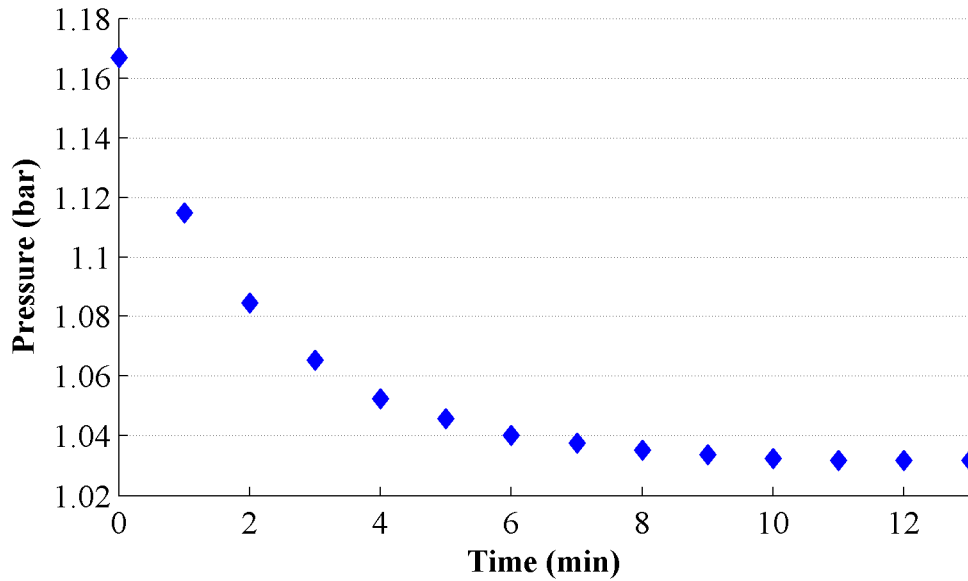


Figure 6.13: Pressure versus time for helium-filled chamber

It was apparent that the chamber could not be considered totally airtight. Further investigations failed to definitively identify the source of any leaks. It is possible, for example, that gas molecules could be passing through the electrical wiring or the thermocouple cladding, or bypassing one or more of the nitrile O-rings. To counteract the effect of leakage, subsequent experiments in gases were conducted at pressures slightly above atmospheric, with a permanent feed from the gas source, to maintain the pressure and to minimise the chance of any air molecules entering the chamber and diluting the gas. For experiments at low vacuum, the vacuum pump was kept continuously pumping so as to remove any air molecules which should seep into the chamber.

Heat and temperature

The test chamber is constructed from stainless steel and is not insulated, therefore there is potential for significant heat flow between the chamber and the surrounding atmosphere. The presence of leaks also allows for heat flow via convection in or out of the chamber. The temperature of any gas within the chamber cannot be guaranteed uniform, as there will be a slow introduction of gas from the pressurised source to maintain pressure, heat transfer between the gas and the chamber walls, and heat transfer between gas and peltier plates. Temperature is measured at one point in the chamber only, and cannot directly provide the temperature of the devices or piezo-vibrator, which are subsequently found to be crucial to resonator behaviour.

Mounting and bonding issues

When bonding the silicon dies to copper disks, there is a risk of introducing some deformation and tension or compression to the beams during the bonding process. Silicon, epoxy, copper, wax resin and stainless steel all have different linear expansion coefficients, so any change in temperature can also cause deformation and a change in the boundary conditions of the beams. Further complications can arise if any part of the silicon die handle layer has not been fully bonded to the copper disk, as this could allow areas of the silicon handle to vibrate out of synch with the piezo-vibrator.

Device inconsistencies

Initial tests showed that each of the four beams on a particular die could have slightly differing resonant frequencies in a given medium. This can be explained by either manufacturing or material inconsistencies, and necessitates the labelling of die and beams (see figure 6.14).

Impurities

During operation it is possible for impurities such as dirt or water vapour to settle on the beam resonators, altering their physical properties.

6.3. Test gases

Gases selected for experimental work were required to be Newtonian, and safe for use given the laboratory environment and experimental design. Gases are preferable to liquids in this work for several reasons:

- Piezo-vibrator actuation is useful in that it can provide high levels of displacement to the resonator beams. In the chosen gases it is easy to implement, but this may not be the case in liquids where electrical conductivity is far higher and the piezo can be shorted.
- The lower density and viscosity of gases allows for greater magnitude δF readings to be available with the given actuator.
- Measurement of beam vibration with the laser vibrometer may be complicated by liquid opacity or reflection from the liquid surface.

The selected gases are listed in table 6.1. For the relevant gas properties, refer to Appendix A.

Gas	Source / Supplier	Notes
Air	Atmospheric	Susceptible to changes in humidity
Argon	BOC	BOC Pureshield Argon UN 1006 EC No. 2311470
Helium	BOC	BOC Helium UN 1046 EEC No. 2311685
Carbon Dioxide	Distillers Company	Code 1013

Table 6.1: Selected test gases

6.4. Testing and data gathering procedures.

6.4.1. Preliminaries

Mounting

Two die were selected: one including examples of beam A, the other of beam B. These die, once bonded to copper disks, were then attached with wax resin to the upper steel disk of the piezo-vibrator. The piezo-vibrator was then screwed into the centre of the test chamber. This left a minimum gap of 5mm between the beam resonators and the glass window. Once mounted in place, the piezo-vibrator and devices remained there for the entire duration of the subsequent experiments to minimise any changes to either beam boundary conditions or piezo-vibrator response. Beams D3 (beam A type) and E4 (beam B type), as shown in figure 6.14, were selected as the beams for all subsequent experiments.



Figure 6.14: Dies and beams selected for experiments

Levelling

Before any vibratory measurements could be taken, it was necessary to adjust the staging so that the vibrometer laser beam would focus onto the beam surface at a normal to it. With the chamber open, the 10X Mirau objective, Zygo surface profiler and monitor were used together to illuminate the silicon beams. By adjusting the staging incrementally, devices could be positioned appropriately by looking to maximise the width of interference fringes.

Introduce gas

Where measurements were to be taken in argon, helium or carbon dioxide, the sealed chamber was first evacuated using the vacuum pump before opening the gas inlet valve and a regulator at the gas tank. Both inlet valve and regulator were left open to maintain pressure of gas in the chamber above atmospheric.

For measurements in air, the chamber was again evacuated, then a gas inlet opened to let air from the atmosphere fill the chamber up to atmospheric pressure. The gas inlet was then sealed.

Set temperature

The effect of temperature on measurements was anticipated to be of interest. To create temperature regimes above room temperature, the peltiers were operated in reverse at a range of voltages. Once an operating voltage had been set and the peltiers switched on, the apparatus was left in this state for at least one hour. This gave the apparatus a period of time in which the internal gas, devices and piezo-vibrator could reach something approaching a constant temperature. Throughout this period, gas pressures were monitored and kept stable.

Power for the pressure transducer and peltier plates was provided by a Farnell E30-2BT Dual 30V 2A DC Power Supply.

6.4.2. Static measurements

Static measurements were performed using the Zygo surface profiler with the 10X Mirau objective and Metro Pro software.

Beam dimensions

The ability to measure beam dimensions accurately was limited by the experimental setup. It was not possible to measure beam depth with the arrangement, and so it had to be assumed to be within the stated manufactured limit of $15 \pm 1 \mu\text{m}$. For beam width and length, it was necessary to adopt the following procedure due to a lack of calibration between the Zygo surface profiler and Metro Pro software. The X staging was adjusted so as to set a reference point with the software at a home position at one corner of the beam under consideration. The X staging, calibrated with the Metro Pro software, was then adjusted to place another reference point at another corner of the beam. Doing so allowed the beam width and/or length to be extracted from the Metro Pro data. In this process it was necessary to remove the chamber lid, exposing the beams and piezo-vibrator to the surrounding air. Although measurements could be performed rapidly, there was an inevitable effect on temperature in the vicinity of the beams.

Surface profile

Stress in the silicon wafer, both intrinsic and as a consequence of the fabrication and mounting steps, will tend to bow the substrate. Although the extent of the resulting beam deformation could not be accurately determined due to calibration issues, it was still possible to check for the existence of bowing using the surface profiler. Figure 6.15 shows an example of an uncalibrated surface profile scan on beam E4, and confirms that bowing was present.

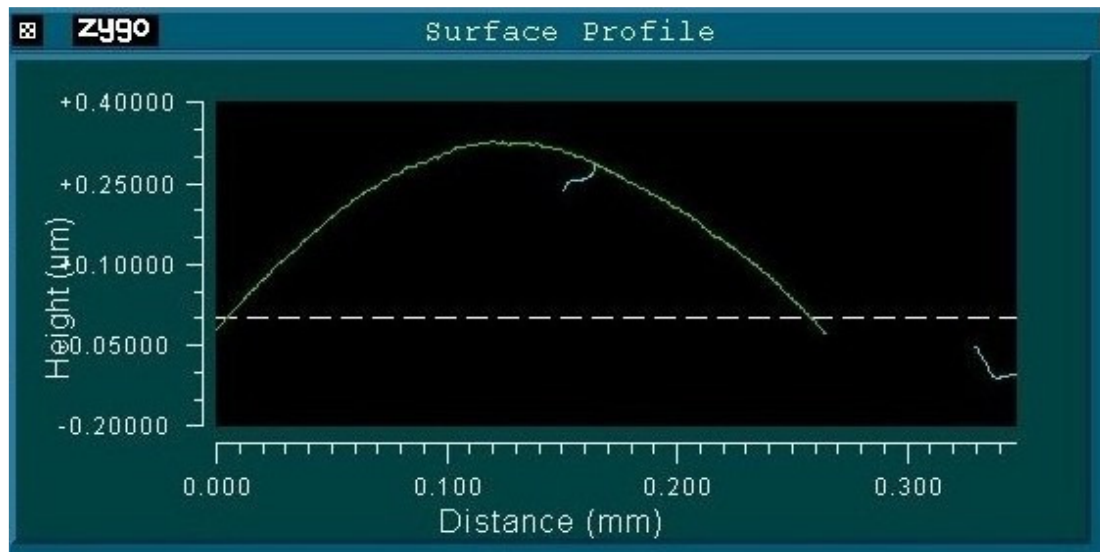


Figure 6.15: Surface profile of beam E4 at 22.7°C

6.4.3. Vibratory measurements

Vibratory measurements were carried out over a range of temperatures and applied actuation voltages in each gas, using the laser vibrometer with the optical head fitted to the Zygo surface profiler. A description of the procedure followed is now outlined:

Analyser and vibrometer settings

For actuation purposes, the signal voltage and frequency range were set on the signal analyser. For certain measurements, the actuation voltage was amplified using a TEGAM Model 2350 high voltage amplifier to achieve voltages up to 40V. The actuation signal was set to Swept Sine to provide a sweep of actuation frequency across the frequency range. Power spectrum measurements were selected to provide the absolute magnitude of beam displacements. The velocity range was set on the vibrometer controller to maximise the resolution of the displacement amplitude.

Laser focusing

The incident laser beam was focused either onto the beam centre for beam displacement measurements, or slightly off the beam for measurements of the applied background displacement. This is illustrated in figure 6.16: background measurements were taken from positions close to either point A or B to avoid any areas of unconstrained silicon, due to either undercut or bonding issues, whereas the beam displacement was measured close to point C to maximise the amplitude measured in the first vibration mode. It was not possible to record and thus replicate the true position of measurements with the experimental setup. However, this did not appear to be of consequence for background measurements. Nor was it of particular importance to beam displacement measurements, where it is the frequencies at which jump points or the resonant peak occur which are of most interest.

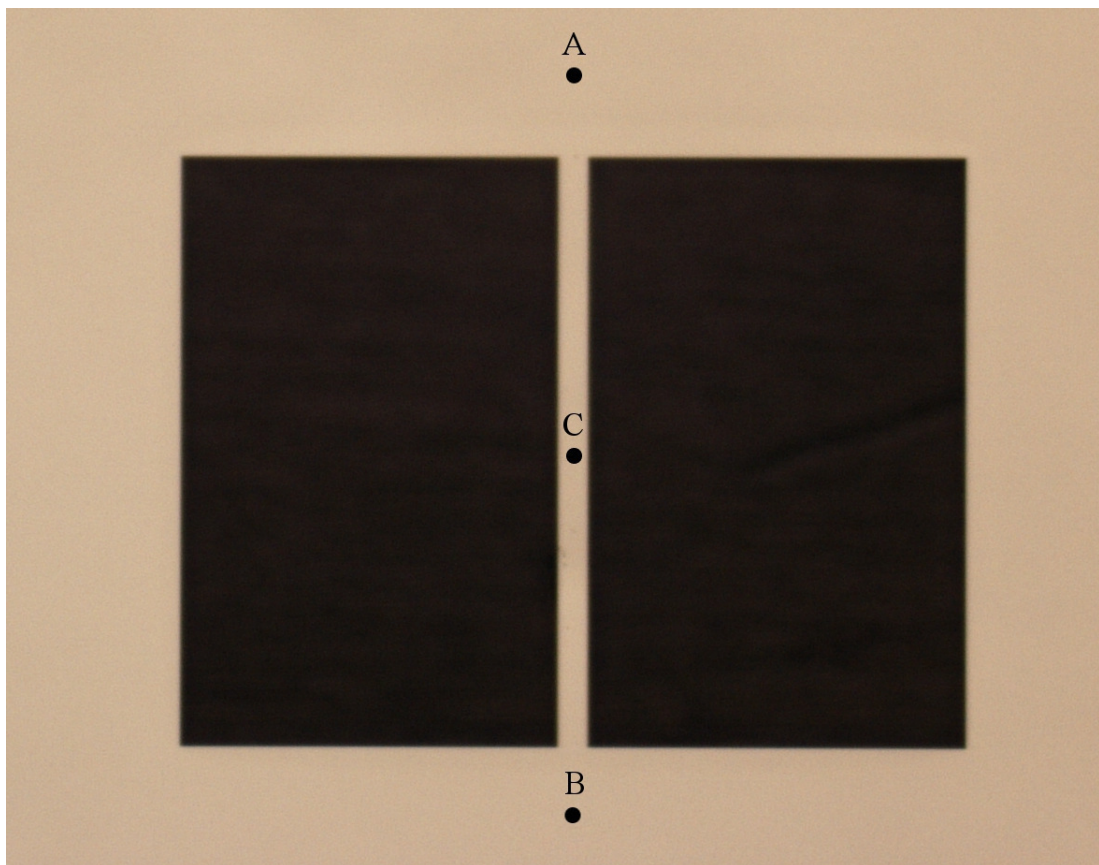


Figure 6.16: Focusing positions of incident laser on silicon device

Performing measurements and collecting data

Swept Sine measurements were found to take approximately three minutes to sweep through the chosen frequency range, gathering 800 data points in doing so. For linear measurements, one sweep was performed to measure the beam frequency response, another to measure the background displacement, taking around six minutes in total to collect the complete data set. For nonlinear measurements it was necessary to perform two sweeps across the frequency range to measure beam response: one sweep beginning at the lowest frequency and increasing across the range, the other beginning at the highest frequency and decreasing. With another sweep measuring the background displacement, nonlinear measurements took around nine minutes.

In the time taken to gather a complete data set, it was possible for there to be a certain degree of temperature or pressure change within the chamber. This introduces two particular uncertainties to measurements: the measured background cannot be guaranteed to exactly reflect the background present when the beam displacement is measured; for nonlinear measurements, jump points may move between the up and the down sweep. The consequence of this, with regard to the validity of data and the use of error bars, is discussed in chapter 7, sections 7.1.2 and 7.2.1.

For background displacement data gathered in this fashion, the measurements obtained provide the true amplitude of actuation. For beam displacement measurements however, what is actually measured is the sum of the beam displacement plus the background displacement. This is not an issue, since, as mentioned above, it is the frequency of jump points or resonance peaks that is of interest. This is discussed in section 7.1.4, where it is shown that background amplitude may be considered negligible when compared to the beam displacement.

Measurement data recorded on the signal analyser was copied to an external hard drive after each sweep had been performed. The data could be converted at a later time into suitable files to allow data analysis.

6.5. References

1. Zygo NewView 5000 Brochure, Zygo Corporation, 2001.
2. Laser Vibrometer User Manual, *Polytec Vibrometer Series OFV 300 / OFV 501*
3. 3562A Dynamic Signal Analyser Operating Manual, Hewlett Packard, 1985.

Chapter 7

Experimental results for fabricated devices

In this chapter the most pertinent experimental results for the two beams considered are presented. Across all of the gathered data, the maximum background displacement h achieved is found to be 38.8nm. As discussed in section 4.3, the system can be considered weakly nonlinear where $d \gg h$. d is approximately equal for both beams at 15 μ m. Therefore the minimum d to h ratio is given by $\frac{15E-6}{38.8E-9} \approx 387$. This suggests that the system does indeed remain weakly nonlinear throughout these experiments. In addition, Mach numbers were seen to remain below 0.01 for all gases at atmospheric pressure or above, and for all bar the most extreme cases of air at low pressure, ensuring that the gases may reasonably be considered incompressible.

7.1. Overview

7.1.1. Actuation

The amplitude h of the actuation, which is subsequently referred to as the background displacement, is known to vary with the voltage applied to the piezo disk. Figure 7.1 shows the frequency response of the background for beam A at two different voltages. The data was gathered at low pressure (below 0.017 bar – see table 7.2 in section 7.4.3), with temperature varying from 28.9 to 29.1°C.

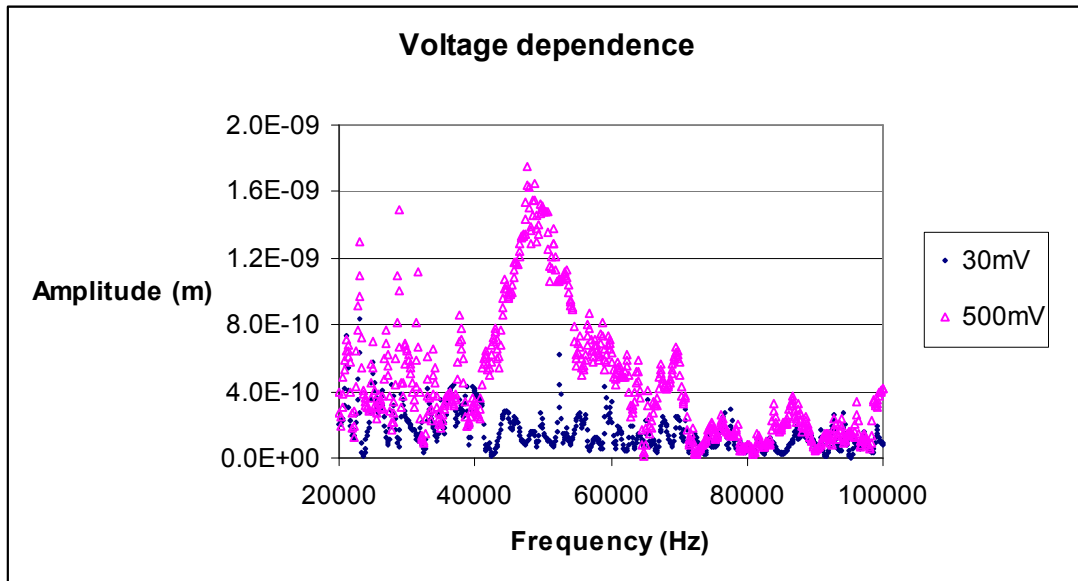


Figure 7.1: Background displacement for beam A at two differing voltages: 30mV and 500mV

It is apparent that applied voltage makes a significant difference to the background displacement. In addition, as the voltage is increased from 30mV to 500mV, so the frequency dependent behaviour of the actuator becomes noticeable. As the voltage is increased, this effect is seen to become more pronounced and highly influential.

For an appreciation of how the surrounding gas might affect the background, measurements were taken for beam A in air and helium at 26.35 °C. The applied voltage was 20V in each case. Figure 7.2 is inconclusive but suggests that the background is damped further in air, as might be expected.

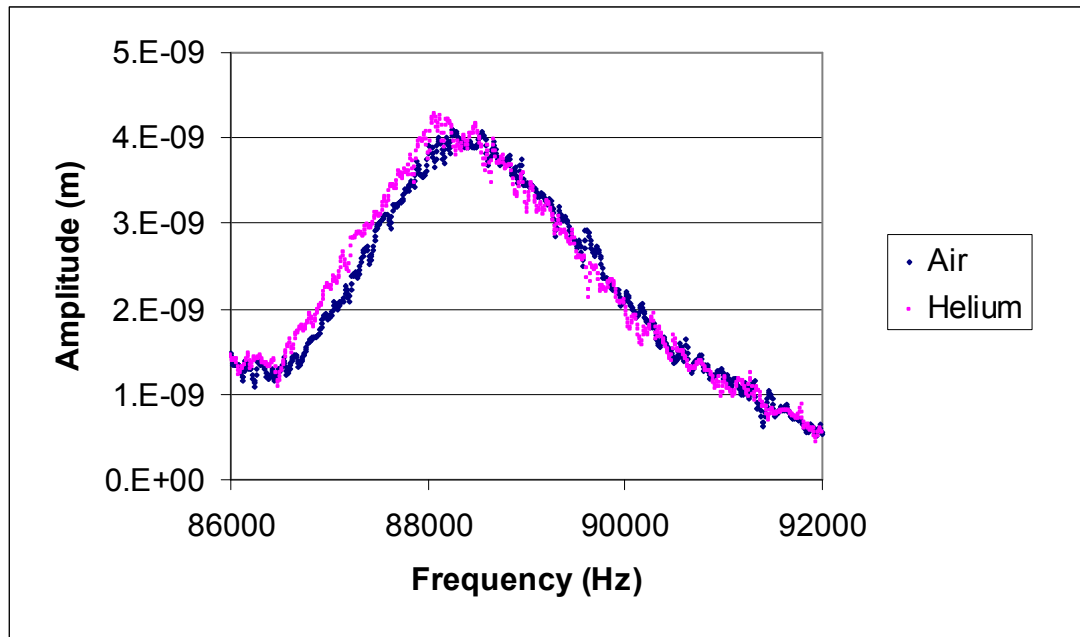


Figure 7.2: Effect of surrounding gas on background displacement, with an applied voltage of 20V

7.1.2. Typical frequency response data

The frequency response of the beams was investigated by applying a swept sine voltage to the piezo disk, and sweeping over an appropriate frequency range. In the case of linear vibrations, it was necessary only to sweep in one direction. For the nonlinear regime, a sweep up and a sweep down were necessary in order to obtain both jump points. For each set of these frequency response measurements, the frequency-dependent behaviour of the background displacement was also recorded.

Figure 7.3a presents the frequency response of beam A in argon, operated within the linear regime. Figure 7.3b shows the associated background displacement. Similarly, figure 7.4 shows equivalent data at a higher voltage level. Jump points are clearly seen to occur, although the accuracy to which their frequency can be stated is dependent on the resolution of the analyser. The separation δF is subsequently taken to be that illustrated in figure 7.4a: the separation between the points showing first clear evidence of a jump occurring in each direction of sweeping.

It is apparent from figures 7.3(b) and 7.4(b) that the amplitude of the background displacement in the region of the resonant frequency cannot be considered single

valued. This is a diversion then from the modelling approach taken in chapter 4, and proves to be of significance (see section 7.2.1).

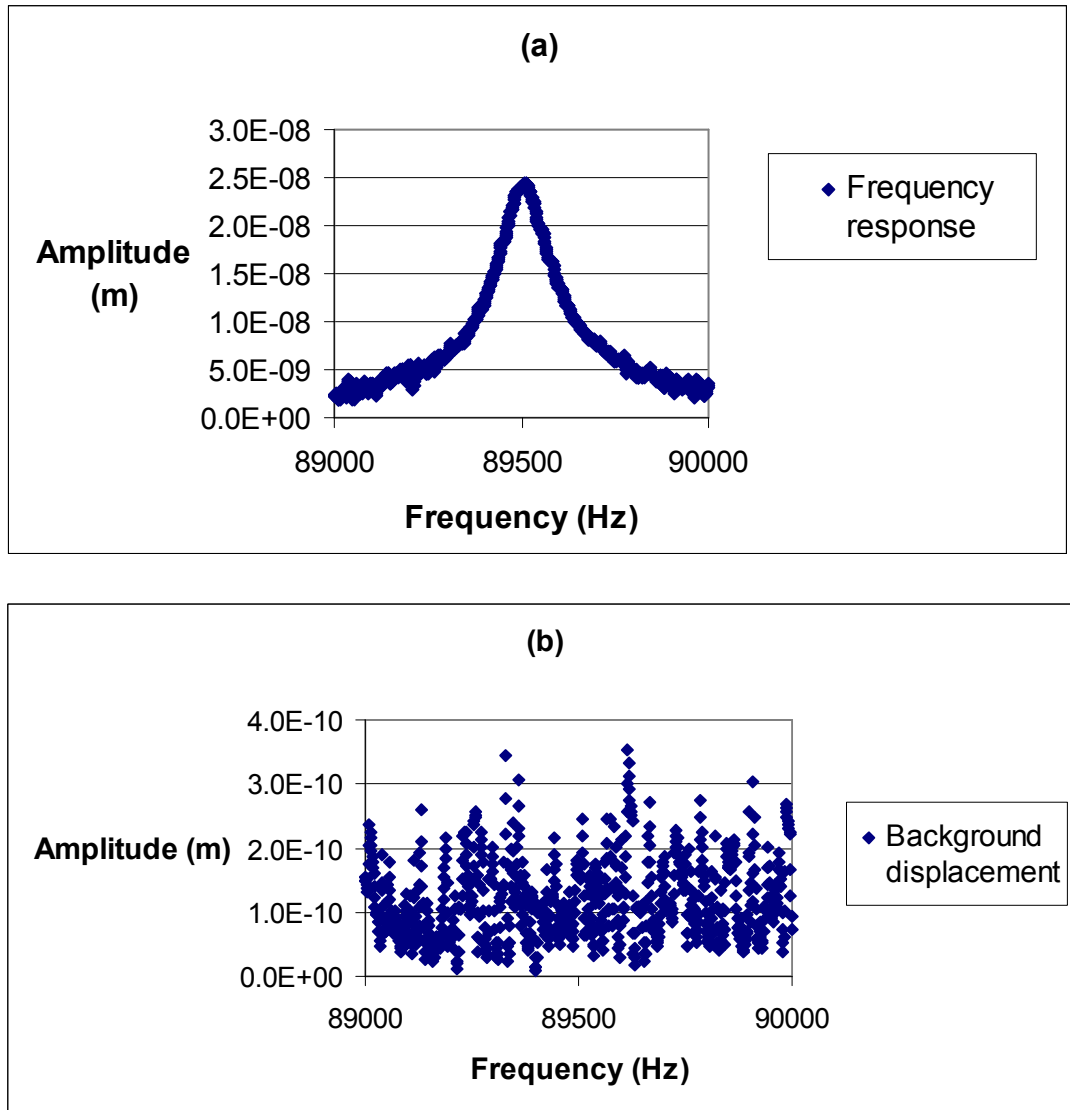


Figure 7.3: Frequency response (a) and background (b) for beam A in argon, operated within linear regime with applied voltage 50mV

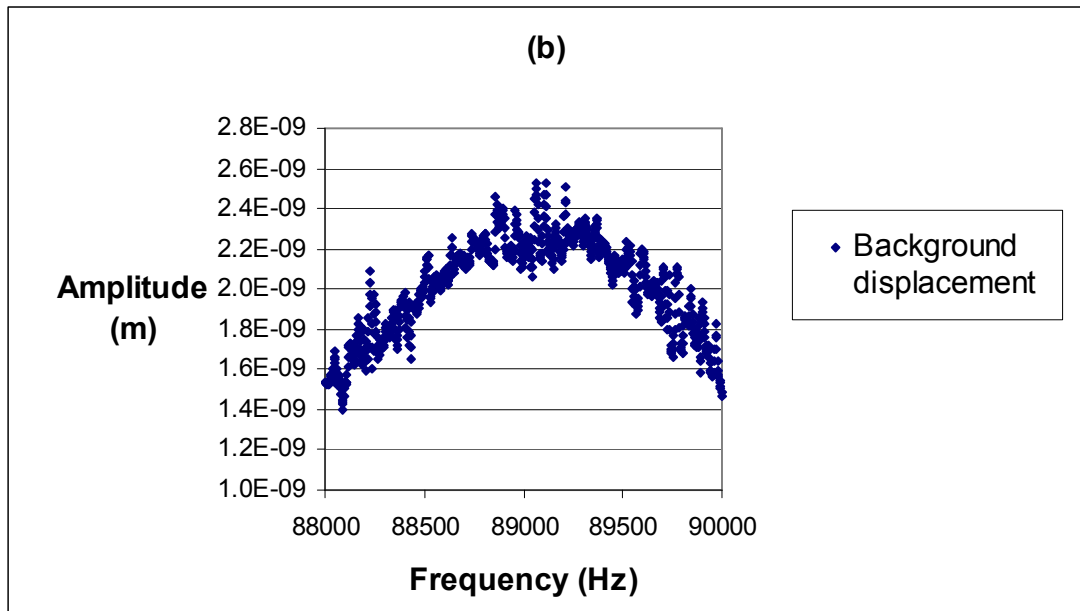
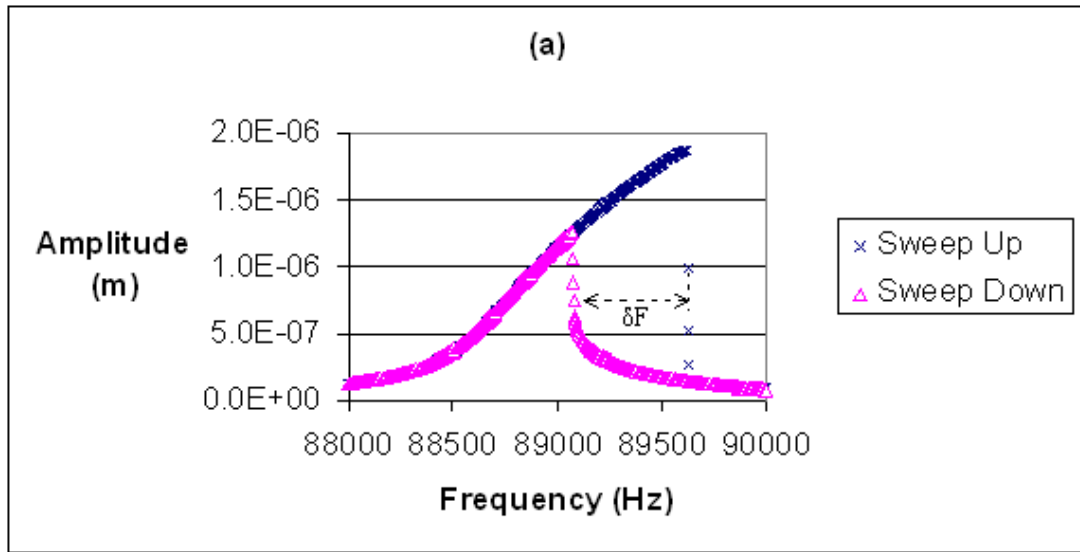


Figure 7.4: Frequency response (a) and background (b) for beam A in argon, operated in nonlinear regime with applied voltage 5V

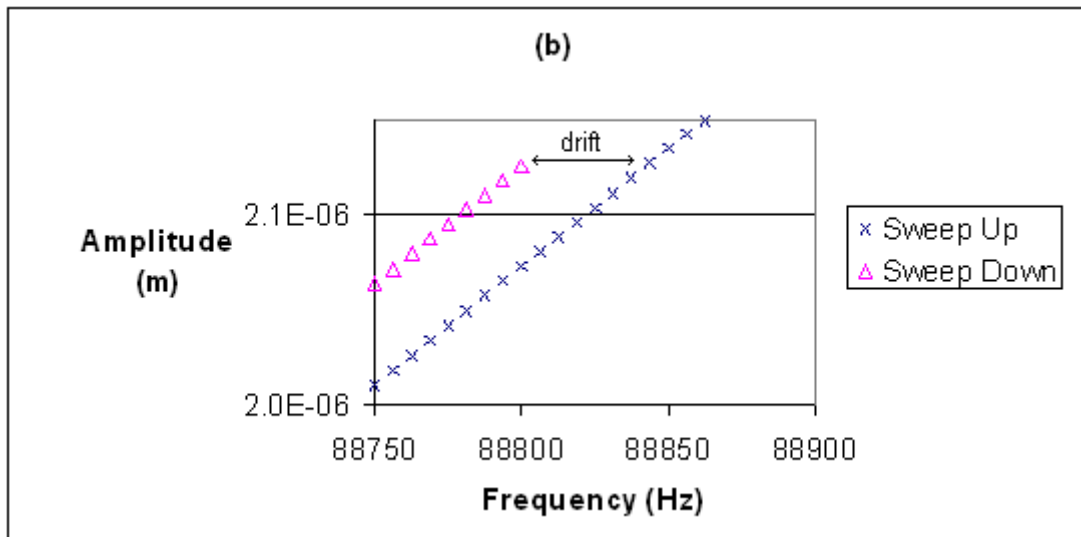
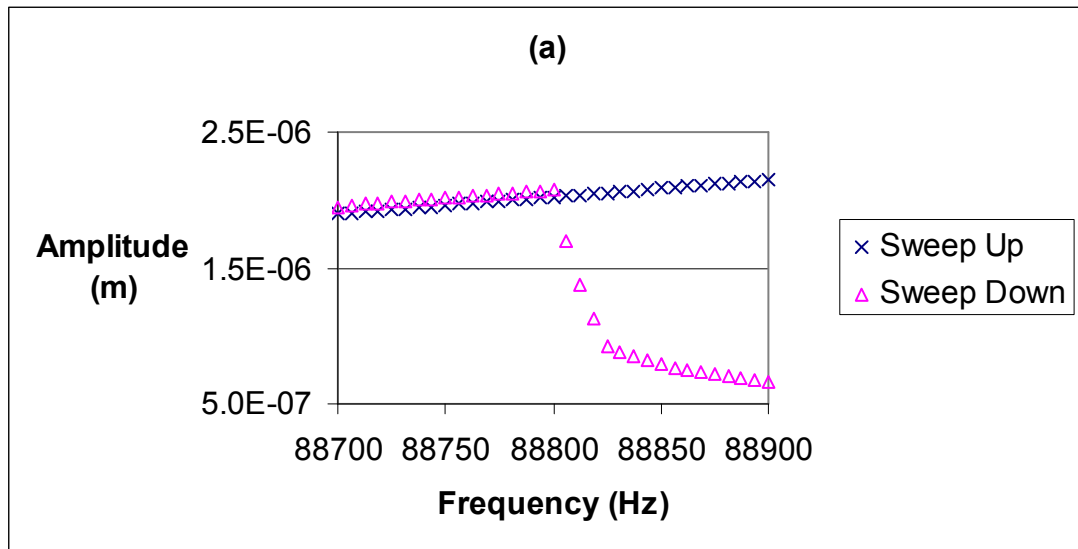


Figure 7.5: Drift in δF

It was noted with some of the gathered data that, between performing an upward frequency sweep and a downward frequency sweep, there could be a slight change in the beam response. This is possibly a result of temperature changes. As a consequence, the up and down sweep data could not be exactly superimposed, resulting in the discrepancy labelled 'drift' in figure 7.5 (b). The frequency value of this drift parameter had to be either added or subtracted from the apparent δF in some cases, to provide a more representative δF . This correction makes it very difficult to include meaningful error bars on plotted δF data.

7.1.3. Nonlinear response data

Measurements of δF were taken for both beams in a range of gases, at various temperatures and applied voltage levels. The most appropriate way to present the results was deemed to be to plot δF against some average value of the background displacement. The decision was taken to use the mean of the background displacement over the range from the lower to upper jump points. This mean is subsequently referred to as \bar{h} .

Figures 7.6 and 7.7 show the results for beams A and B respectively. In the case of beam A, there is a clear indication that measurements of δF may be sufficient to identify certain gases. There is some indication of the same for beam B, although there appears more crossover between the data for each gas. For both beams though, differentiating between air and carbon dioxide would initially appear problematic.

It is important to note that plotting δF against \bar{h} can result in the appearance of apparently spurious data. This is examined in detail in section 8.2.2, where the effect of the background profile is taken into consideration.

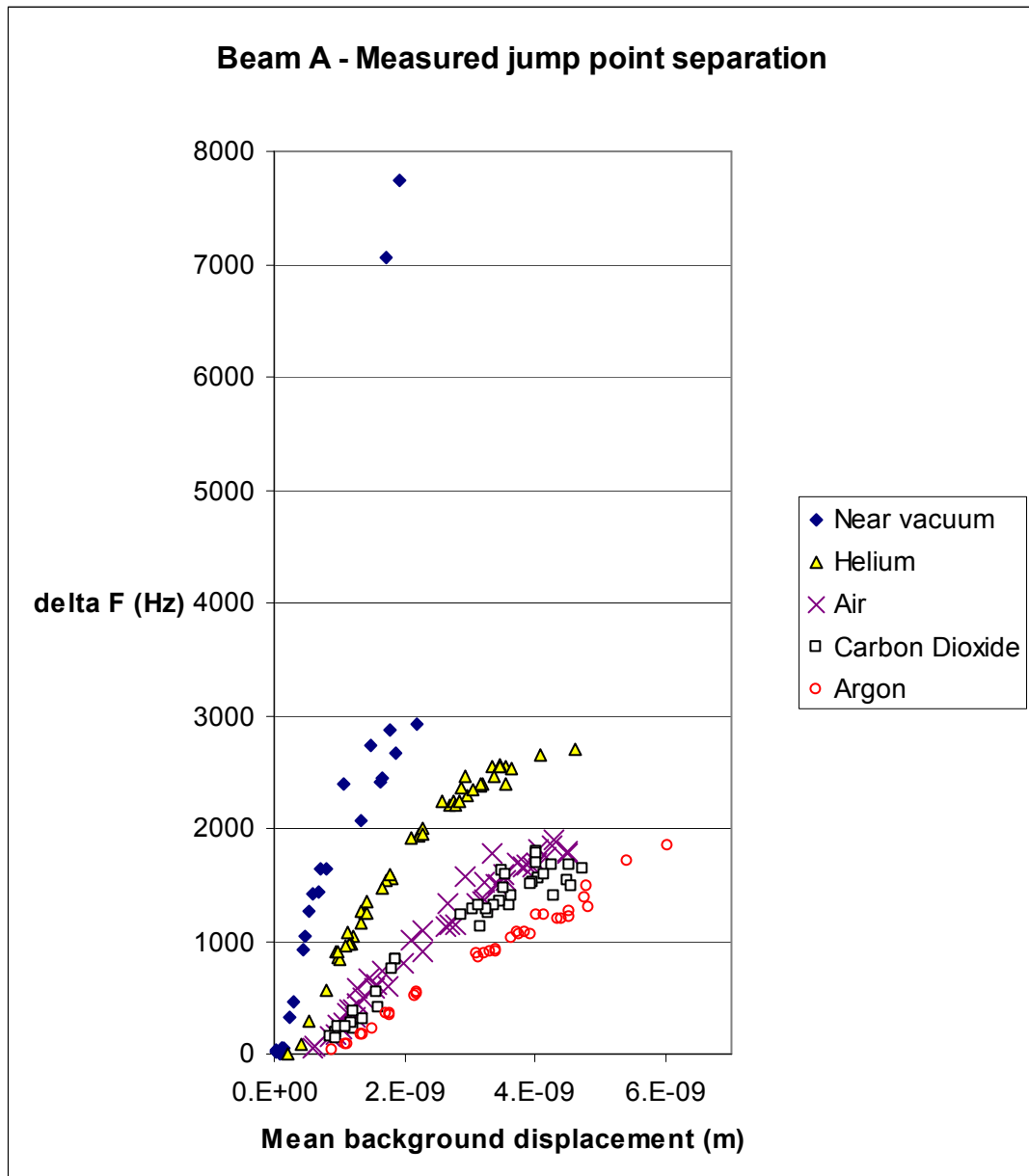


Figure 7.6: δF versus \bar{h} for beam A

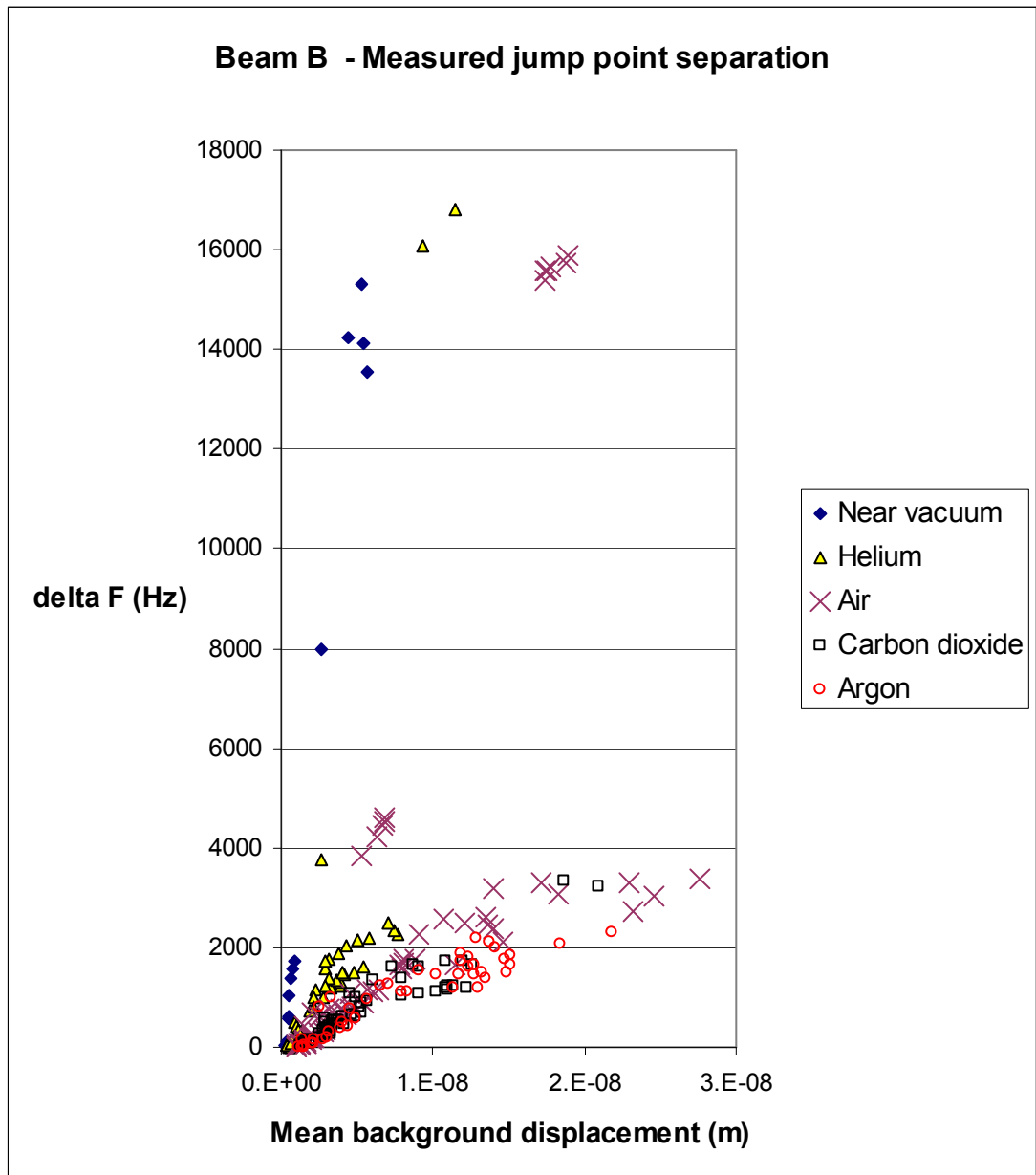


Figure 7.7: δF versus \bar{h} for beam B

In chapter 1 it was stated that existing sensors employ bandwidth measurements in identifying fluid properties (see sections 1.2 and 1.4.1). In this research the interest is in identifying any advantage in using measurements of δF instead. Figure 7.8 presents measurements of the two obtained for beam A in helium.

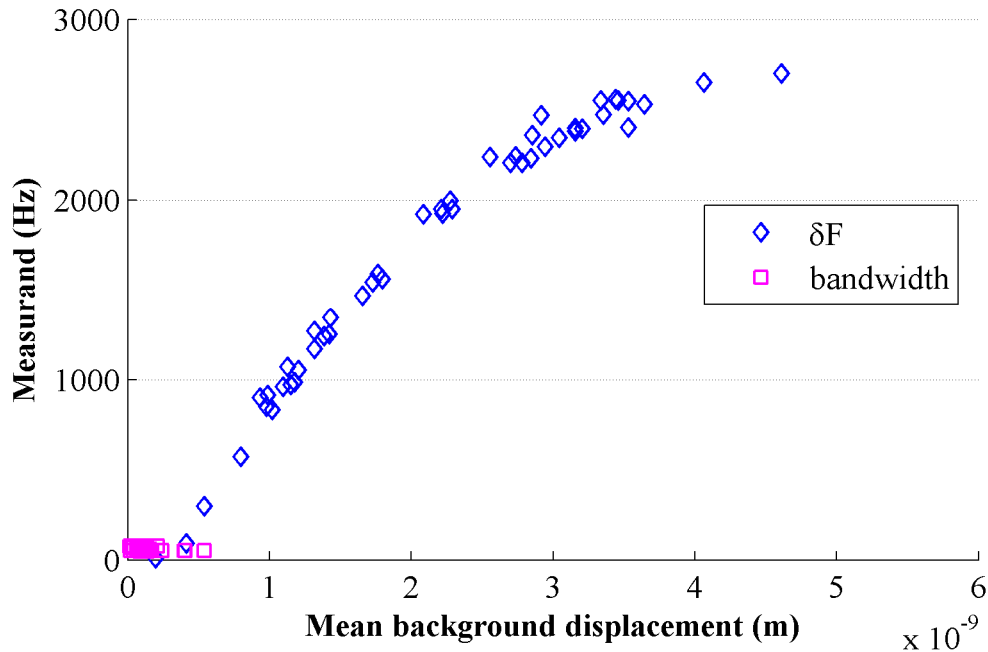


Figure 7.8: Linear bandwidth and nonlinear δF measurements for beam A in helium

It is clear that δF can be made far greater than bandwidth for the given beam. This is of interest, but does not in itself indicate greater accuracy or sensitivity in identifying a gas, or distinguishing between two similar gases. This is discussed further in section 8.4.

7.1.4. Amplitude of vibration

As discussed in section 6.4.3, the amplitude of vibration at the centre of the beam cannot be directly measured, nor can the phase relationship between the background and this vibration. However, for later modelling purposes, a reasonable approximation of amplitude is required. In order to gain an impression of the contribution of the background (a) to the measured vibration amplitude (b), the ratio of the (b) to (a) amplitudes was briefly examined. Figure 7.9 illustrates one of the measurements for beam B in argon, chosen as this minimises this ratio. For this data, the minimum ratio (b)/(a) is approximately 11, maximum 91. This suggests that, for

the purposes of this work, the background contribution may be neglected when considering the measured vibration amplitude.

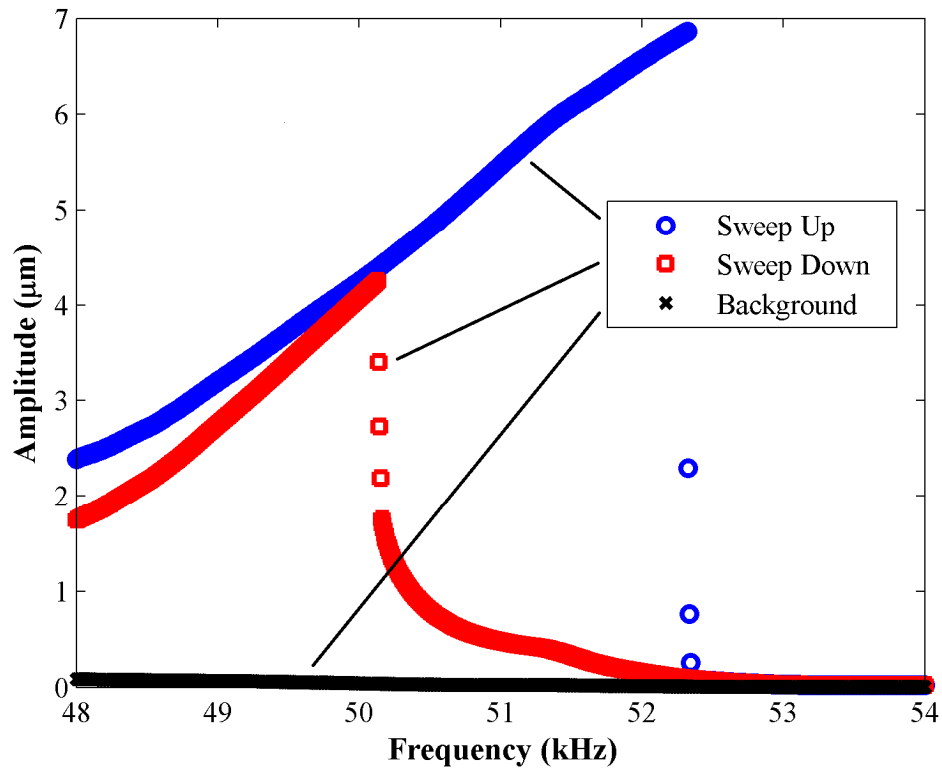


Figure 7.9: Beam B in argon, with applied actuation voltage at 40V

7.2. Temperature effects

Measurements were taken over a temperature range of 19.7 to 33.3 °C. The effect of temperature on the background, boundary conditions and beam dimensions is investigated below.

7.2.1. Background stability

The background displacement for both beam A and beam B was measured at two temperatures in a near vacuum, at low pressure with actuation voltage set at 500mV. As each beam is mounted on a separate copper disk, it is necessary to measure the background for each beam separately. Figure 7.10 displays the measurements for beam A, figure 7.11 those for beam B.

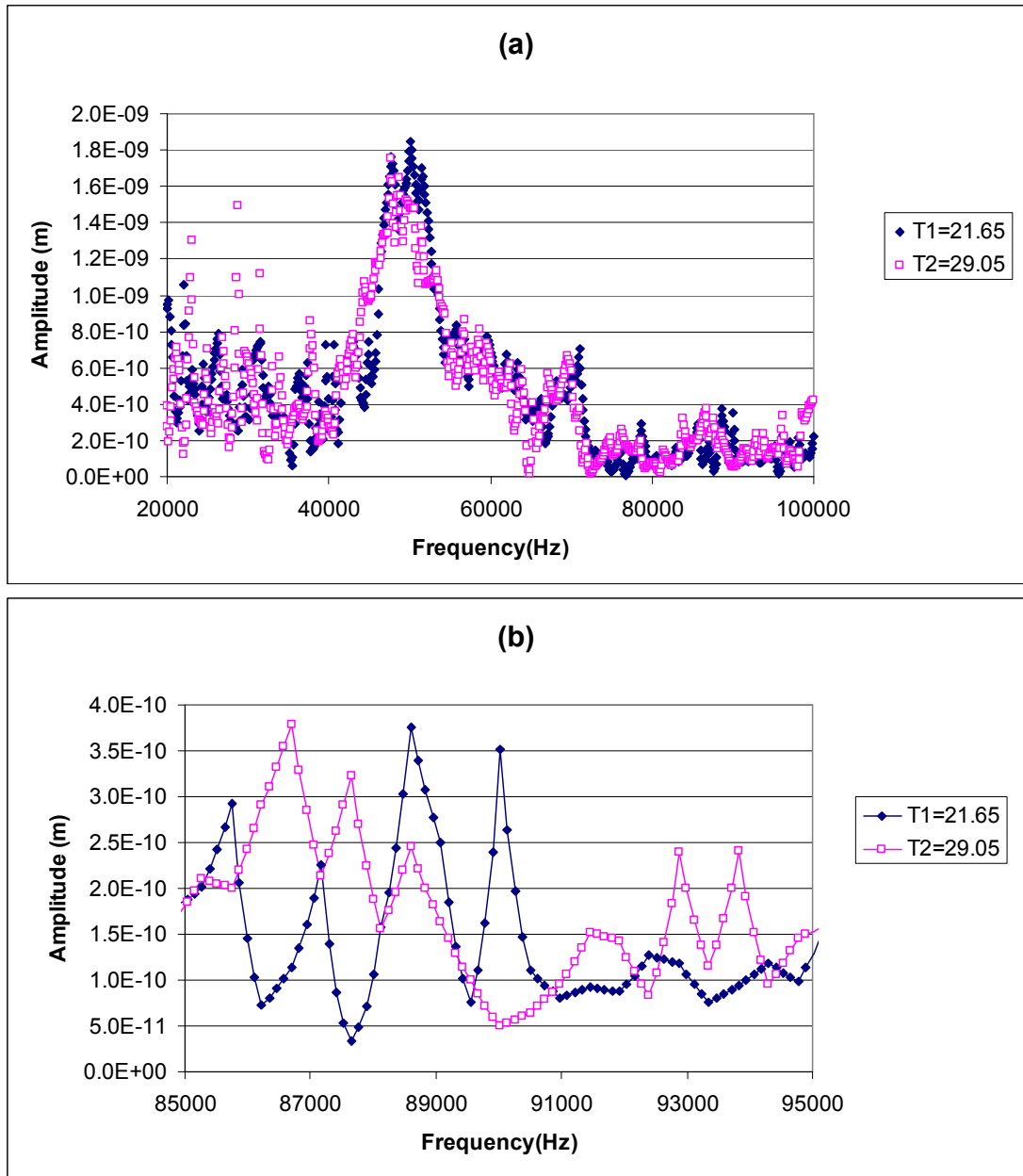


Figure 7.10: Temperature dependent background displacement for beam A in a near vacuum at 500mV. Lower temperature 21.65 °C, upper temperature 29.05°C

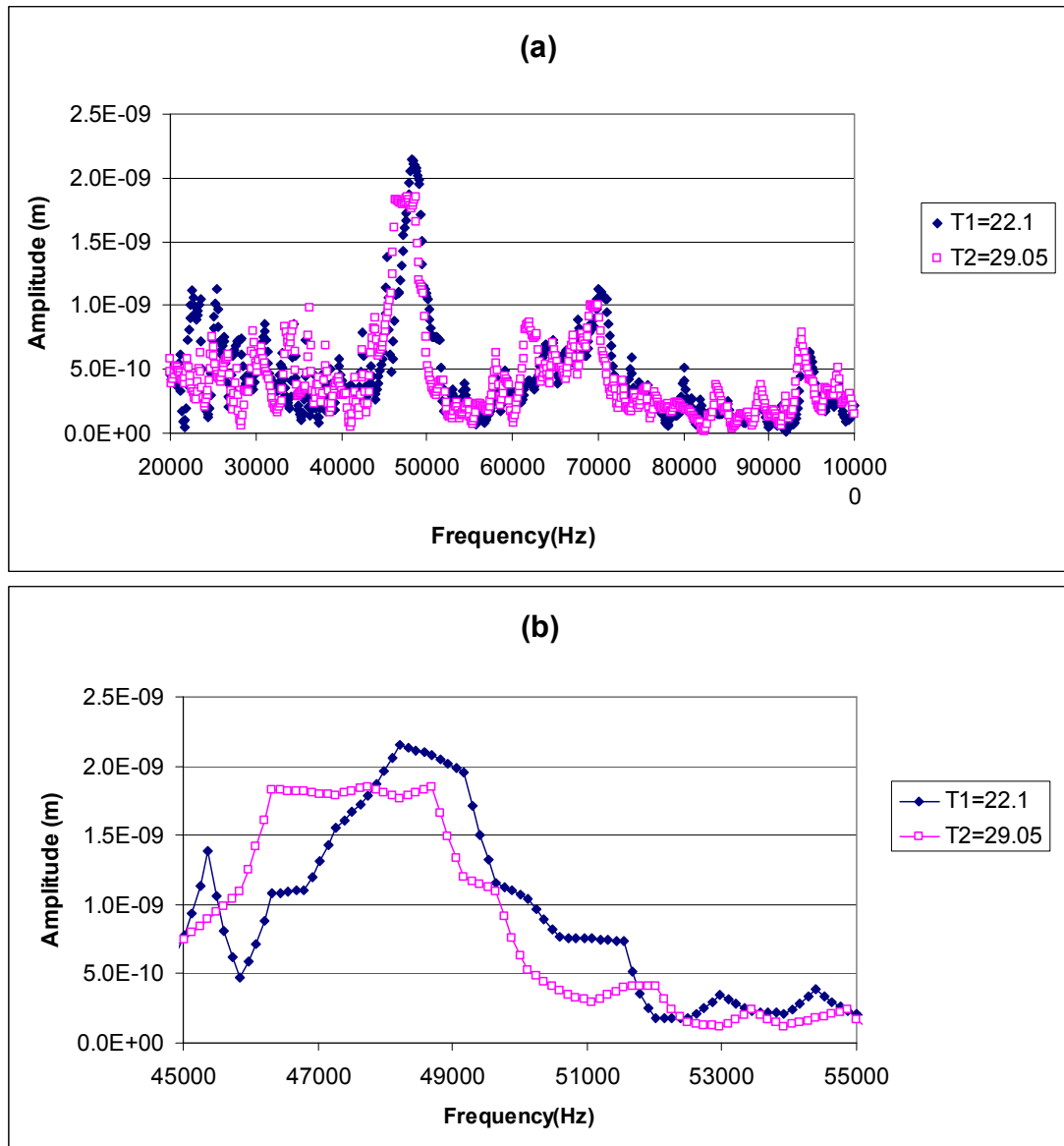


Figure 7.11: Temperature dependent background displacement for beam B in a near vacuum at 500mV. Lower temperature 22.1°C , upper temperature 29.05°C

Figures 7.10(a) and 7.11(a) indicate that the frequency response profile of both backgrounds moves down in frequency as temperature is increased over the given ranges. Figures 7.10(b) and 7.11(b) focus on the effect on the backgrounds in the region of the pertinent beam's fundamental resonant frequency. It is apparent that temperature can have a significant effect on the background, such that the background must be measured separately for each linear or nonlinear measurement. It is not sufficient to assume a consistent background displacement for a given applied voltage.

To investigate the stability of the background further, it is appropriate to use higher voltages in order to maximise readings and any differences between them. Consider the following cases:

Case 1 – repeatability of measurements

The background displacement was measured under near identical conditions on different days, to evaluate the repeatability of measurements. Figure 7.12 shows a typical example of such a reading, for beam A in air, with an applied voltage of 25V and a mean temperature of 29.2 °C. Very little difference can be observed in the backgrounds, and this is found to be consistently true for both beams, regardless of the voltage, gas or temperatures under consideration. Measurements may then be considered repeatable to a reasonable degree of accuracy.

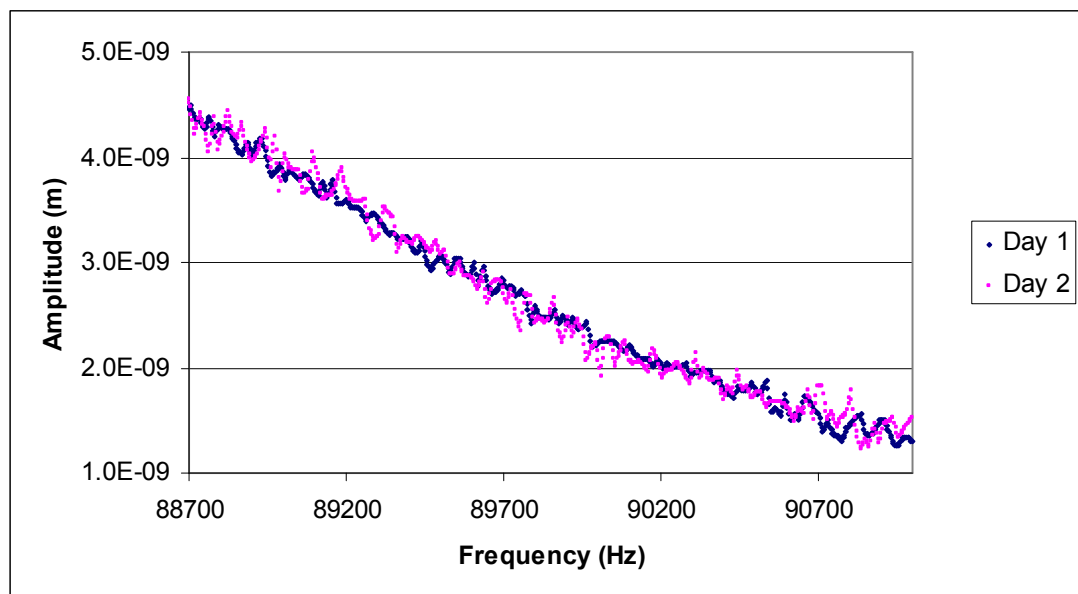


Figure 7.12: Backgrounds for beam A on separate days

Case 2 – effect of moderate temperature changes

There were found to be drifts in temperature over the course of obtaining a linear or nonlinear data set. A typical drift is of no more than 0.3 °C, although this is exceeded on rare occasion. It is necessary therefore to examine the effect of moderate temperature changes on backgrounds, in order to confirm whether or not a background may reasonably be associated with the preceding or subsequent beam vibration measurements (see section 6.4.3 for further discussion). Figures 7.13, 7.14 and 7.15 illustrate the effect of temperature drifts in the region of 0.3, 0.45 and 0.7 °C respectively.

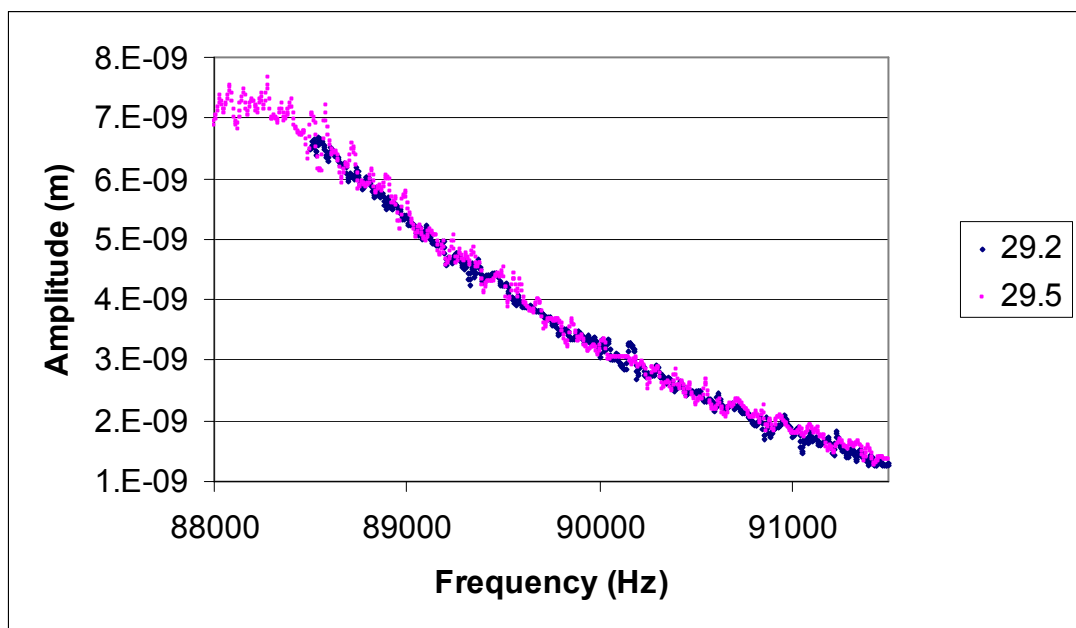


Figure 7.13: Beam A backgrounds in air. Applied voltage 35V. Temperature shift 29.2 to 29.5 °C

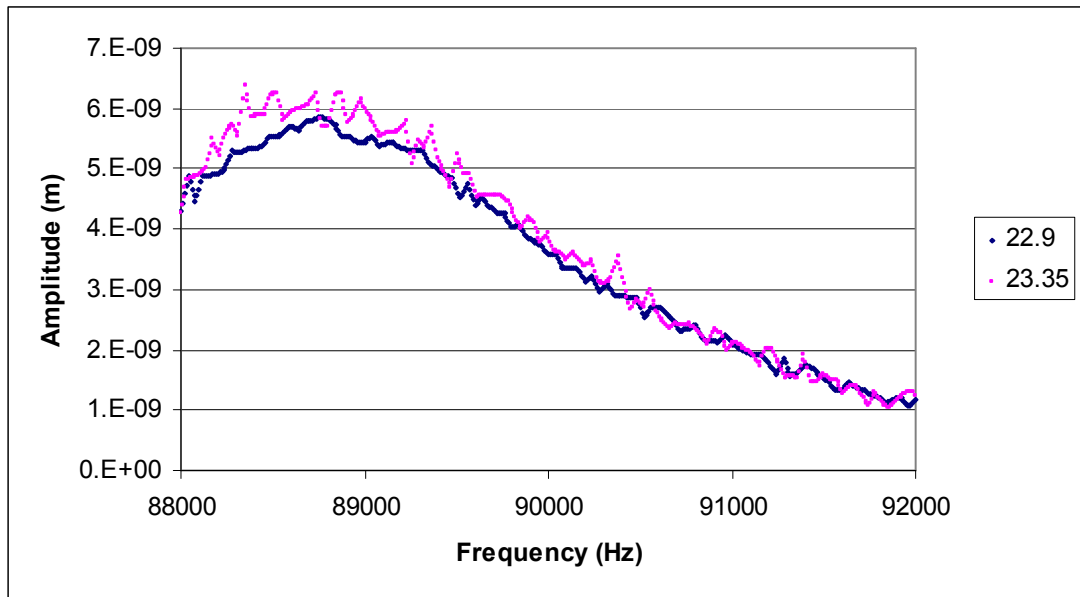


Figure 7.14: Beam A backgrounds in helium. Applied voltage 30V. Temperature shift 22.9 to 23.35 °C

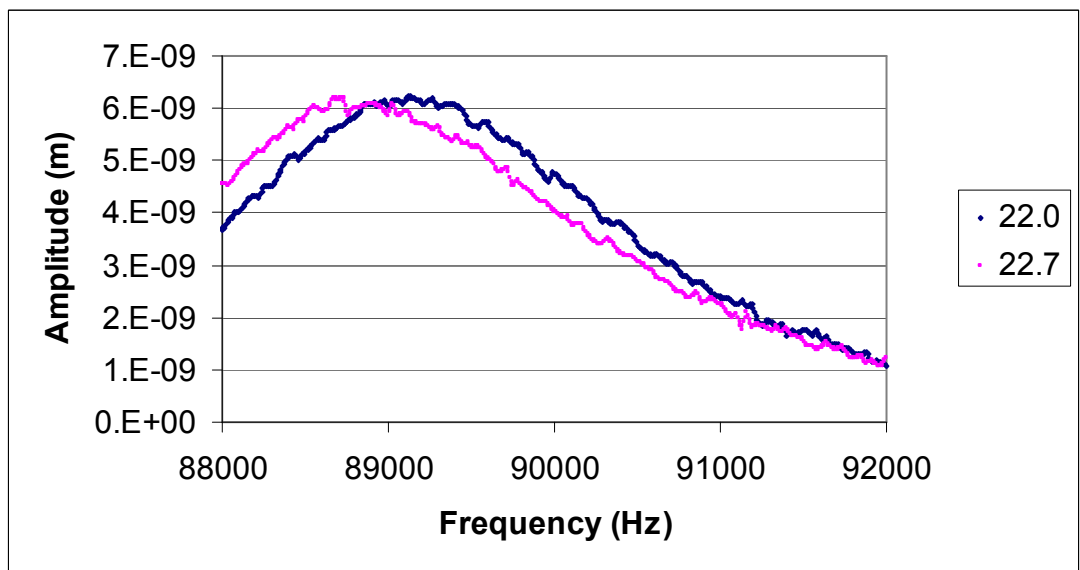


Figure 7.15: Beam A backgrounds in air. Applied voltage 30V. Temperature shift 22.0 to 22.7 °C

For a drift of 0.3 °C, it is difficult to detect any difference between the backgrounds over the frequency range of concern. As the size of drift increases, so the backgrounds begin to become distinct. For the drift of 0.7 °C, the distinction is clear. This trend is found to be true for both beam A and B at these higher voltages.

Summary

In summary, the background displacement is shown to be repeatable where conditions remain identical. Changes in temperature cause shifts in the background, but these shifts may be negligible where the temperature change is of the order of 0.3°C or less. This suggests that it is justifiable to associate background readings with linear or nonlinear data sets, as the temperature is unlikely to shift significantly in this time.

7.2.2. Boundary conditions

As discussed in section 6.2.4, temperature-induced changes in boundary conditions can alter the tension in a beam, affecting the resonant frequency. Figure 7.16 shows how the resonant frequencies of beams A and B behave with temperature. The linear data for all gases and all applied voltages is plotted.

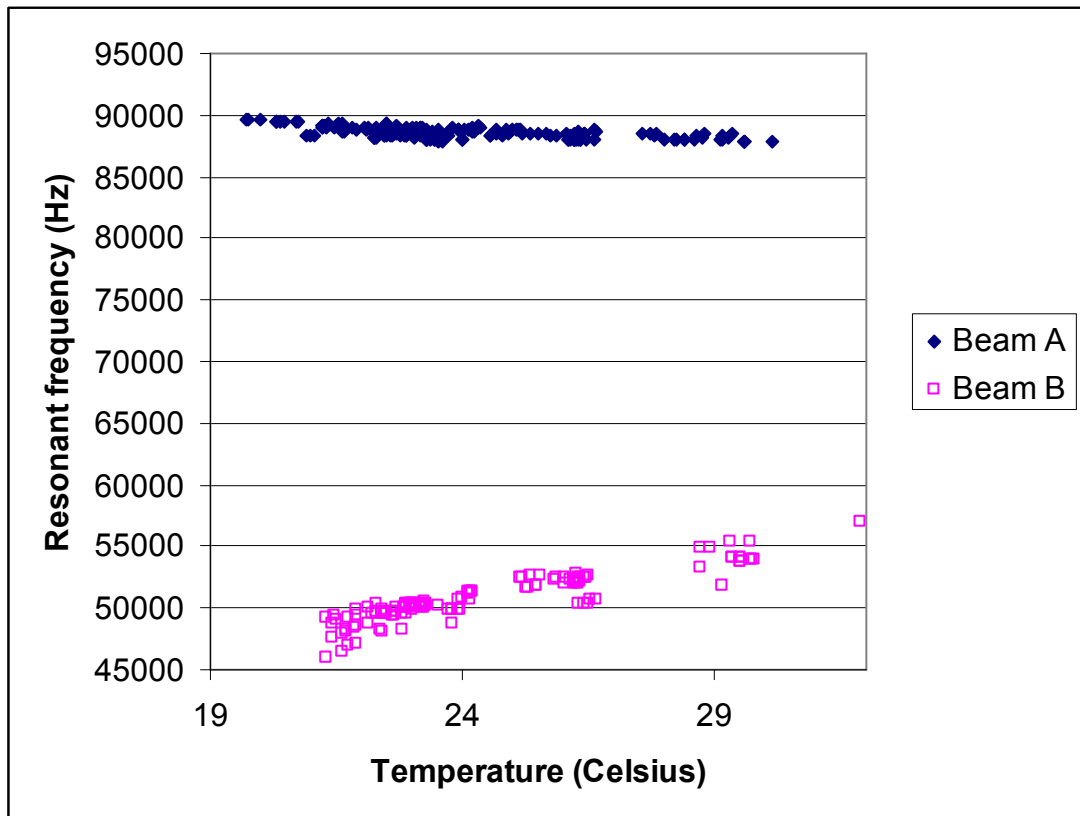


Figure 7.16: Resonant frequency dependence on temperature

The resonant frequency for both beams is seen to change with temperature. The trend for either beam though differs. The resonant frequency tends to decrease with temperature for beam A, yet increase with temperature for beam B. This discrepancy suggests that the change is dominated by the unknown boundary conditions, rather than changes in fluid or beam properties. This is examined further in section 8.3.1.

7.2.3. Beam dimensions

The dimensions of both beams were determined at varying temperatures, as described in section 6.4.2. The measurements, subject to the inherent uncertainties, are given in table 7.1. This data appears to show inconsistent behaviour with temperature. It is therefore assumed that this measurement technique is not sufficiently accurate to be reliable. The consequences of temperature-induced changes to beam dimensions are discussed further in section 8.1.3.

Beam	Temp. (°C)	L (µm)	B (µm)
A	21.4	1197.50	32.89
A	28.25 ± 2.25	1202.35	31.06
B	21.3	1498.63	76.90
B	30.5 ± 2.25	1498.16	76.92

Table 7.1: Beam dimensions

7.3. Beam comparison

It is useful to appreciate the relative performance of beams A and B in various gases. For this purpose, δF is plotted against the mean background displacement for both beams, by gas. Figures 7.17 to 7.21 show the results.

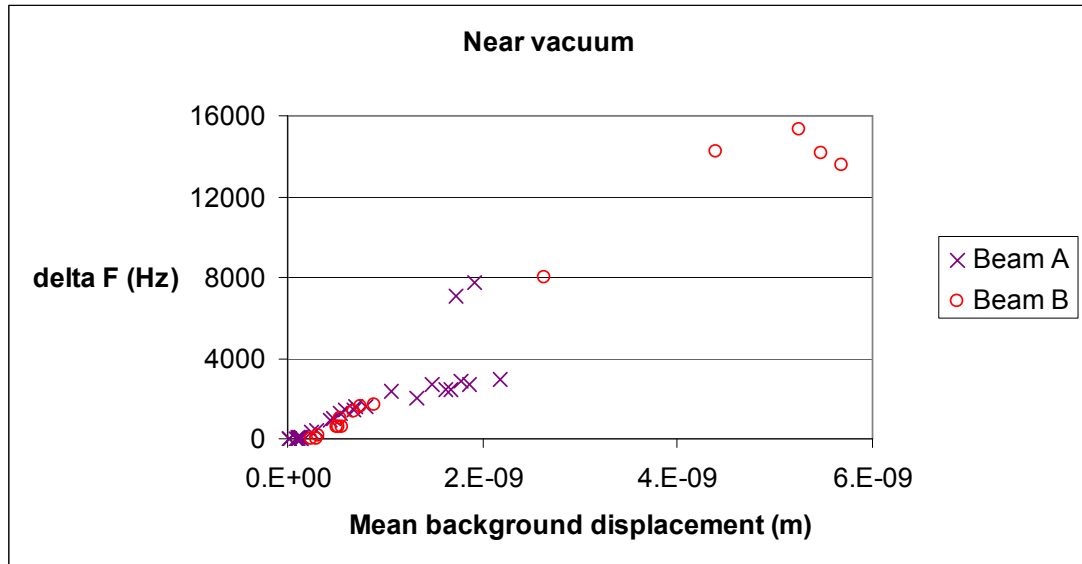


Figure 7.17: δF for beams A and B at low pressure, in a near vacuum

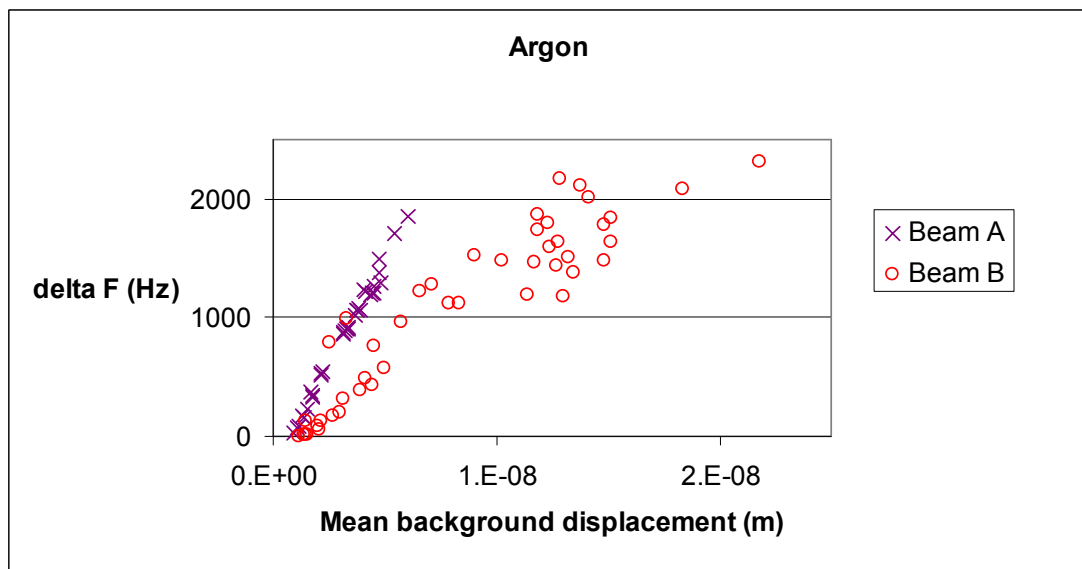


Figure 7.18: δF for beams A and B in argon

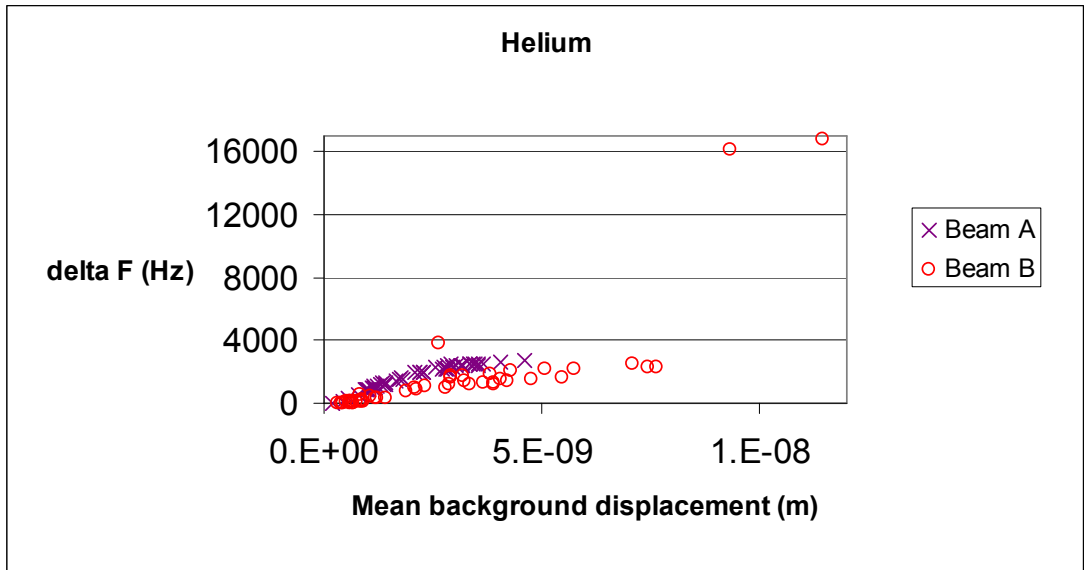


Figure 7.19: δF for beams A and B in helium

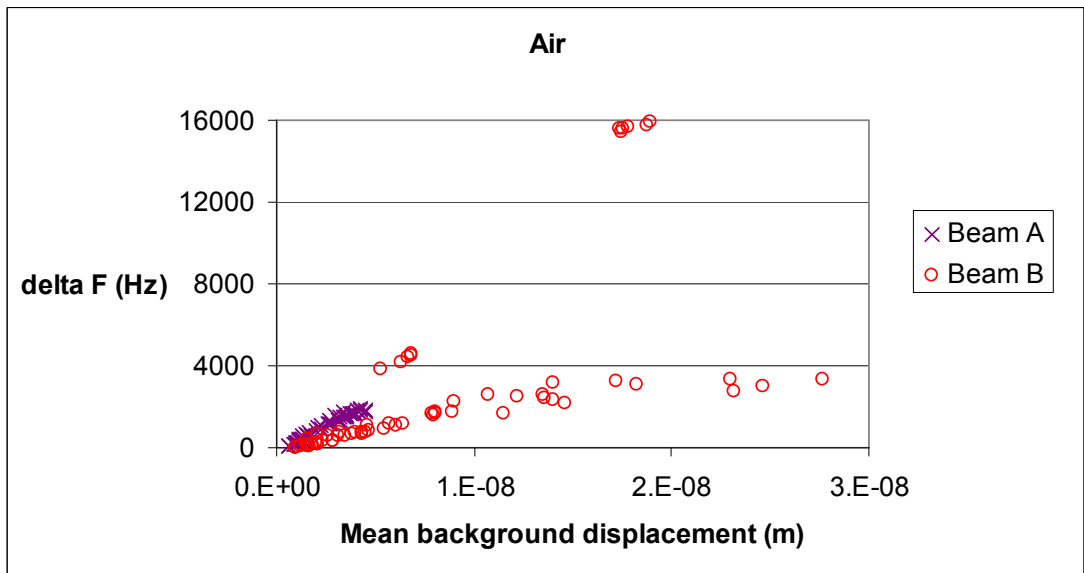


Figure 7.20: δF for beams A and B in air

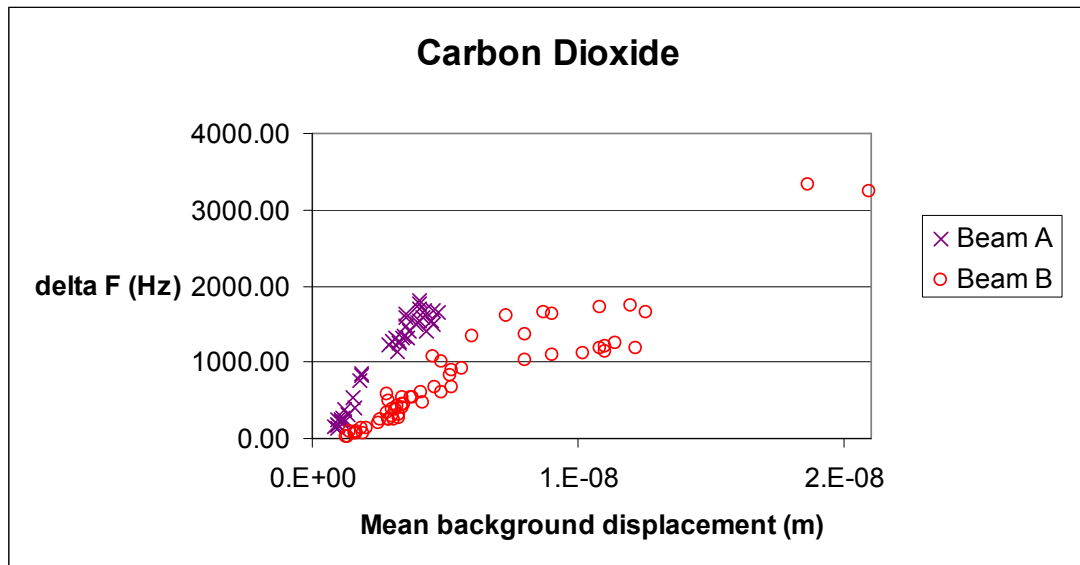


Figure 7.21: δF for beams A and B in carbon dioxide

The results for carbon dioxide indicate a clear distinction between beams A and B, with beam A appearing to offer greater δF for a given \bar{h} . The results for the other media, however, suggest that further attention must be paid to the background profile before any firm conclusions can be drawn.

7.4. Limits

In this section consideration is given to the maximum of the measurements taken, plus the limiting factors on the experiments.

7.4.1. Magnitude of readings

As can be seen from figure 7.7, it was possible to achieve values of δF in excess of 16 kHz. A reading of beam B in helium at 28 °C gave $\delta F=16.8$ kHz, with an applied voltage of 25V. This data set also yielded the largest measurement for the amplitude of vibration, at 16.7 μm (without correction for background contribution or position of measurement on beam, as discussed earlier). Although this displacement is of the order of the depth of the beam, it is still small when compared to beam length (of the order of 1%).

7.4.2. Achievable resonant modes

Limitations in the experimental equipment were such that frequencies could only be measured up to a maximum of 100 kHz. Referring to section 4.2.1, table 4.5, this means that it was not possible to analyse the second mode for these beams. To examine the achievable resonant modes, wide frequency sweeps were performed on beams A and B at low pressure i.e. near vacuum (see section 7.4.3), in a temperature range of 28.8 to 29.1 °C, with applied voltage levels of 30mV and 500mV. The results are shown in figures 7.22 and 7.23.

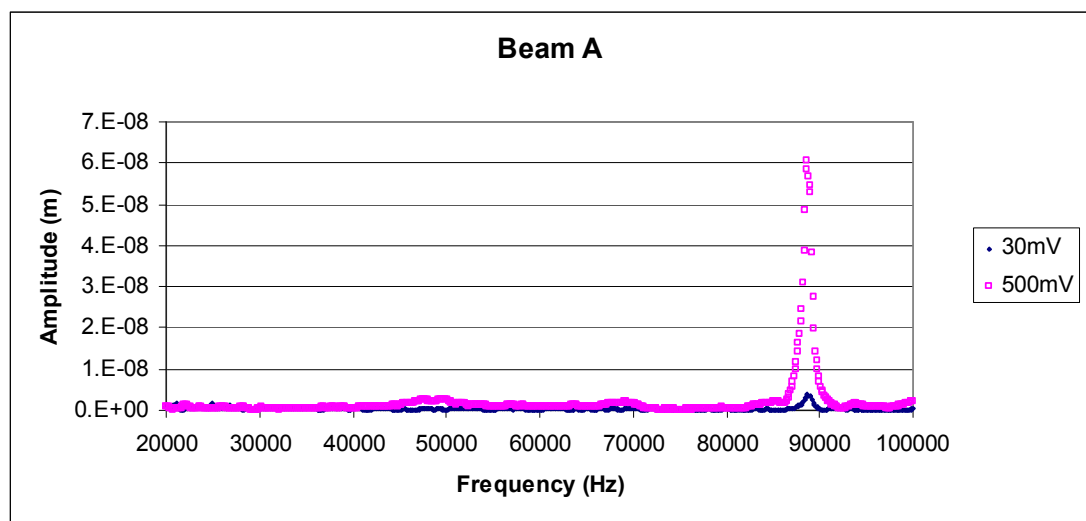


Figure 7.22: Resonance in beam A

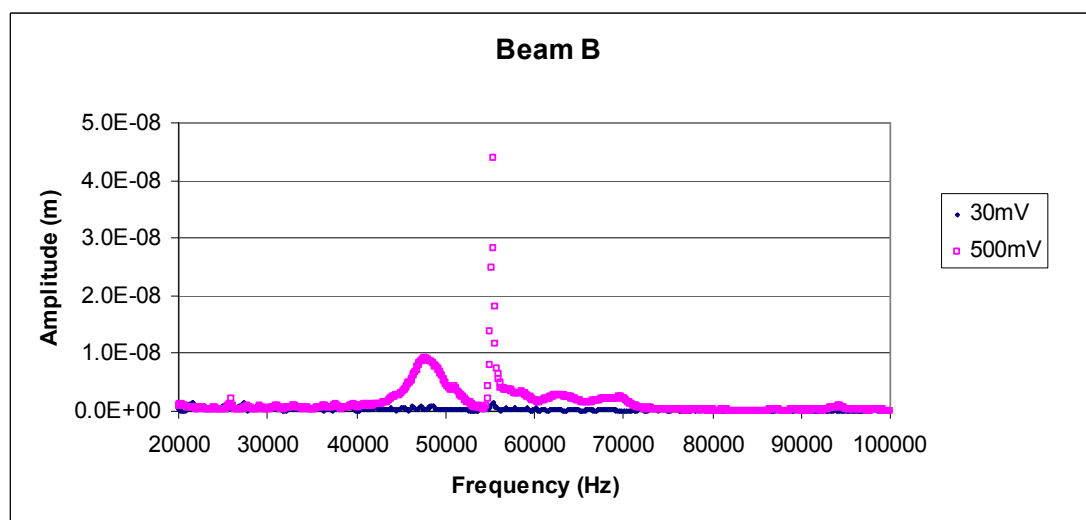


Figure 7.23: Resonance in beam B

For both beams, resonances occur where expected. At the lower voltage level, these resonances are only just perceptible, but become clear at the higher voltage. In the case of beam B, there appears to be some other resonant behaviour around the fundamental frequency. However, by examining the associated background for this reading, it becomes apparent that this is associated with the background profile. This is confirmed in figure 7.24 which shows a significant resonance at around 50kHz.

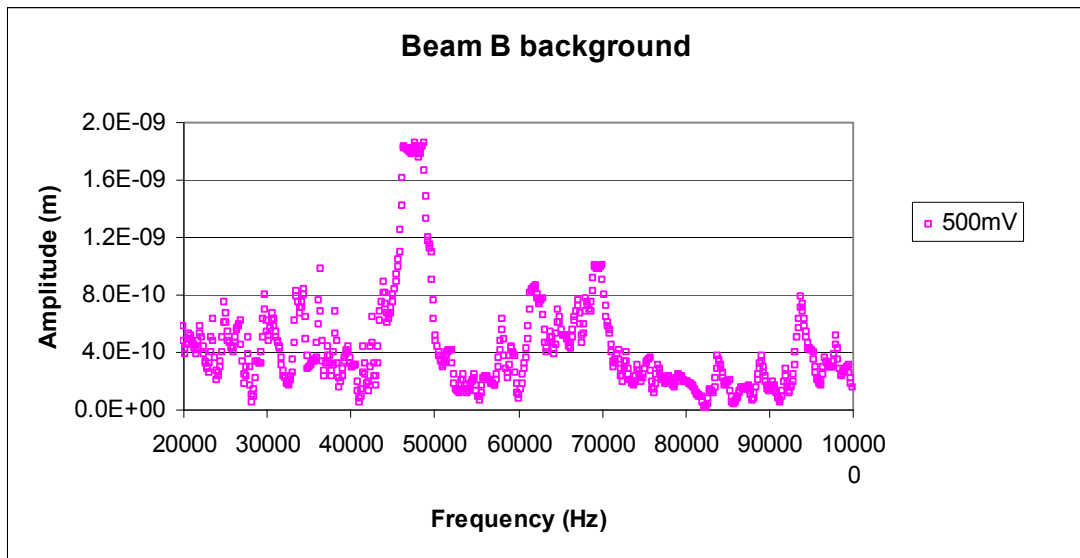


Figure 7.24: Background for beam B, 500mV measurement (see figure 7.23)

7.4.3. Pressure regimes

Pressure readings were gathered for all data sets, as outlined in section 6.4. The extremes of the measured voltage and converted pressure values are displayed in table 7.2 for readings in gas, plus readings taken at low pressure i.e. near vacuum.

Medium	Lower Voltage (V)	Lower Pressure (Bar)	Upper Voltage (V)	Upper Pressure (Bar)
Gas	2.475	0.99	3.561	1.4244
'Vacuum'	0.007	0.0028	0.043	0.0172

Table 7.2: Extremes of pressure

Using this data and considering the Knudsen numbers (see section 3.1) illustrates that:

- All gas measurements are in the viscous regime.
- The ‘vacuum’ measurements at low pressure are actually taken in the molecular/transition regime. For this reason, such measurements are referred to as ‘near vacuum’ rather than ‘vacuum’, and assumed to be air at low pressure.

7.5. Summary

In this chapter the essential experimental results have been presented. δF was found to reach values up to 16.8 kHz, and the effect of temperature on the background displacement and the boundary conditions noted. In the following chapter the results are analysed in finer detail, and the model adjusted accordingly.

Chapter 8

Analysis

The circular cylinder damping model was used to direct the device and experimental design. In this chapter, experimental data is used to develop a damping model based on the elliptic cylinder approximation. In developing this model, the influence of the applied background displacement is noted. Finally, the modelled beam behaviour is employed to make predictions regarding the sensitivity of nonlinear measurements to changes in fluid properties.

8.1. Approximations

8.1.1. Errors and uncertainties

As discussed in previous chapters, there are numerous uncertainties in the measured data and inherent inaccuracies in the single harmonic model for beam behaviour. Consequently it is extremely difficult to determine the uncertainty in any modelled data point. It would be misleading to include any error bars on plotted model data, and as such the figures in this chapter do not include any.

8.1.2. Reynolds and Keulegan-Carpenter numbers

In section 7.1.4 it was noted that the background displacement contributes only a negligible amount to the amplitude of vibration. As a consequence, any approximations for the Reynolds or Keulegan-Carpenter number do not consider the background contribution.

8.1.3. Beam and fluid properties

It is clear that the beam dimensions and fluid properties change with temperature. However, as discussed previously, it is not possible in this work to have an exact measure of the beam dimensions. Additionally, there is discrepancy in the literature regarding fluid properties at a given temperature (see Appendix A). It is useful

therefore to appreciate what effect such temperature induced changes will have on the pertinent measurand δF .

The following procedure was adopted to estimate this effect.

- Values for the viscosity and density of helium, carbon dioxide and argon at 20 and 26.85 °C were taken from Appendix A, source [10].
- Beam A was assumed to have ideal dimensions at 20 °C, and the expanded dimensions at 26.85 °C were calculated using properties given in Appendix B.
- The circular cylinder damping model was used to predict δF at two constant levels of background displacement, for each gas and temperature.

The results are plotted in figure 8.1.

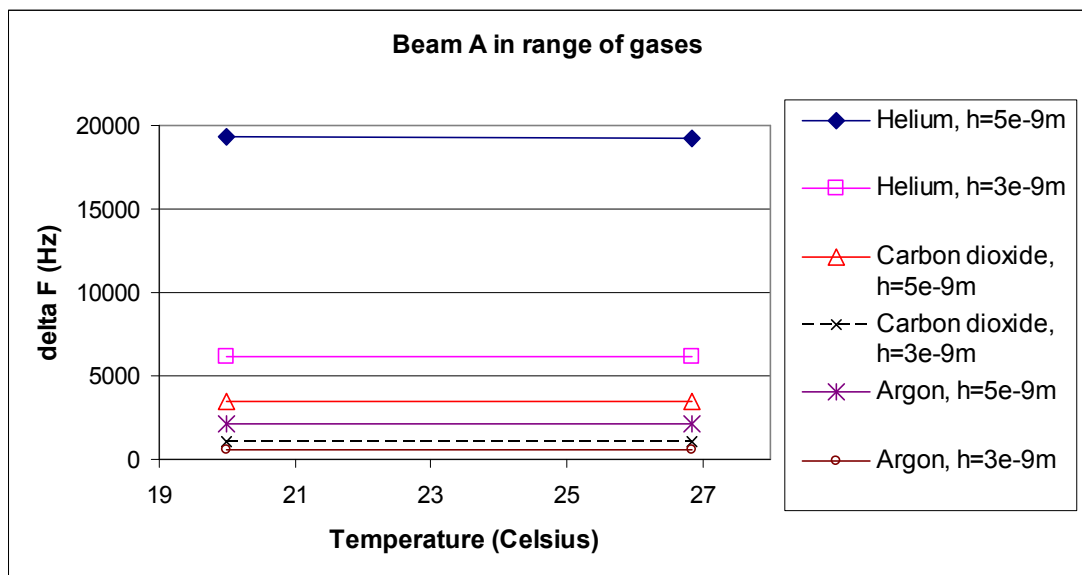


Figure 8.1: Effect on δF of temperature-induced changes to beam and fluid properties.

It is predicted that δF will typically change by less than 1% over this temperature range, at the given levels of background displacement. At lower displacement, this value can increase to around 2% in helium (whereas for carbon dioxide and argon, a reduction in background displacement quickly leads to linear behaviour.)

Beam dimensions are predicted to vary only by an order of around 0.001%. The beam is not fully constrained as the anchors are made of the same material, and subject to same thermal expansion. (Note that axial compression is dealt with

separately by considering the extension η .) This confirms the statement made in section 2.2.2 to this effect. Fluid properties are predicted to change by less than 3%.

It should be noted that, for all of the data in figure 8.1, the constraints of the circular cylinder model regarding Reynolds number and Keulegan-Carpenter number are broken. The maximum Reynolds number is estimated as 13.1 in carbon dioxide; maximum Keulegan-Carpenter number 2.91 in helium. However, the magnitude of the changes to beam dimensions and fluid properties over this temperature range suggest that any changes to fluid damping on the beam should be minimal. The circular cylinder model should then still be able to provide a qualitative description of the beam behaviour.

As a consequence of the above, the beam dimensions and fluid properties are assumed to remain constant across the temperature range of the subsequent analysis. Beam dimensions are taken as being ideal for both beams A and B, and fluid properties taken as the values at 25 °C given by Fluent (see Appendix A, source [7]).

8.2. Influence of background

In sections 7.1.1 and 7.2.1 it was observed that the profile of the background displacement over the important frequency range is highly dependent on the applied voltage and the temperature of the actuation apparatus. In addition, figures 7.6 and 7.7 in section 7.1.3 show that measurements of δF with similar mean background displacement can vary widely in magnitude.

To investigate the influence of the background further, measured background data is applied to the circular cylinder model to see what is predicted for beam response, and how this compares to the actual measured response.

8.2.1. Shifting and scaling background data for modelling purposes

One immediately apparent problem in applying measured background data to the modelled solution is that the model only accounts for the first harmonic at the fundamental mode. As hinted in section 4.5.7, damping encountered experimentally may be greater than that accounted for in the harmonic balance solution. This would in turn place any predicted resonance peak at a higher frequency than that measured.

In addition to this there are uncertainties regarding beam and fluid properties. The net effect is that a discrepancy is expected between the measured and modelled resonance peak. The consequences of this, and a proposed remedy, are outlined below.

Case 1 – applying background data directly to model in linear regime

A set of background and response data was selected for beam A in air. The background data was then input into a Matlab file based on the circular cylinder model, and the predicted frequency response plotted against the measured response – see figure 8.2.

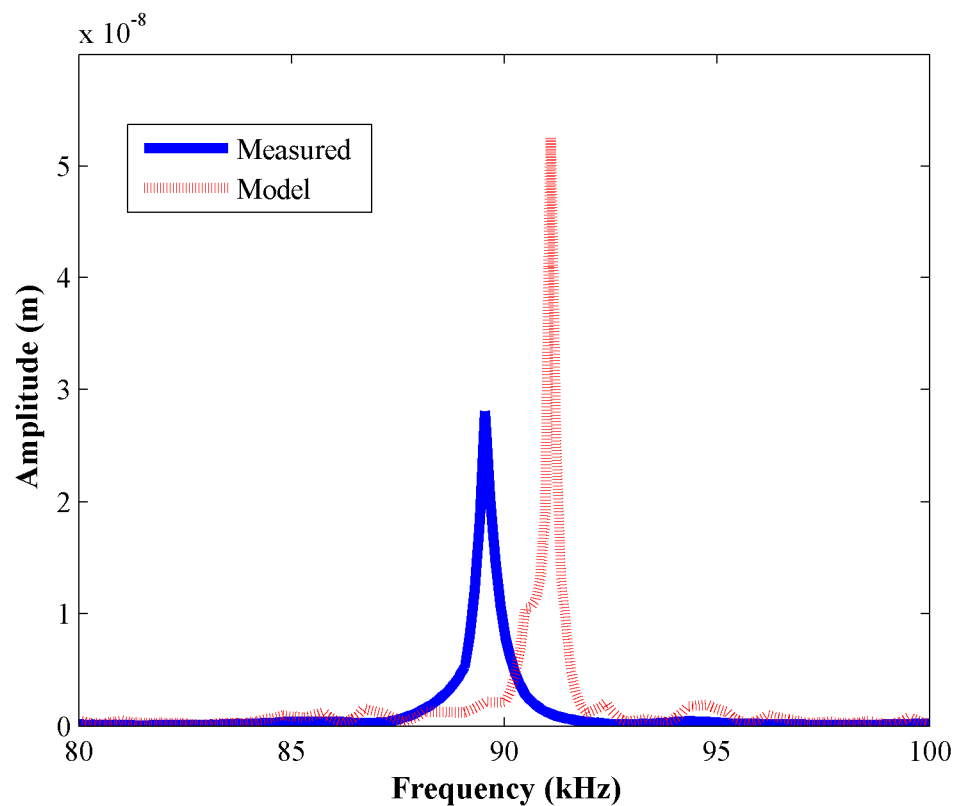


Figure 8.2: Measured and predicted response for beam A in air, where response is linear and background displacement is applied directly to the circular cylinder model.

As predicted, the measured case exhibits a lower resonant frequency than the model. In addition, the measured vibrational amplitude is lower than for the model. As discussed in section 6.4.3, data measurements may not have been taken at the precise centre of the beam, whereas the model predicts for the centre of the beam, giving maximum displacement in the fundamental mode. In this particular case the Reynolds number and Keulegan-Carpenter numbers are predicted to be within the

applicable limits – 0.06 and 0.01 respectively – suggesting that the circular cylinder damping model may be more reliable in the linear regime than nonlinear.

Note that the above plot is only achievable when the measured background is spread over a sufficient frequency range. For the vast majority of data gathered, the frequency range was minimised to improve resolution. The following case illustrates the consequence of this.

Case 2 – applying background data directly to model in nonlinear regime

Similarly to case 1, background data for beam B in air was applied directly to the circular cylinder model, and the results plotted in figure 8.3.

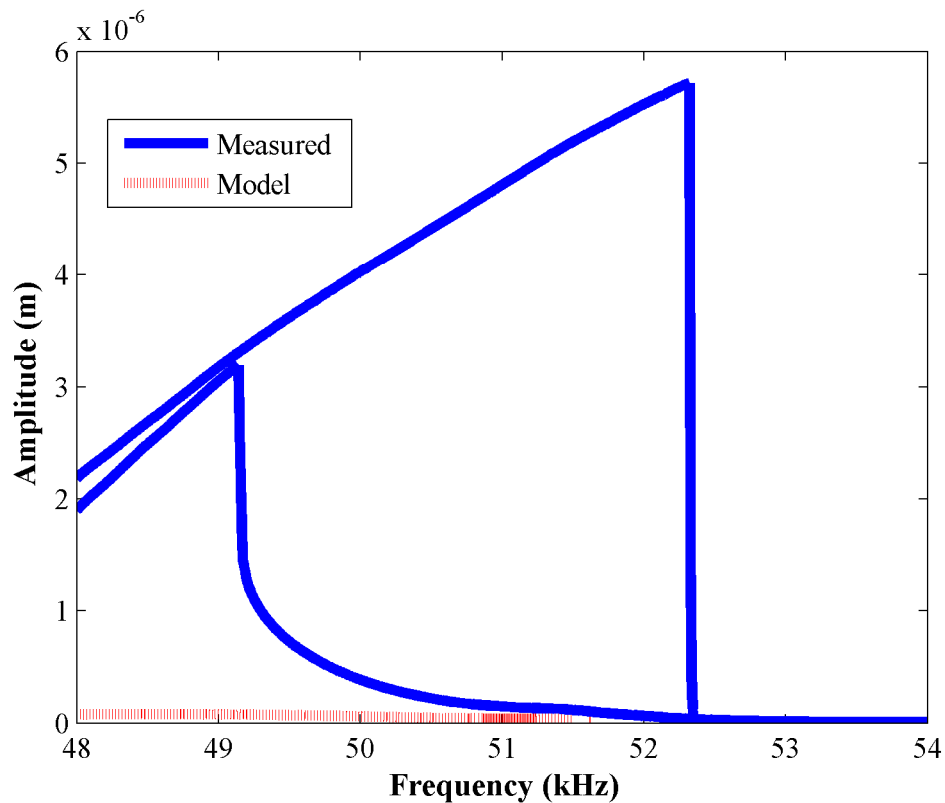


Figure 8.3: Measured and predicted response for beam B in air, where response is nonlinear and background displacement is applied directly to the circular cylinder model

In this case, the range of frequencies covered by the background data is such that it does not reach high enough frequencies for the model to make any useful predictions regarding resonant behaviour. To account for this it may be appropriate to ‘shift’ the background data up in frequency before applying it to the model. This translation

would allow an approximately equivalent background to be applied in the vicinity of the model's resonant frequency.

Case 3 – modifying and applying background data in nonlinear regime

To estimate the required frequency shift in the nonlinear regime, it is first necessary to determine \bar{h} from the measured data, as outlined in section 7.1.3. This constant \bar{h} is then applied to the circular cylinder model, across a sufficiently broad frequency range so that the model predicts a nonlinear response. An example is shown in figure 8.4.

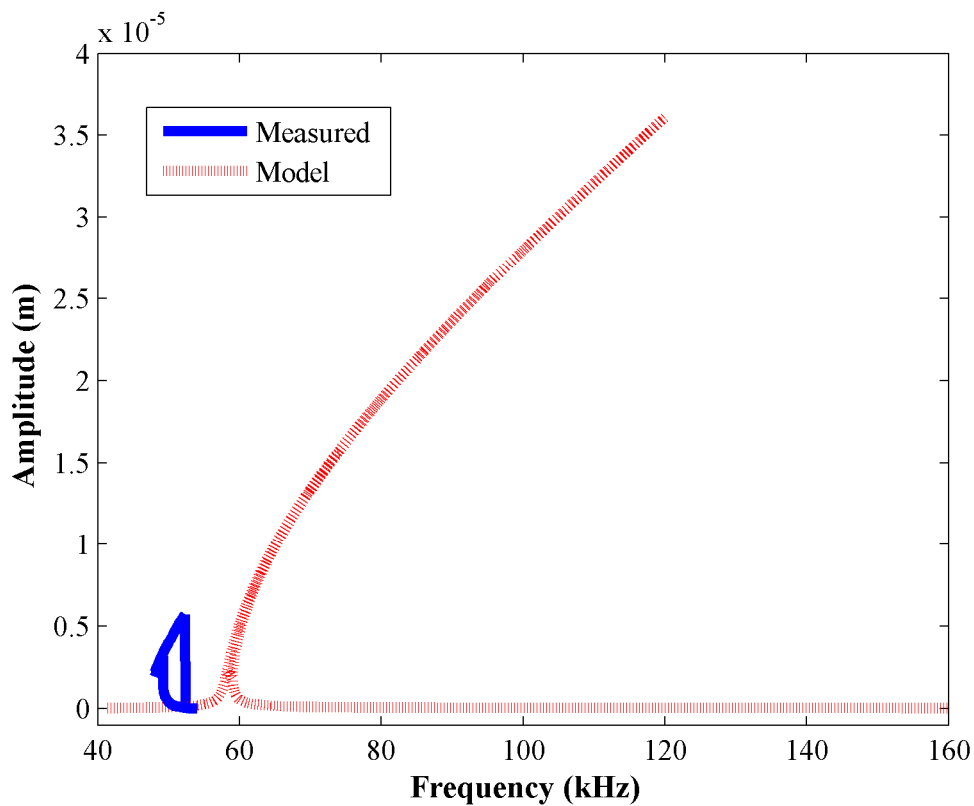


Figure 8.4: Estimating required frequency shift for beam B in air, using circular cylinder model

In this case it is apparent that simply applying \bar{h} to the model does not give a particular accurate prediction of δF . However, investigations show that the frequency of the lower jump point in any modelled data is far less susceptible to a change in \bar{h} than the upper jump point. With this in mind, the required frequency shift may then be approximated as the frequency separation between the measured lower jump point and the modelled lower jump point.

Before applying this translation to the background data, it is important to note that the actual forcing applied to the beam is proportional to $\omega^2 h$, whereas fluid damping for both cylinder models is a function of ω . Both of these factors are crucial in determining beam behaviour, and so any translation must account for the effect of a change in frequency. Regarding the forcing, any increase in the frequency of the applied background data must be accompanied by an appropriate reduction in the background displacement amplitude, to maintain an equivalent forcing level. As for the damping, in order to match the measured case, any modelled data must calculate the fluid damping as if using the unshifted frequency. From this point forward, the frequency shift and amplitude scaling applied to the background data will simply be referred to as SHIFT.

Figure 8.5 shows the result of applying the appropriate SHIFT to the data for figures 8.3 and 8.4.

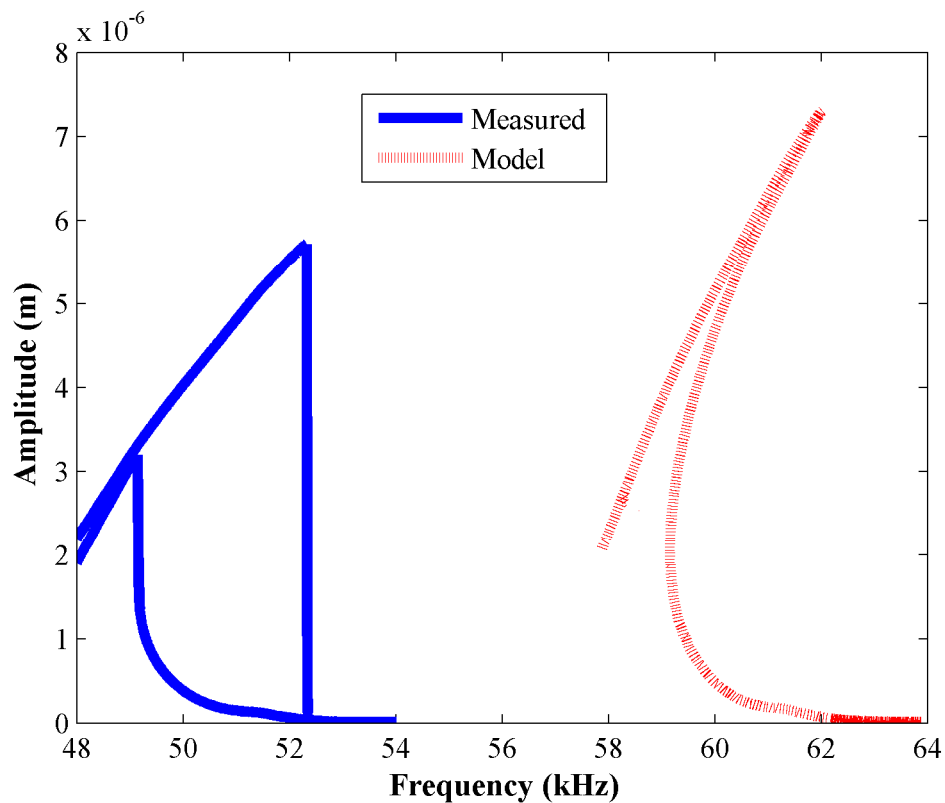


Figure 8.5: Applying SHIFT to circular cylinder model for beam B in air

It is apparent that using this SHIFT, although crude, gives a far better agreement between measured and modelled δF . Again, it is noted that the constraints of the

circular cylinder damping model are broken in the nonlinear regime, but this should not detract from the effectiveness of using this approach.

8.2.2. Effect of background profile

To confirm that the aforementioned discrepancies in δF at similar \bar{h} are not due to any measurement errors, a selection of data for beam B in air was chosen for investigation. Again, the circular cylinder model was adopted, and appropriate SHIFT applied to each data set, to compare predicted and measured δF . Figure 8.6 shows the results.

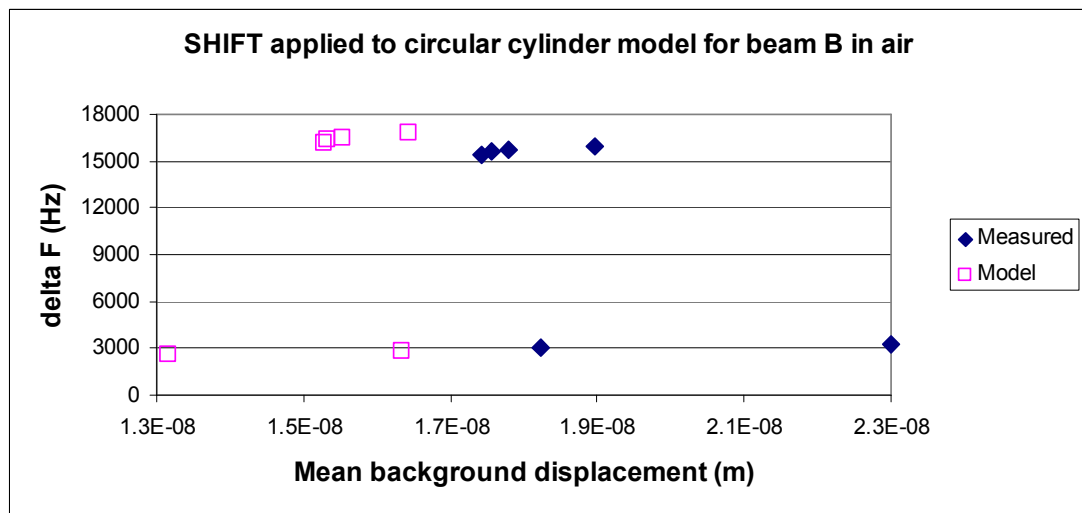


Figure 8.6: Effect of using SHIFT on δF and mean background displacement

The mean background displacement for the model is calculated between the predicted jump points. The scaling inherent in SHIFT causes the mean background displacement to reduce in the model data. However, it is clear that the model follows the same trend as the measured data. These qualitative predictions indicate that the discrepancies in δF are not due to any experimental errors, but are genuine phenomena to be explained.

To investigate further, two of the shifted and scaled backgrounds used in figure 8.6 are compared. Figure 8.7 shows a plot of these backgrounds, with the jump point frequencies indicated by circles, and note made of \bar{h} and δF associated with each.

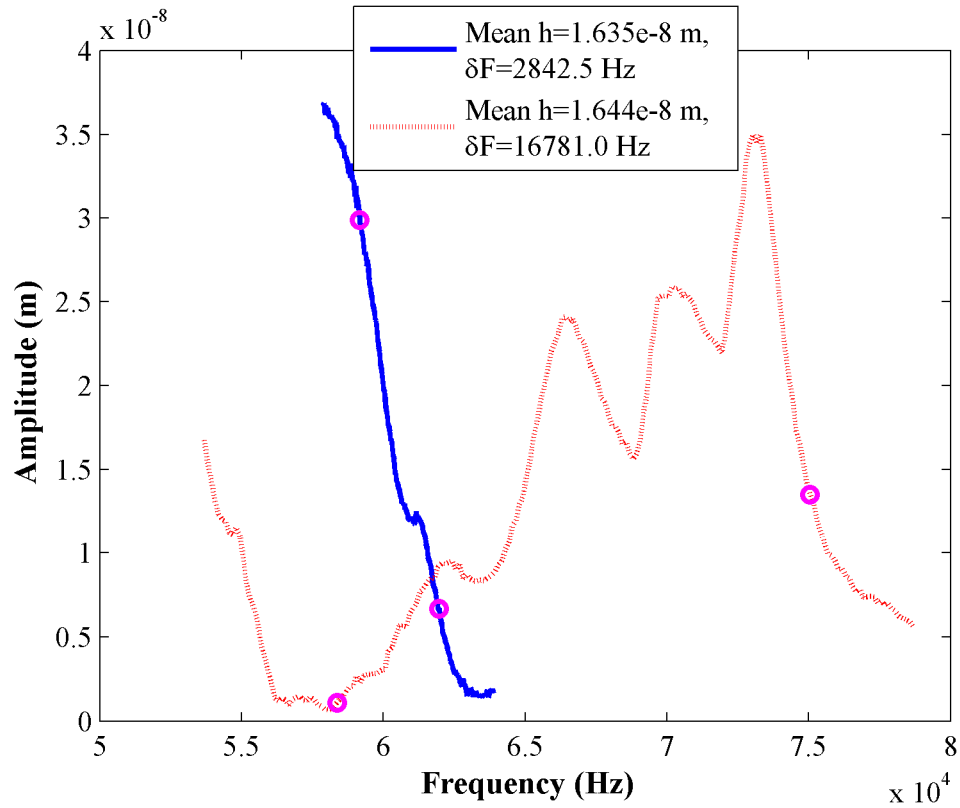


Figure 8.7: Comparison of shifted and scaled backgrounds for beam B in air. Jump point frequencies are indicated by circles placed on the relevant background profile

It is apparent that these two backgrounds, though similar in \bar{h} , demonstrate markedly different profiles in the vicinity of the associated jump points. For the case with lower δF , the background reduces in amplitude between the lower and upper jump points. The converse is true for the case with the higher δF . Noting that the model has so far not accounted for any extension term η , nor any other influencing factors, it is then concluded that δF is highly dependent on the background amplitude and profile in the vicinity of the resonant frequency.

8.3. Detailed modelling

In this section, the molecular damping and elliptic cylinder damping models are employed, along with experimental data, to develop a damping model for beam A. The aim is to develop a model which can predict, with reasonable accuracy, the behaviour of beam A over the range of temperature, pressure and displacement considered in the experiments.

As discussed in section 1.4.4, fluid damping will not account for all of the damping on the beam. There will be contributions from other damping mechanisms. For modelling purposes, this additional damping will be accounted for by including a damping coefficient, which is referred to as *OTHER*. In the molecular damping regime then, the damping coefficient is taken as $c = MOL + OTHER$, where $MOL = \frac{pb}{\nu_T}$ represents the molecular damping per unit length; in the viscous regime, $c = \Phi\mu + OTHER$, where *OTHER* is to be determined from experimental data.

Preliminary modelling consistently showed that the circular cylinder model overestimates the damping in the nonlinear regime (where the relevant constraints on the Reynolds and Keulegan-Carpenter numbers are broken.) To adjust for this would require the inclusion of a negative *OTHER* term; this is nonsensical and consequently the circular cylinder model was considered insufficient for purposes of this section.

In working with the elliptic cylinder model, it should be noted that the aspect ratio of beam A, and indeed beam B, is such that thickness effects may become important. This may negatively effect the validity of the damping coefficient model, but does not prevent attempts at a numerical fit being made.

8.3.1. Molecular regime - linear

Analysis of linear data gathered in the molecular pressure regime allows for an approximation of the coefficient OTHER in this regime, as well as a working expression for the extension η . As outlined in section 4.5.3, η may have a negligible effect on bandwidth and δF , but can significantly effect the resonant frequency.

The low damping in the molecular pressure regime suggests that it is acceptable to use the following relationship between quality factor Q , damping ζ , damped resonant frequency ω_d and bandwidth $(\omega_2 - \omega_1)$: $Q \approx \frac{1}{2\zeta} \approx \frac{\omega_d}{(\omega_2 - \omega_1)}$ [1]. This expression may be considered valid where $\zeta < 0.05$, and subsequent investigation showed this to be true throughout the molecular regime measurements.

Note that in the linear regime, any calculations for \bar{h} are determined over the bandwidth, and the frequency shift (SHIFT) determined by measuring the separation between the measured and the modelled resonance peaks.

Determining the extension η

As illustrated in sections 4.5.2 and 4.5.3, the resonant frequency does not change rapidly with \bar{h} or ζ , but is highly sensitive to η . In section 7.2.2 it was confirmed that the resonant frequency changes with temperature, most probably as a consequence of changes to the boundary conditions, and hence η . Together, these observations suggest that an approximate temperature-dependent extension term η may be developed to account for variations in resonant frequency with temperature.

To determine an expression for η , the following procedure was followed:

- The damped resonant frequency of the beam was read over a range of temperatures, where the pressure and \bar{h} were held approximately constant.
- For each data set, the first aim was to match the measured and the modelled Q values, whilst holding η at zero in the model. Consequently, rather than use the coefficient MOL for molecular damping, the coefficient c was set to allow matching. In this process, the mean \bar{h} , with a suitable SHIFT for scaling, was used, rather than use the true background data. This was found to be necessary at the given level of applied displacement in order to accurately read the resonant frequency or bandwidth from the modelled data. Using the true background data in the Matlab model was found to produce indistinct resonant peaks and halfpower points; this may be explained by the presence of noise in the system, and the model's interpretation of such noisy data.
- The assumption was then made that η was actually zero at the lowest temperature for the data sets under consideration. At the experimental stage it was not possible, given the equipment and methodology, to measure η directly, and so it is necessary to make an assumption of this type to allow for further modelling.
- For the higher temperature data sets, η and c were then finely tuned. The aim was to maintain a match of Q with the measured data, whilst simultaneously setting the resonant frequency of the model such that the rate of change with temperature closely matches that seen in the measured data. This is illustrated below in figure 8.8a. It was then possible to extract an approximate linear dependence of resonant frequency on temperature in the model.
- The values of η used at each temperature were then taken and plotted against temperature, as shown in figure 8.8b. Again, an approximate linear expression could then be extracted, giving a temperature-dependent formula for η .

The above procedure for beam A yielded the following:

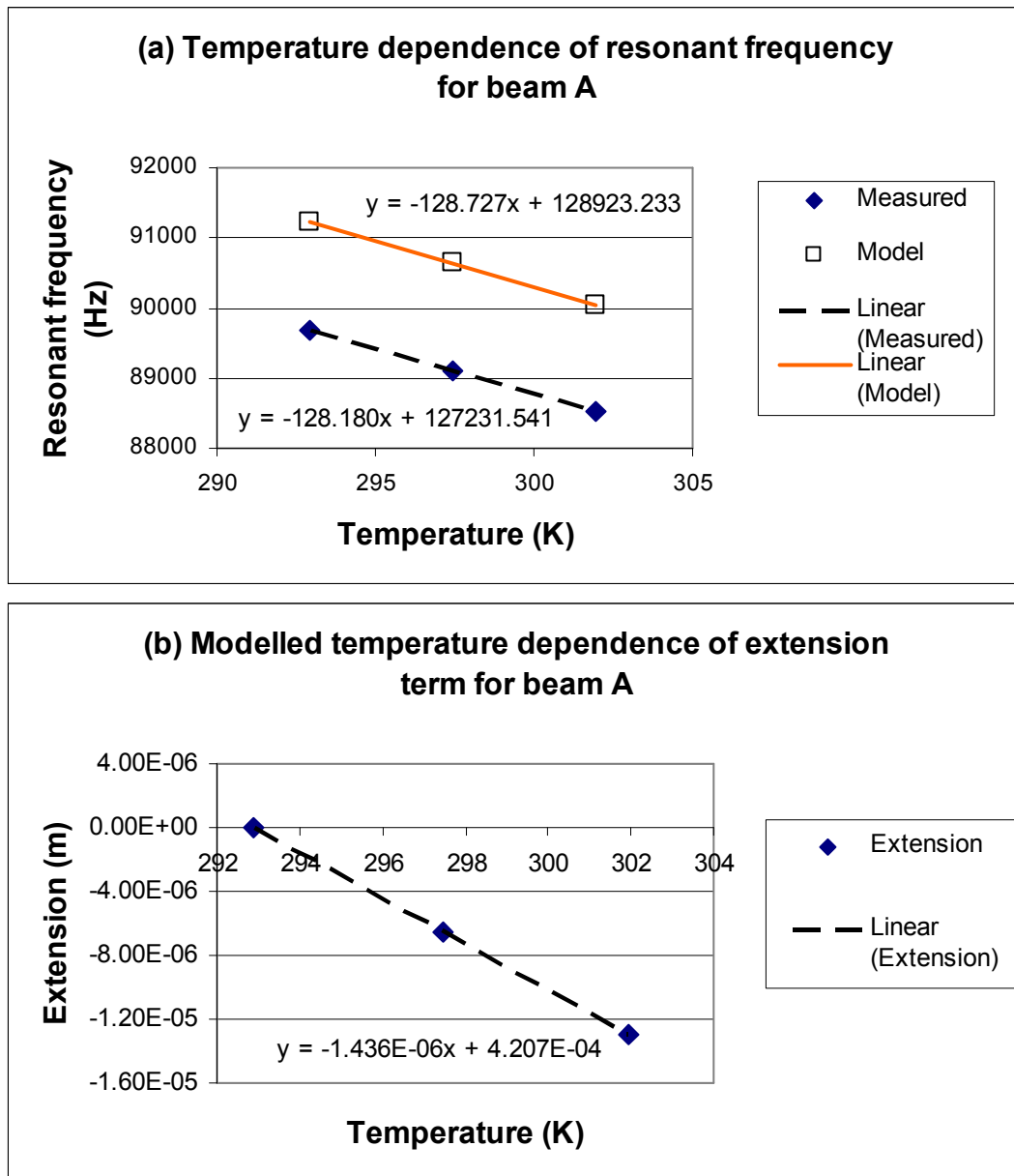


Figure 8.8: Determining a temperature dependent formula for tension η in beam A

The expression for η is then taken to be $\eta = (-1.44E-6 \cdot T) + 0.00042$, where T is the temperature in Kelvin, i.e. is represented in the form $\eta = \eta_0 + \eta(T)$. Although this does not give a true absolute value for η , for reasons stated above, it is valuable in that it can closely predict the behaviour of the resonant frequency with temperature. This expression is included in subsequent modelling.

Determining damping coefficient *OTHER*

The damping coefficient *OTHER* would be expected to include a contribution from the intrinsic losses. According to the formulae presented in section 2.5, support losses to beam A would be expected to contribute a value of approximately $1.82\text{E-}6$ to this coefficient, surface losses $2.27\text{E-}6$, and thermoelastic losses $2.94\text{E-}11$.

To determine *OTHER*, this procedure was followed:

- Maximum and minimum values for the measured quality factor Q were calculated by accounting for the resolution of the measurements. From these, maximum and minimum values for the damping coefficient c were then calculated.
- The molecular damping coefficient *MOL* was calculated in each case, using recorded pressure and temperature data. Maximum and minimum values for *OTHER* were then calculated using $c = \text{MOL} + \text{OTHER}$.

In doing these calculations, several instances of *OTHER* were found to have a negative value. As this cannot reflect the true situation, it is assumed that there is an inaccuracy in the calculation of the molecular damping coefficient *MOL*. Consequently, only positive values for *OTHER* are considered. For a working value of *OTHER* then, a mean is taken across all such positive values. This returned an approximate coefficient as $\text{OTHER} = 1.8\text{E-}5$. This value exceeds that predicted for intrinsic losses and is thus adopted for subsequent calculations in the linear regime.

Regarding the calculations of *MOL*, it is worth noting that for smaller *MOL* values a larger Q is observed, as would be expected. Although *MOL* calculations may contain inaccuracies, they are still then of qualitative value.

Background discrepancies

In analysing this linear data in the molecular regime, particular discrepancies were noticed in some of the background data. Several of the background displacement readings were found to be of a far higher magnitude than expected, such that using this data with the Matlab model produced nonlinear results. An explanation may come from the actuation arrangement and the measurement procedure, as discussed in sections 6.2.4 and 6.4.3. In attaching the silicon device to the copper disk, it is possible that certain regions on the device remained unbonded, and as such have a certain freedom to vibrate. These local regions may then have their own frequency response. It is impossible to ensure that background measurements were taken from precisely the same spot every time. It is possible that certain readings were taken in one of these local regions, skewing the results.

The magnitude of these discrepancies was such that all background data for the linear regime had to be carefully evaluated. In the nonlinear regime however, the magnitude of the applied piezo displacement is such that these localised effects can largely be ignored.

8.3.2. Molecular regime - nonlinear

To approximate the coefficient *OTHER* for beam A in the nonlinear regime, a similar process was followed as for the linear regime. In this case the previously determined formula for η was adopted, and a match sought between the measured and modelled δF . Again, a mean was taken over the positive values obtained for *OTHER*, giving an approximate coefficient of $OTHER = 1.3E-4$ to be used in subsequent calculations in the nonlinear regime.

The apparent discrepancy between the values of *OTHER* in the linear and nonlinear regime may require explanation. It may be that the damping on unaccounted harmonics, which will be greater in the nonlinear case than linear, are responsible for these model predictions. To verify this however is not within the scope of this work.

8.3.3. Viscous regime - linear

Having determined values for η and $OTHER$ in the molecular regime, the next aim was to establish values for parameters a and b in the elliptic cylinder model. These values should be such that model predictions offer good agreement with measured data across the four chosen viscous gases.

In the linear regime, it was found that the Reynolds number consistently remained below 1 in all of the gases. This allowed for an analytically determined parameter a in each gas. It was then noted that $\zeta < 0.05$ in all gases, confirming that it is reasonable to use the aforementioned approximation for Q when considering damping on the system. By adjusting parameter b in the model for each gas, and using a mean \bar{h} of lower magnitude for reasons given above, it was then possible to match the measured and modelled Q . Having done this for several data sets for each gas, a mean value of parameters a and b was taken.

Using $a = 0.75$, $b = 2.85$, and $OTHER = 1.8E-5$, the Q at three different temperatures was modelled for each gas and plotted against the measured value. In each instance the maximum and minimum values of Q were calculated according to the resolution of the modelled and measured data, and a mean taken. These mean Q values are shown in figure 8.9.

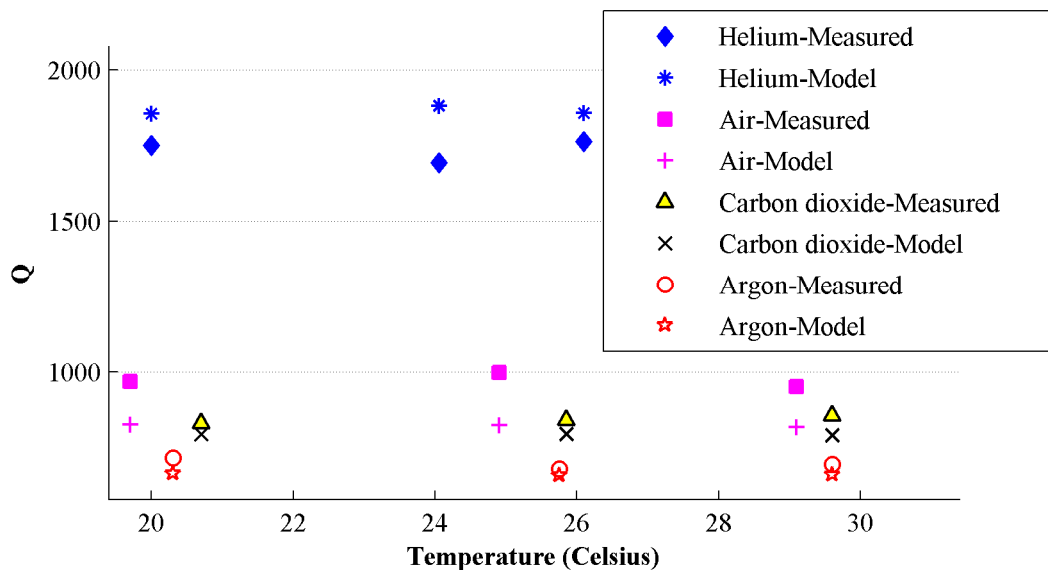


Figure 8.9: Quality factor for beam A in four viscous gases; measured and linear elliptic cylinder model

Although, as mentioned, it would be misleading to include error bars on modelled data, it may be worth investigating how closely this model and measured data appear to match. By considering the maximum and minimum Q values, it was possible to gain an impression of the difference between measured and modelled data. These are summarised in table 8.1.

Fluid	% Disagreement	Comments
Air	10 to 14	Model is over-damped
Argon	1 to 5	Model is over-damped
Carbon dioxide	2 to 5	Model is over-damped
Helium	0 to 2	Model is under-damped

Table 8.1: Disagreement between measured and modelled quality factors for four gases in viscous regime

The agreement between the model and measured data appears to be strong, other than in the case of air. The model parameters are taken forward to section 8.4 below.

8.3.4. Viscous regime - nonlinear

In order to determine parameters a and b in the nonlinear regime, a similar process is followed as for the linear regime, except a match is sought for δF as opposed to Q. At this higher level of background displacement, the Reynolds number remains below 1 only in the case of helium. As a result, a mean initial value for parameter a was obtained using the analytical formula with helium only. Subsequently, a series of iterations were performed on each data set to establish values for a and b which provided a reasonable agreement between the measured and modelled δF in all gases.

With $a = 1.1$, $b = 1.2$, and $OTHER = 1.3E-4$, δF was modelled at three different mean background displacements for each gas and plotted against the measured value. Again, mean values for δF were calculated according to the resolution of the modelled and measured data. Results are shown in figure 8.10.

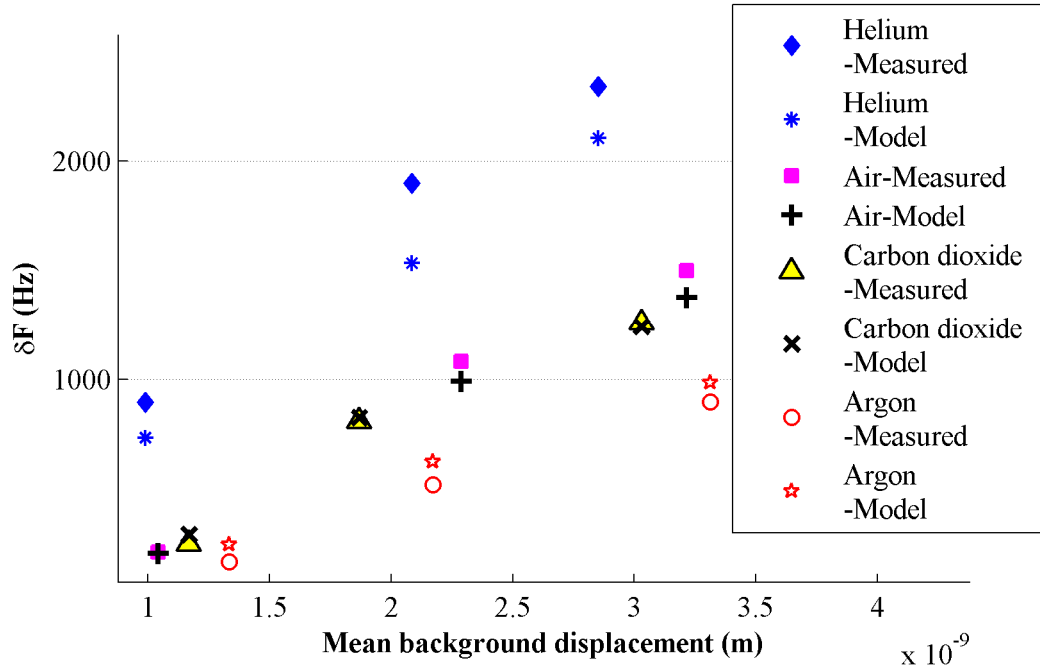


Figure 8.10: δF for beam A in four viscous gases: measured and nonlinear elliptic cylinder model

As before, the difference between measured and modelled data was examined with regard to resolution. Table 8.2 summarises these findings.

Fluid	% Disagreement	Comments
Air	0 to 7	Model is over-damped
Argon	9 to 42	Model is under-damped
Carbon dioxide	0 to 12	Model is variable
Helium	9 to 18	Model is variable

Table 8.2: Disagreement between measured and modelled δF for four gases in viscous regime

Agreement between the model and measured data varies noticeably between the gases. Air and carbon dioxide show good agreement over the range of background displacements considered. With argon, the percentage disagreement appears greatest at the lower levels of background displacement. For helium, the disagreement was seen to increase greatly at higher background displacements beyond the range considered in figure 8.10. With this in mind, the model parameters are taken forward to section 8.4.

8.4. Sensitivity

In this section the practicality of using the resonating beam A as a gas sensor is examined. The effectiveness of using linear and nonlinear measurements is compared, and predictions made using the developed damping model.

8.4.1. Identifying gases

Referring back to figure 7.6 in section 7.1.3, it is apparent that helium and argon can clearly be identified by δF . Air and carbon dioxide however appear difficult to distinguish without thoroughly investigating the background displacement. It is therefore appropriate to examine whether linear measurements can distinguish between the gases.

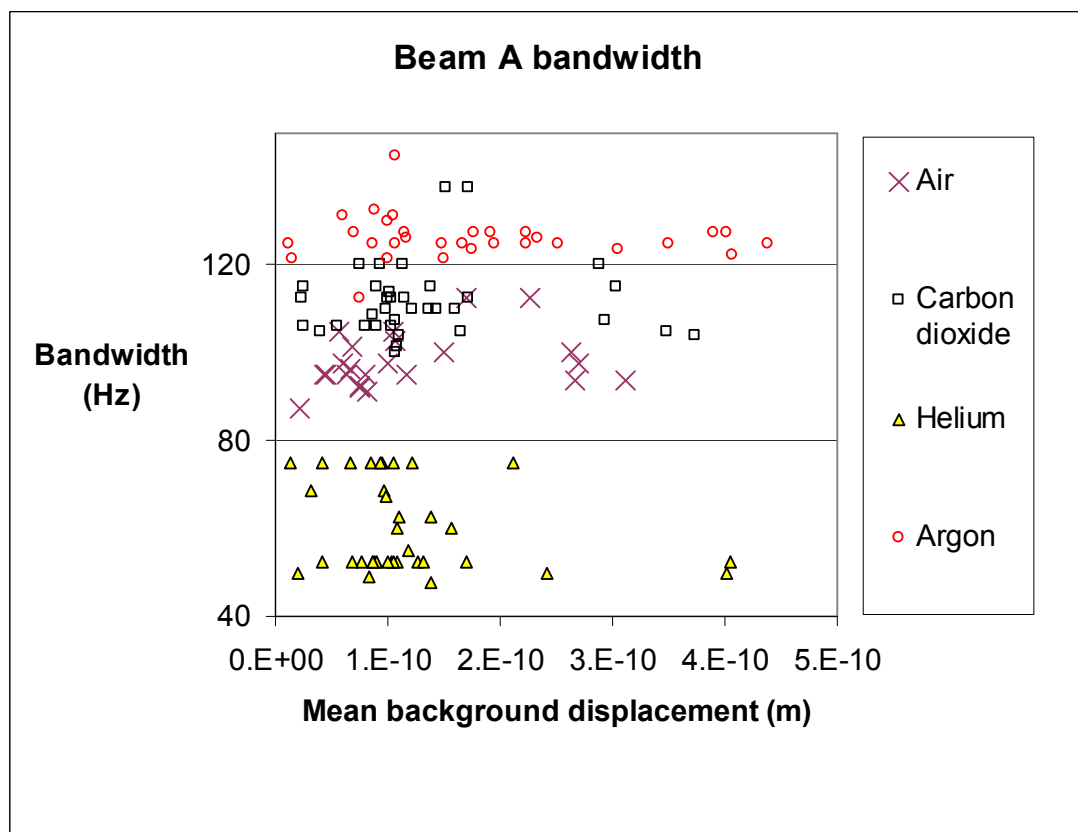


Figure 8.11: Measured bandwidth of beam A in viscous gases

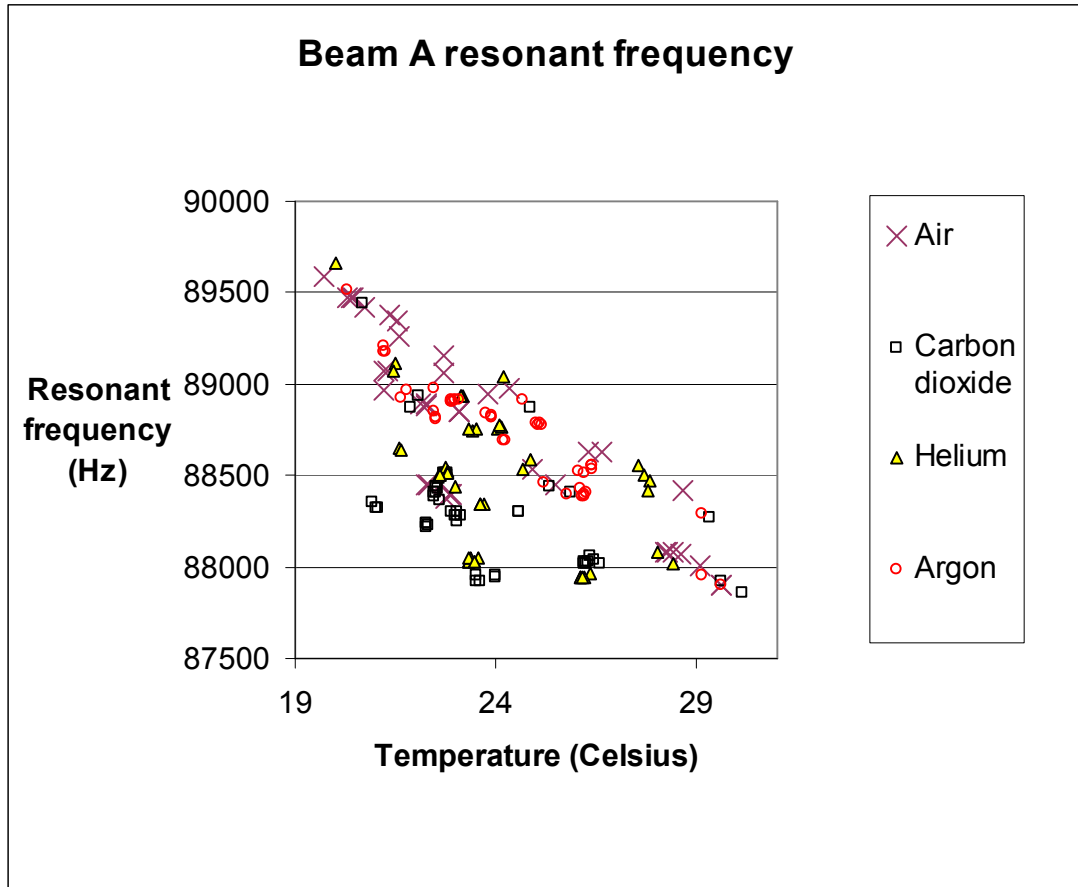


Figure 8.12: Measured resonant frequency of beam A in viscous gases

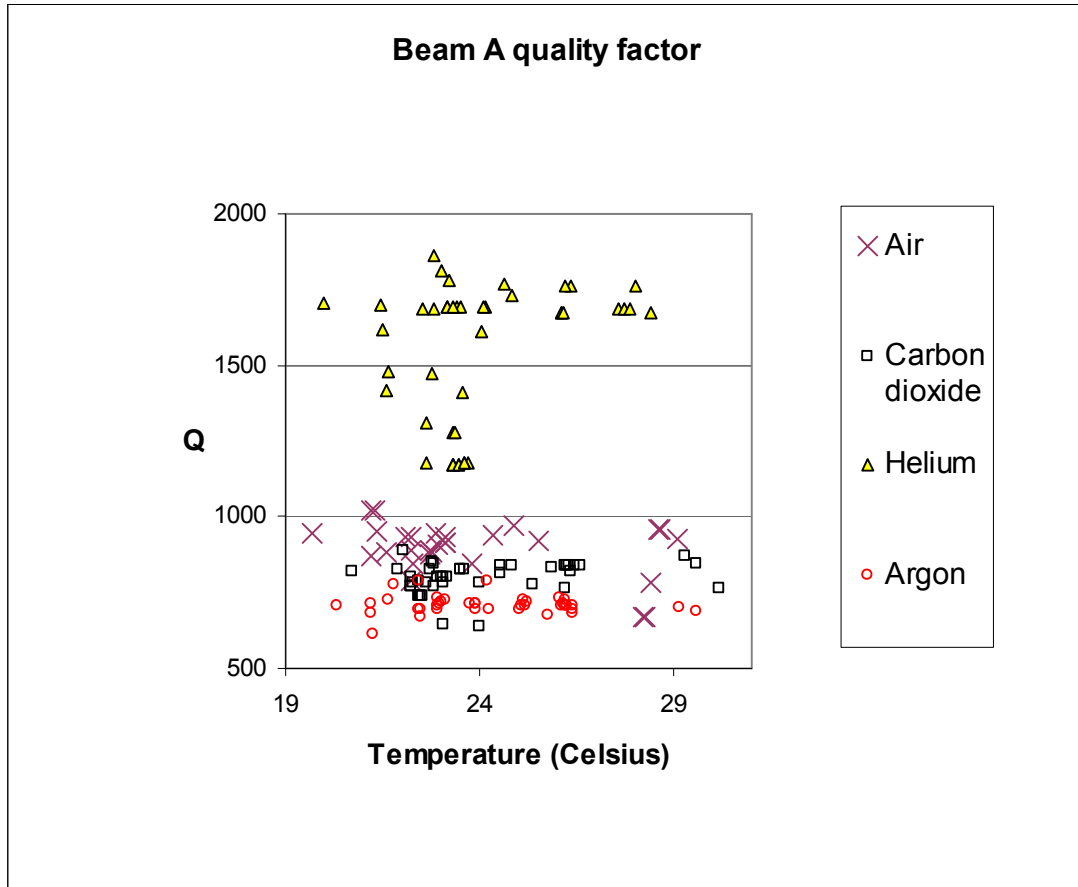


Figure 8.13: Measured quality factor of beam A in viscous gases

Figures 8.11, 8.12 and 8.13 reveal the following:

- Helium is identifiable by bandwidth and quality factor.
- Argon may be identifiable by bandwidth and quality factor, but exhibits similarities to air and carbon dioxide.
- Air and carbon dioxide exhibit small differences, but can be difficult to distinguish.

Linear and/or nonlinear measurements then allow for the identification of helium and argon. A way of definitely distinguishing between air and carbon dioxide has yet to be identified. Investigation of the linear data shows that the bandwidth can differ between air and carbon dioxide by typically around 25Hz. To examine relevant nonlinear data requires selecting data sets with comparable temperatures and background displacements. Figure 8.14 presents δF for five such comparable data sets.

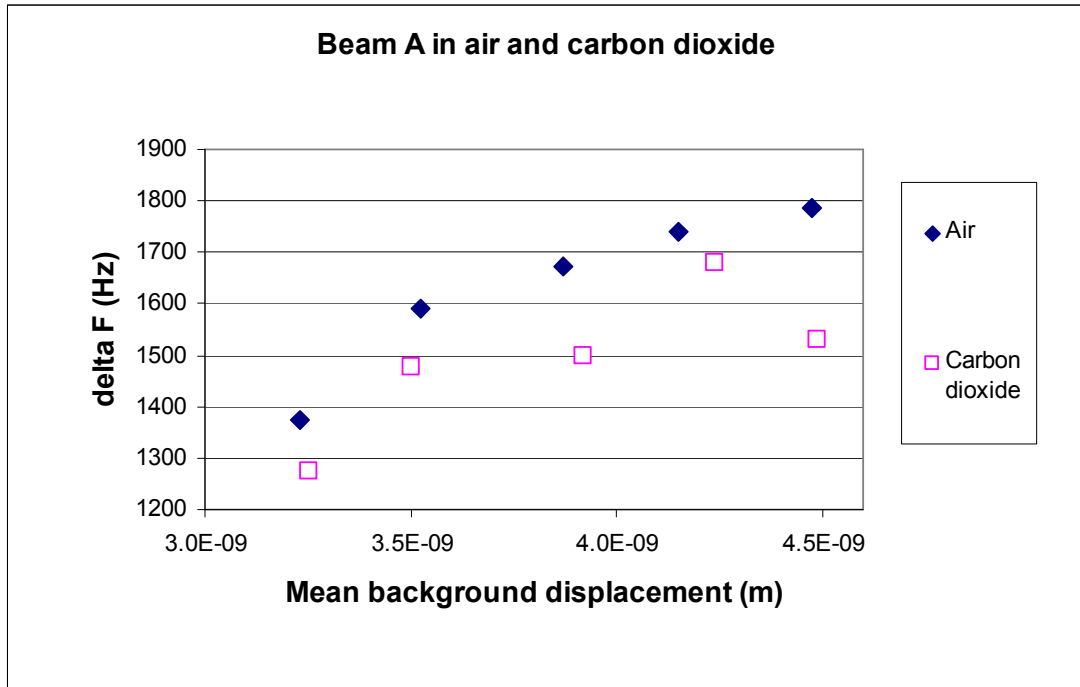


Figure 8.14: Selected measured δF data for beam A in air and carbon dioxide

The data selected for figure 8.14 illustrates that a difference in δF of up to 250 Hz can be achieved over the chosen background displacement range. In terms of distinguishing between air and carbon dioxide, this is an order of magnitude greater than that achieved by linear measurements. However, fluctuations in the data indicate that there remain uncertainties.

To further investigate the usefulness of nonlinear measurements for distinguishing between these gases, the developed damping model was used to predict δF for both gases at 25 °C, and the results plotted in figure 8.15.

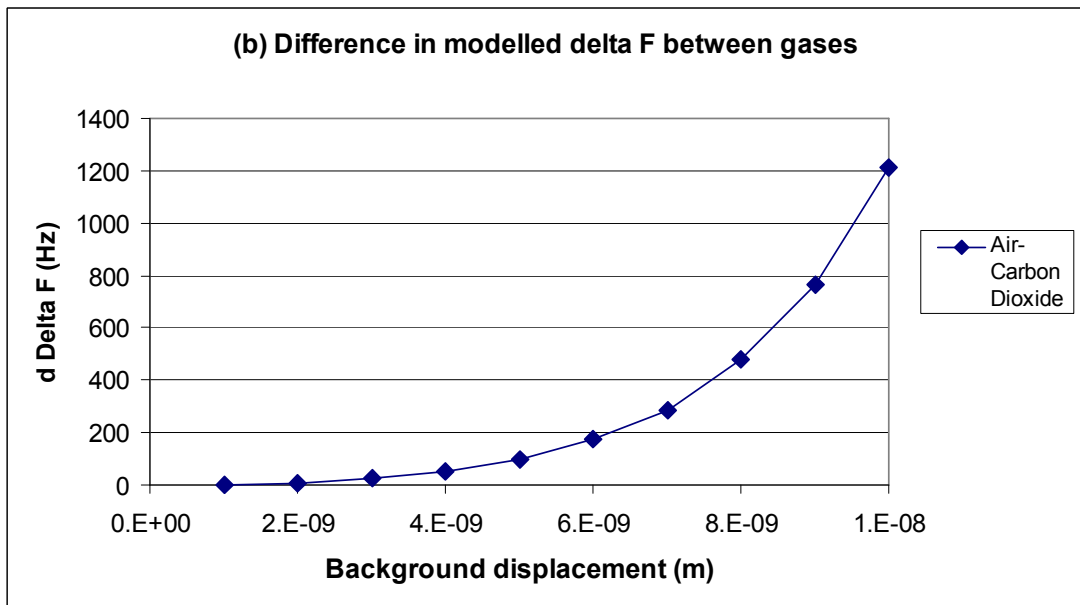
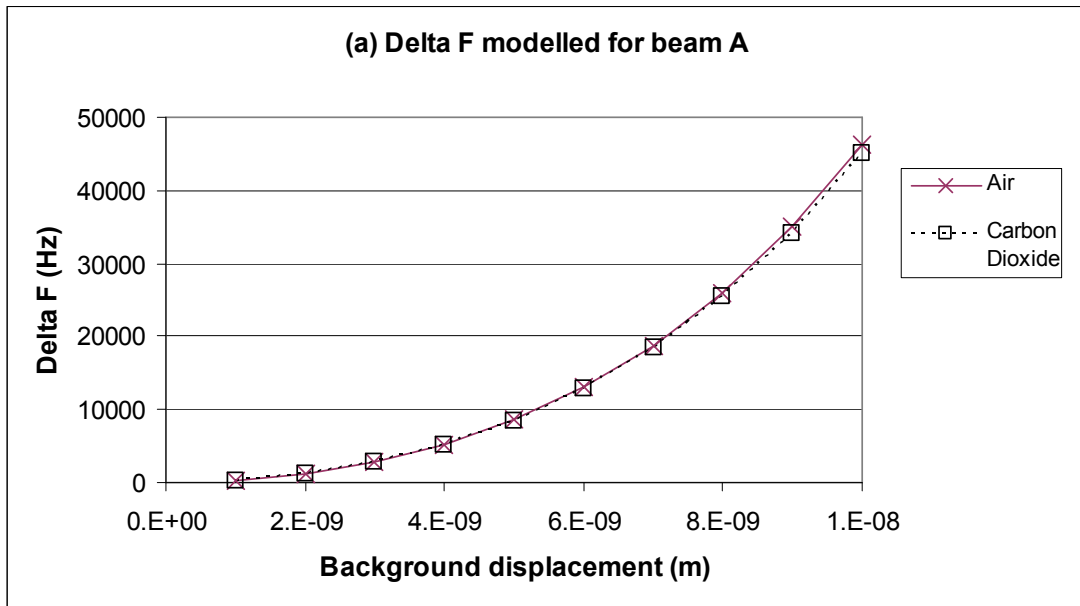


Figure 8.15: Elliptic cylinder model predictions for beam A in air and carbon dioxide

Figure 8.15 shows that the difference between δF in air and carbon dioxide is predicted to grow with background displacement amplitude. At sufficiently high displacement then, differences in δF may be amplified far beyond the differences in bandwidth. Nonlinear measurements may potentially be used to distinguish between similar gases with a degree of sensitivity higher than that available with standard linear measurements.

8.4.2. Model predictions

The predicted sensitivity of linear and nonlinear measurands was investigated for beam A. Viscosity and density was varied in the model, to see the effect each had on resonant frequency, bandwidth and δF . The initial values for viscosity and density were taken to be those for carbon dioxide, as model predictions most often closely measured data for this gas, whether in the linear or nonlinear regime.

For linear measurements, a value of $\bar{h}=8.5\text{E-}11$ was adopted, as this ensured predictions remained linear. For nonlinear measurements, $\bar{h}=2\text{E-}9$ so as to remain within the range considered in figure 8.10. Predictions were then made for each measurand where (a) viscosity was held constant and density increased in increments up to 150% of the initial value, and (b) the converse of this. Figures 8.16 to 8.20 show the predicted measurements over this range.

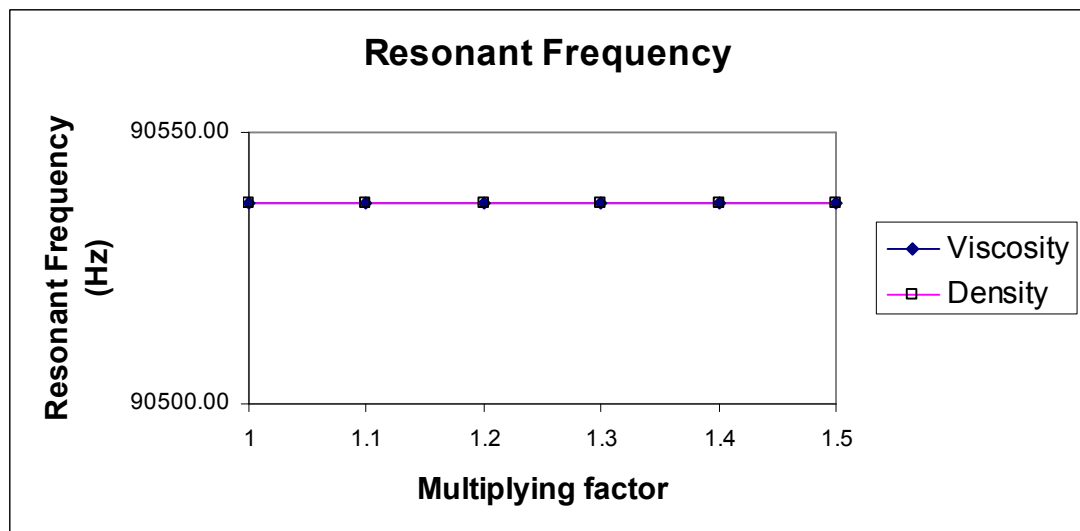


Figure 8.16: Fluctuation of resonant frequency with viscosity or density; predictions for beam A using linear elliptic cylinder model

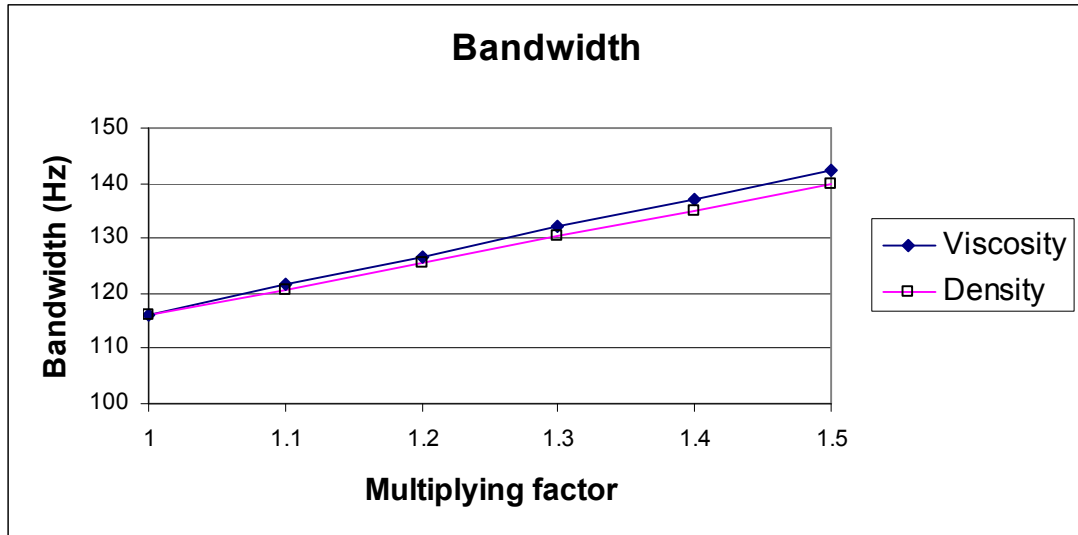


Figure 8.17: Fluctuation of bandwidth with viscosity or density; predictions for beam A using linear elliptic cylinder model

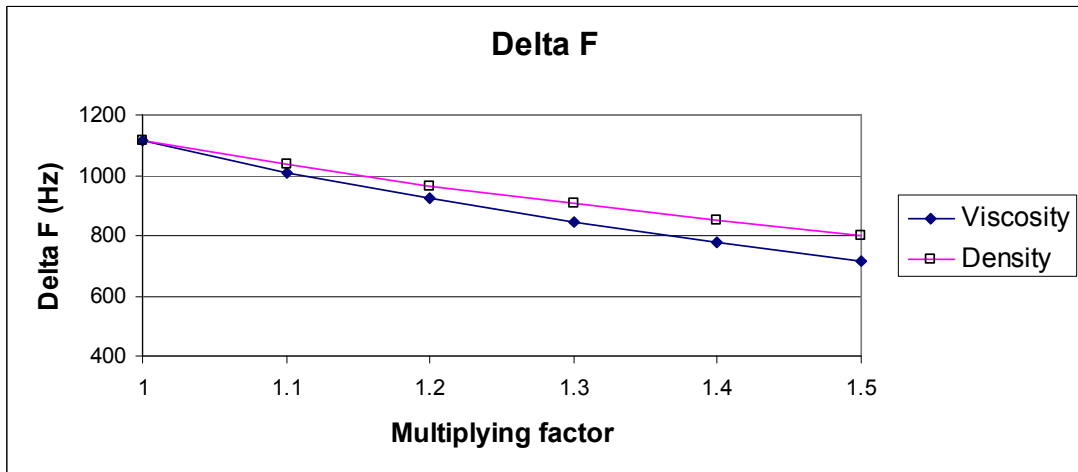


Figure 8.18: Fluctuation of ΔF with viscosity or density; predictions for beam A using linear elliptic cylinder model

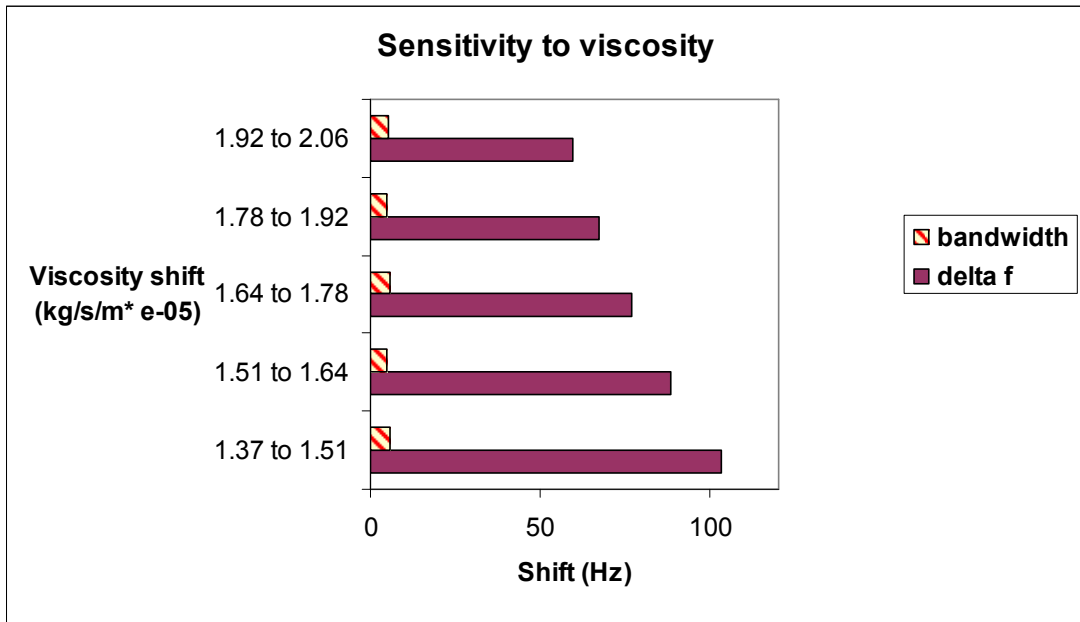


Figure 8.19: Sensitivity of bandwidth and δF to fluctuations in viscosity

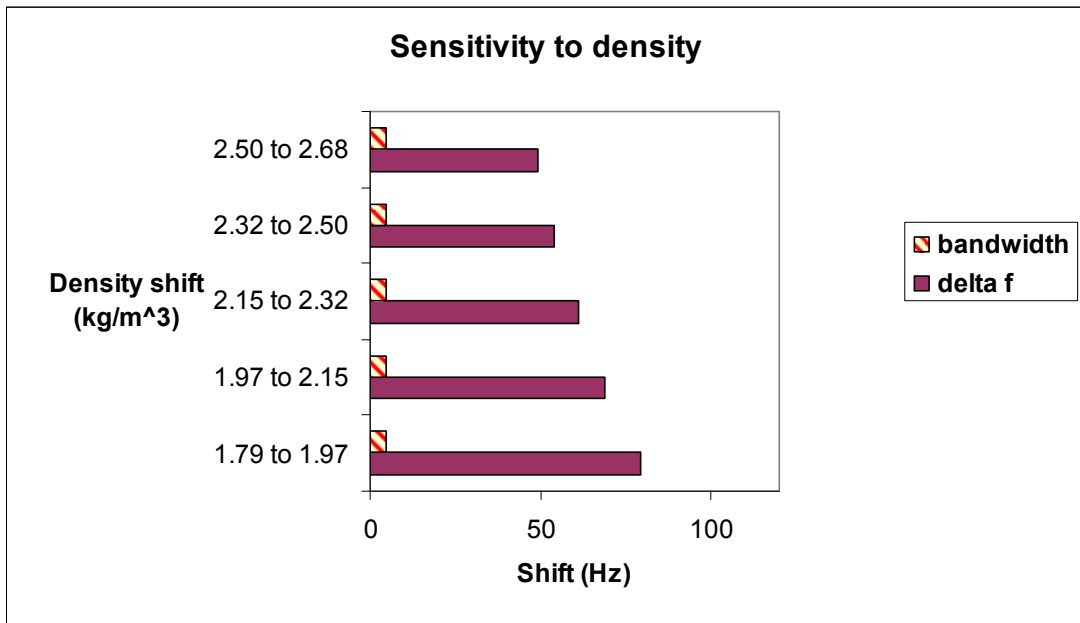


Figure 8.20: Sensitivity of bandwidth and δF to fluctuations in density

Over the range considered, no change in the resonant frequency was observed. δF and bandwidth did change with both density and viscosity, with δF showing the greater sensitivity to changes in fluid properties. This confirms predictions made in section 4.5.4, and the implications of this are discussed in the following chapter.

8.5. References

1. Rao, S.S. *Mechanical vibrations*. 4th ed. Pearson Prentice Hall, 2004.

Chapter 9

Conclusions

The aim of this work was to investigate the nonlinear response of rectangular MEMS resonator beams immersed in gases. The measurand δF was identified as an indicator for gas properties. Suitable experiments were designed and conducted to provide data for two differently proportioned silicon beams operated in four different gases and two pressure regimes. The major contributions of the thesis are outlined below in section 9.1. This is followed by a discussion of the limitations of the study in section 9.2. Implications of the study are outlined in section 9.3. Finally, suggestions for further work are made in section 9.4.

9.1. Contributions

The equation of motion for a clamped-clamped beam in a fluid has been shown in section 4.2.1 to be of the form of the damped Duffing equation. Amplitude jump points are predicted to occur when the harmonic forcing is of sufficient magnitude, and the observation made that the frequency separation δF between these points is dependent on the dynamic viscosity and density of the fluid. At low damping, nonlinear beam resonators are shown to be potentially more sensitive to changes in fluid properties than existing linear resonating devices.

Experimental data presented in chapter 7 confirms the qualitative findings of the modelling and illustrates that measurements of δF may be used to uniquely identify gases. The magnitude of δF is seen to be dependent on beam dimensions. In addition, it is shown that δF may be amplified to magnitudes far exceeding linear measurements of bandwidth with the same beam.

Further analysis in section 8.2 demonstrates that the magnitude of δF is highly dependent on the magnitude of the applied displacement and its frequency dependence (referred to as the ‘background profile’).

Focusing on one of the rectangular beams only, a damping model was developed with parameters extracted from the experimental data. Numerical predictions from

this model indicate that a rectangular resonator beam operated in the nonlinear regime can show sensitivity to changes in fluid properties at low viscosity and density of at least an order of magnitude better than when it is operated in the linear regime.

With respect to previous related research, this work extends the potential of clamped-clamped beam resonators as sensors, by introducing the new measurand δF . A review of the literature suggests that this is the first work to attempt this particular approach. Using the measurand δF may allow for the development of high-sensitivity viscosity or density sensors. However, numerical simulations do not show any advantage in using this measurand in mass sensing applications.

9.2. Limitations of the study

The study has a number of limitations, arising from both the experimental work and the system modelling.

9.2.1. Experimental issues

Beam imperfections

With the given manufacturing procedure, it is not possible to produce a perfectly rectangular beam with an idealised geometry. There will inevitably be a certain amount of undercut or overcut around the beam, particularly at the beam ends. This was difficult to measure with the equipment available. In addition, profile scans revealed a certain degree of bowing in the beams. Both of these issues are likely to affect beam behaviour and therefore the accuracy of the model.

Impurities

Without a procedure for repeatedly cleaning the devices between measurements, it was not possible to know whether or not any impurities had attached themselves to the beams during the experiments. A particular concern would be moisture from humid air attaching itself to beams, reducing their resonant frequency in the process. This would negatively affect the accuracy of resonant frequency measurements.

Bonding issues

The method for attaching devices to the piezo actuator introduces several uncertainties. On first attaching silicon devices to the copper disks, it is possible to introduce tension or compression across the beam, as well as potentially failing to fully adhere parts of the device handle layer. The differing coefficients of thermal expansion for silicon, copper, steel, epoxy and resin mean that temperature-induced fluctuations in beam boundary conditions are difficult to predict. These issues might be addressed by considering an alternative process for attaching devices to the actuator, or considering an alternative method of actuation.

Temperature control

The chosen method of temperature control with peltier plates was limited. It was not possible to cool the inside of the chamber to below room temperature within a reasonable time, if at all; only to heat the chamber by running the peltiers in reverse. To set the temperature of the chamber accurately was also impossible: approximate temperatures could be achieved by manually adjusting the voltage of the power supply to the peltiers, keeping in mind the ambient room temperature.

A more effective method for temperature control with peltiers may be to use some integrated control circuit, with a feedback loop, to continually monitor chamber temperature and adjust power supply automatically. The addition of thermal cladding around the chamber could aid in minimising heat flow in and out of the chamber.

Sealing of chamber

The chamber was seen to leak, allowing gases to escape or enter the chamber. This was particularly undesirable when trying to measure beam behaviour in a vacuum: only a low vacuum could be achieved, making it difficult to establish the degree of intrinsic damping present. In addition, gases would cease to remain 100% pure throughout the experiments. Variations in pressure resulting from gas loss from the chamber affect gas density, creating uncertainties in the results. A thorough examination of the chamber, and possibly a redesign of certain features, might rectify this problem.

Background control

As outlined in detail in chapters 7 and 8, the profile of the applied background displacement was very difficult to control. Temperature drift meant that background measurements could also not be linked to beam vibration measurements without introducing an unknown error.

9.2.2. Modelling issues

Flow separation

The models adopted for the fluid drag on the beam assume that there is no separation of the flow. However, as discussed, since the resonator beam is not streamlined, a certain amount of separation must occur, leading to pressure drag. When operating the beam in the nonlinear regime, the Reynolds number and/or the Keulegan-Carpenter number can be seen to reach values where it would be necessary to consider pressure drag.

Missing modes and harmonics

Beam behaviour is approximated by considering only the fundamental mode of vibration and the first harmonic term. This approach is useful in that it simplifies the model sufficiently to allow for qualitative predictions to be made. The weakness though is that it may not account for the whole of the beam behaviour nor the damping on the beam.

Beam aspect ratios

Neither of the beams used in experiment have aspect ratios within the limits recommended for the elliptic cylinder damping model. This may affect the accuracy of the damping coefficient.

Model parameters

The parameters a and b determined for beam A have different values in the linear regime and the nonlinear regime. This is sufficient for approximating beam behaviour in the chosen regime, but indicates that the elliptic cylinder model is incomplete.

9.3. Implications of study

The results are of direct practical relevance. Using clamped-clamped beam resonators and the measurand δF , it should be possible to design a novel sensor capable of:

- measuring viscosity or density directly
- identifying fluids directly
- responding to changes in fluid properties with a high degree of sensitivity.

For the direct identification of a fluid, it may be necessary to use a combination of linear and nonlinear measurements, or alternatively to take two nonlinear readings with differently sized or proportioned beams. Figure 4.12 in section 4.5.2 indicates that, for a given beam and displacement magnitude, there should exist contours of equal δF when plotting the measurand against fluid viscosity and density. Numerical simulation shows that, for two differing beams, there will however exist a unique δF pair in a particular fluid.

Remaining uncertainties in the model suggest that, at this stage, it would be necessary to calibrate any devices in known fluids before they could be reliably used as sensors.

The principles of the work are extendable to more viscous fluids, including liquids. This would obviously require a higher level of displacement, and may require more sophisticated modelling to compensate for any breaking of the current modelling constraints. It may also be true that the approach could be used in non-Newtonian fluids, but this has not been investigated.

Although this study was conducted on MEMS devices, the results should be generalisable to larger scale devices. Using larger devices would require greater applied displacements to achieve δF of similar magnitude to MEMS scale devices. However, there may be advantages in terms of manufacture, cost, robustness, and uniformity of beam geometry. In general, the beam dimensions and materials would have to be selected according to the desired application.

9.4. Further work

There are various areas for further investigation, relating to both practical and theoretical issues. These are discussed below.

9.4.1. Actuation

To develop a reliable sensor, it would be necessary to have accurate control of the actuation. The amplitude of actuation has been shown to be crucial, and can have a far greater effect on measurements than small changes in fluid or device properties. Either the sensor is designed using a more appropriate or controllable piezoelectric actuator, or it may be desirable to consider an alternative method of actuation, such as electrostatic actuation [1], electromagnetic [1,2], thermal/electrothermal [1,3,4] or optical [1,5]. Any method of actuation chosen would have to be able to provide sufficient displacement or forcing to the beam, at levels above any noise in the system.

9.4.2. Detection

The chosen optical detection method may prove unsuitable for use with opaque fluids, or with nano-scale devices, due to difficulties in focusing a laser onto the resonator surface. In addition, it is possible that laser heating of a resonator could produce spurious results. It may be necessary therefore to investigate using an alternative method of detection. Stemme [1] discusses various methods of excitation and detection. Methods of detection covered include capacitive, dielectric, piezoelectric, piezoresistive and magnetic.

9.4.3. Alternative fluids and materials

The damping model developed in this work is sufficient to prove the concept of the proposed sensor. However, further work would be required to confirm that such a sensor may be developed for use in more viscous fluids such as liquids, or in non-Newtonian fluids.

Although silicon has been favoured as the beam material in this work, it may not necessarily be the most appropriate material for any given application. Alternative materials should be considered e.g. plastics, metals or glass.

9.4.4. Develop damping model

The existing damping model could be extended to offer a more complete description of the damping forces. There are clear uncertainties with the current intrinsic and fluid damping models. The following modifications to the models may enhance their accuracy, although it is not apparent to what degree without further investigation.

Pressure drag

Since a certain degree of flow separation is inevitable with a rectangular beam, the profile drag might be better represented as a quadratic force. This would then account for both the skin friction drag and the pressure drag (see section 3.2).

Added mass

Although it was demonstrated as being negligible in a low viscosity gas, it may be appropriate to introduce an added mass term to the elliptic cylinder model for completeness. This might then help extend the validity of the fluid damping model to higher viscosities.

Flow regimes

Most fluid damping models in the literature are specific to a pressure regime. Work by Bidkar [6] describes a model for the gas damping which is valid over four orders of magnitude of Knudsen numbers spanning the free-molecular, the transition, and the low pressure slip flow regimes. Such an approach is worth investigating if it can deliver a more consistent damping model for gases.

Nonlinear damping terms

Several authors suggest the inclusion of nonlinear damping terms in the damping model. Zaitsev et al [7] demonstrated the need to include a nonlinear damping term in the analysis of a clamped-clamped nanomechanical beam in vacuum, in order correctly model the dynamics. Morfey and Tan [8] state that nonlinearities appear in the fluid drag once the beam displacement amplitude becomes comparable with the viscous penetration depth at the oscillation frequency.

9.4.5. Analysis of further modes and/or harmonics

As discussed in sections 4.2 and 4.3.1, for simplicity of analysis, various modes and harmonics have been deliberately neglected. Off-resonant modes are unlikely to make a significant contribution to the behaviour of the beam when it is operated close to the fundamental resonant frequency. However, the subharmonic and superharmonic oscillations which occur in a nonlinear system may make a measurable contribution, and as such would merit further investigation.

9.4.6. Alternative applications

It has been demonstrated that the measurand δF is highly susceptible to changes in the applied displacement. With this in mind, it may be possible to exploit this feature and create novel devices which seek to measure or react to the level of actuation, as opposed to fluid properties.

9.5. References

1. Stemme, G. 'Resonant silicon sensors', *Journal of Micromechanics and Microengineering*, **1** (2), 1991, pp. 113-125.
2. Greywall, D.S. 'Micromechanical RF filters excited by the Lorentz force', *Journal of Micromechanics and Microengineering*, **9** (1), 1999, pp. 78-84.
3. Jianqiang, H. et al. 'Dependence of the resonance frequency of thermally excited microcantilever resonators on temperature', *Sensors and Actuators A: Physical*, **101** (1-2), 2002, pp.37-41.
4. Bargatin, I., Kozinsky, I., Roukes, M.L. 'Efficient electrothermal actuation of multiple modes of high-frequency nanoelectromechanical resonators', *Applied Physics Letters*, **90**, 2007, 093116.
5. Lammerink, T.S.J., Elwenspoek, M., Fluitman, J.H.J., 'Optical excitation of micro-mechanical resonators', *Proceedings of MEMS '91: IEEE Micro Electro Mechanical Systems, An Investigation of Micro Structures, Sensors, Actuators, Machines, and Robots*, Nara, Japan, 1991, , pp. 160–165.
6. Bidkar, R.A. et al. 'Unified theory of gas damping of flexible microcantilevers at low ambient pressures', *Applied Physics Letters*, **94**, 2009, 163117
7. Zaitsev, S. et al. 'Nonlinear dynamics in nanomechanical oscillators', *Proceedings of the 2005 International Conference on MEMS, NANO and Smart Systems (ICMENS 2005)*, Banff, Alberta, USA, 24-27 July 2005.
8. Morfey, C.L., Tan, M. 'Unsteady drag on a cylinder due to transverse oscillation at finite amplitude', *Journal of Sound and Vibration*, **246** (4), 2001, pp. 705-721.

Appendix A – Fluid Properties

Gas properties at atmospheric pressure (1 atm)

Gas	Temperature (K)								
	293.15			298.15			300		
	Density (kg/m ³)	Dynamic viscosity (10 ⁻⁵ Pa.s)	Speed of Sound (m/s)	Density (kg/m ³)	Dynamic viscosity (10 ⁻⁵ Pa.s)	Speed of Sound (m/s)	Density (kg/m ³)	Dynamic viscosity (10 ⁻⁵ Pa.s)	Speed of Sound (m/s)
Air (dry)	1.2041 [2] 1.207 [5] 1.205 [3] 1.2047 [10]	1.8205 [10]	343.3 [1]	1.225 [7] 1.1845 [10]	1.7894 [7] 1.8444 [10]	346.2	1.1771 [10]	1.983 [3] 1.8531 [10]	347.3 [1]
Helium	0.1664 [3] 0.16674 [10]	1.9561 [10] 1.941 [11]	1007.4 [1]	0.1625 [7] 0.16394 [10]	1.99 [7] 1.9793 [10]	1015.9	0.164 [5] 0.16293 [10]	1.9879 [10]	1019.1 [1]
Argon	1.661 [3] 1.6617 [10]	2.2294 [10] 2.217 [11]	318.8 [3,4]	1.6228 [7] 1.6337 [10]	2.125 [7] 2.2606 [10]	321.9	1.449 [5] 1.6236 [10]	2.2721 [10]	323 [2] 322.5 [3,4]
Carbon dioxide	1.839 [6] 1.842 [3] 1.808 [10]	1.469 [6] 1.4620 [10] 1.480 [11]	266.2 [3] 266.6 [6]	1.7878 [7] 1.7774 [10] 1.808 [6]	1.37 [7] 1.4831 [10] 1.493 [6]	268.5 268.6 [6]	1.797 [6] 1.7662 [10]	1.502 [6] 1.4910 [10]	269.3 [3] 269.4 [6]
Nitrogen	1.165 [3] 1.1651 [10]	1.7550 [10]	349.0 [3]	1.138 [7] 1.1455 [10]	1.663 [7] 1.7782 [10]	352.0	1.145 [5] 1.1384 [10]	1.7867 [10]	353 [2] 353.1 [3]

Note: speed of sound at 298.15 K is approximated from other available data.

Liquid properties

Liquid	Temperature (K)					
	293.15			298.15		
	Density (kg/m ³)	Dynamic viscosity (10 ⁻⁵ Pa.s)	Speed of Sound (m/s)	Density (kg/m ³)	Dynamic viscosity (10 ⁻⁵ Pa.s)	Speed of Sound (m/s)
Water				998.2 [7]	0.001003 [7]	
Glycerin				1259.9 [7]	0.799 [7]	
Cyclohexane	778.5 [8]				0.00098 [9]	

Sources:

[1] <http://hyperphysics.phy-astr.gsu.edu/hbase/HFrame.html>

[2] <http://en.wikipedia.org>

[3] <http://www.engineeringtoolbox.com/>

[4] <http://www.diracdelta.co.uk/science>

[5] <http://physics.info/density/>

[6] <http://www.peacesoftware.de/>

[7] Fluent

[8] http://www.simetric.co.uk/si_liquids.htm:

[9] http://www.arb.ca.gov/db/solvents/solvent_pages/Hydrocarbon-HTML/cyclohexane.htm

[10] <http://www.mhtl.uwaterloo.ca/old/onlinetools/airprop/airprop.html>

[11] Handbook of basic tables for chemical analysis, Second edition, Thomas J Bruno, Paris D.N. Svoronos. CRC Press, 2003.

Appendix B - Silicon Properties

Density 2329 kg.m^{-3} at 300K [1]

Young's modulus $169 \times 10^9 \text{ kg.m}^{-1}.\text{s}^{-2}$ at 300K for <110> direction [2]

Coefficient of linear thermal expansion $2.616 \times 10^{-6} \text{ K}^{-1}$ at 300K [1]

Specific heat capacity $1.63 \times 10^6 \text{ J.K}^{-1}.\text{m}^{-3}$, $710 \text{ J.kg}^{-1}.\text{K}^{-1}$ [3, 4]

Thermal conductivity= $149 \text{ W.K}^{-1}.\text{m}^{-1}$ at 300K [5]

Poisson's ratio 0.28 [3]

Sources:

[1] Hull, R. *Properties of crystalline silicon [electronic resource]*. London: INSPEC, the Institution of Electrical Engineers, c1999.

[2] O'Mara, W., Herring, R., Hunt, L. *Handbook of semiconductor silicon technology*. Noyes Publications, 1990.

[3] Hao, Z., Erbil, A., Ayazi, F. 'An analytical model for support loss in micromachined beam resonators with in-plane flexural vibrations', *Sensors and Actuators A*, **109**, 2003.

[4] <http://www.engineeringtoolbox.com/>

[5] <http://en.wikipedia.org/wiki/Silicon>